Optical Properties and Application of Metallic Nanoparticles and their Assembled Superstructures

by

Ashish Agarwal

A dissertation submitted in partial fulfillment
of the requirements for the degree of
Doctor of Philosophy
(Chemical Engineering)
in The University of Michigan
2010

Doctoral Committee:

Professor Nicholas Kotov, Chair
Professor Sharon C. Glotzer
Associate Professor Joerg Lahann
Assistant Professor Anish Tuteja

To my parents Anil Agarwal and Seema Agarwal, my wife Rohini Agarwal and my sister Neha Agarwal for their love, support and encouragement.

ACKNOWLEDGEMENTS

My five years at University of Michigan have been truly wonderful. I got the opportunity to meet so many brilliant and interesting people and learn so many new things on campus. First and foremost, I would like to thank my advisor Professor Nicholas A. Kotov for his invaluable guidance during the course of this thesis. I am grateful to Dr. Kotov for giving me the opportunity to explore and innovate in his lab. I enjoyed being a graduate student in his lab and apart from the many scientific skills I learned from him, I learned *how to think big* from him. Thank you again Dr. Kotov.

I am ever grateful to Late Prof. Kartic Khilar (IITB) for being my teacher, mentor and friend. A special thanks to Professor Luis Liz Marzan for giving me the opportunity to visit spain and spend time in his lab. I would like to thank Professor Peter Palffy-Muhoray, Professor Theodore Norris, Professor Xueding Wang and Professor Kang Kim for their collaboration and scientific discussion on various projects and ideas. I am grateful to my present and past lab members who helped me learn using microscopes and other equipment essential for my research.

I would like to thank my friends Amit Kaushik, Gaurav Bansal, Sibasish Mukherjee, Devesh Kumar, Saumil Ambani, Sudhanshu Srivastava, Jake Fontana, Meghan Cuddihy, Christine Andres, Peter Ho, Edward Jan for their support. Tea time discussions with amit, sibu, GB and sud recharged my batteries for long hours in lab. Last but not the least; I am grateful to my parents, my sister and my wife. I could not have come so far without them.

TABLE OF CONTENTS

LIST OF FIGURES

Figure

LIST OF TABLES

Table

LIST OF ABBREVIATIONS

B Biotin

BT Benzenethiol

CB Circular Birefringence

LD Circular Dichorism

CJD Creutzfeldt-Jakob Disease

CT Computed Tomography

CTAB Hexadecyltrimethylammonium bromide

CW Continuous Wave

EDC N-ethyl-N′-(3-dimethylaminopropyl)carbodiimide

ELISA Enzyme-Linked Immunosorbent Assay

FWHM Full Width at Half-Maximum

GNRs Gold Nanorods

HU Hounsfield Units

HUVECs Human Umbilical Vein Endothelial Cells

ICG Indocyanine Green

ICAM-1 Intercellular Adhesion Molecule-1

IFN-γ Interferon-gamma

IL-6 Interleukin-6

LB Linear Birefringence

LBL Layer-by-Layer

LD Linear Dichorism

LSPR Localized Surface-Plasmon Resonance

LPR Longitudinal Plasmon Resonance

MRI Magnetic Resonance Imaging

NHS N-hydroxy-succinimide

NP Nanoparticle

NIR Near Infrared

NIM Negative Index Materials

OA Oleylamine

OPO Optical Parametric Oscillator

PBS Phosphate Buffered Solution

PEG Polyethylene Glycol

PAI Photoacoustic Imaging

PA Photoacoustic

PAA Polyacrylic acid

PU Polyurethane

RA Rheumatoid Arthritis

ROI Region of Interest

SA Streptavidin

SCC Squamous Cell Carcinoma

SEM Scanning Electron Microscope

SERS Surface Enhanced Raman Scattering

SNR Signal-to-Noise Ratio

SPAT Short-pulsed Photoacoustic Tomography

SPECT Single-Photon Emission Computed Tomography

TEM Transmission Electron Microscope

TGA Thermogravimetric Analysis

TNF-α Tumor Necrosis Factor alpha

TPL Two-Photon Luminescence

ABSTRACT

This dissertation reports the development of novel targeted contrast agents based on gold nanorods (GNRs) and their application in imaging cancer cells, cardiovascular inflammatory diseases and drug delivery monitoring using photoacoustic imaging (PAI). The GNRs based contrast agents were imaged with high signal-to-noise ratio (∼17) and excellent spatial resolution (∼250 µm) with concentration down to 10 pM in biological tissues. The inherent disadvantage of limited imaging depth (∼5 mm from skin surface) in PAI due to strong attenuation of light in biological tissues restricts the monitoring of drug delivery in intra-articular connective tissues. A novel targeted optical and nuclear dual-modality contrast agent was successfully developed by radiolabeling GNRs with ^{125}I to monitor anti-rheumatic drug delivery. PAI and nuclear imaging in combination present the detailed distribution of GNRs conjugated anti-rheumatic agent in intra-articular connective tissues with concentration down to 10 pM and radioactive label of 5 µCi . Radiolabeled contrast agents were further conjugated with polyethylene glycol (PEG) to increase the *in vivo* circulation time and prevent rapid clearance through accumulation into liver. Addition of PEG molecules on the surface of contrast agent increased the *in vivo* circulation time from 4 minutes to over 4 hours allowing specific targeting by the contrast agent.

Apart from application as a contrast agent, gold nanorods due to their anisotropic shape also form interesting building blocks for 3D superstructures with wide range of optical properties for applications in plasmonics, metamaterials and sensors. Under controlled evaporation monodisperse GNRs were self-assembled into micron sized

three dimensional supercrystals. The highly organized supercrystals of GNRs with plasmonic antennae enhancement of electrical field have made possible the first real-time detection of prions (concentration down to 10^{-10} M) in complex biological media such as serum using surface enhanced raman scattering. CdTe nanoparticle-GNRs superstructures were made through biotin-streptavidin specific binding and investigated as potential gain materials for overcoming metallic losses in metamaterials through exciton-plasmon coupling. An extremely simple technique was developed to transfer gold nanorods from aqueous to organic medium, which allowed orientational ordering of low aspect ratio rods in dispersion through application of high electric fields. Alignment of non-aqueous GNRs in dispersion was achieved with a maximum order parameter of S$\approx$0.9. The key results reported in this report are anticipated to lead to the development of novel, sophisticated, multifunctional contrast agents which can recognize specific receptors, deliver drugs to targeted tissue, aid in reporting outcome of therapy, provide real-time assessment of therapeutic efficacy, and most importantly, monitor intracellular changes to help understand pathological mechanisms. The novel superstructures reported with GNRs in various spatial arrangements are anticipated to lead to the development of commercial diagnostic substrates, sensors and plasmonic metamaterials.

CHAPTER I

Introduction

Nanotechnology is the science of controlling matter at the atomic or molecular scale. In the past decade major advances have been made in the synthesis of nanoparticles (NPs) of various size, shape and composition with high degree of monodispersity. However applications in imaging, plasmonics and metamaterials[1–4] require a substantial progress in engineering multifunctional NP surfaces as well as assembly of individual nanoparticles into complex 3D geometries. The optical and magnetic responses of an ensemble of NPs are dramatically different compared to the individual NPs due to collective resonance of free electrons on the surface. Hence a very high degree of control over spatial organization is required to assemble and arrange the nanoparticles into various configurations to achieve desired optical response from the material. Functionalizing NP surfaces with various biomolecules, polymers and surfactants is a key step towards fine tuning various forces acting upon the NPs that eventually lead to organized superstructures. This dissertation reports novel developments in engineering functional metallic nanoparticles and their application in molecular imaging, diagnostics and optical metamaterials.

The emergence of "molecular imaging" as an integrated discipline in medicine has set the stage for an evolutionary leap in diagnostic imaging and therapeutic monitoring. Molecular imaging makes molecular processes visible, quantifiable, and trackable

over time in a live animal or human, in physiologically authentic environments. In the preclinical stages, molecular imaging reduces the number of experimental animals that need to be sacrificed because data is generated noninvasively. In clinical practice, molecular imaging may help with the decision to take, or not take, a drug candidate into clinical trials and will offer another way to monitor efficacy once a drug is in trials. Molecular imaging involves integrating new imaging technology with new imaging agents. The coincident expansion of nanotechnology, which can significantly accelerate the development of new imaging agents, has already played a fundamental role not only in molecular imaging, but also in biosensors, biomarkers, and drug delivery.[5] This area of research is anticipated to lead to the development of novel, sophisticated, multifunctional applications which can recognize specific receptors, deliver drugs to targeted tissue, aid in reporting outcome of therapy, provide real-time assessment of therapeutic efficacy, and most importantly, monitor intracellular changes to help understand pathological mechanisms.

Photoacoustic tomography or Photoacoustic Imaging (PAI), also referred to as optoacoustic tomography or thermoacoustic tomography, is an emerging hybrid molecular imaging modality that is non-invasive, non-ionizing, with high sensitivity, satisfactory imaging depth and good temporal and spatial resolution.[6–18] In SPAT, a short-pulsed laser source is used to illuminate the tissue sample and generate photoacoustic waves due to thermoelastic expansion. Then the signals are measured by wide-band ultrasonic transducers to reconstruct the image of the sample. Therefore, the contrast of PAI is based on the optical absorption in biological tissues, but its resolution is not limited by optical diffusion or multiple photon scattering but instead by the bandwidth of detected photoacoustic waves.[19] Because ultrasonic waves are much less scattered in biological tissues than light, PAI depicts subsurface joint tissue structures much more accurately than optical imaging. In other words, PAI overcomes the resolution disadvantage of optical imaging and the contrast disadvan-

tage of ultrasound imaging. Moreover, like conventional optical technologies, PAI also presents a unique ability in tracing optical contrast agents in biological tissues. The application of PAI holds promise for evaluation at molecular or cellular level due to the high sensitivity of PAI to a variety of extrinsic optical contrast agents. Monitoring of drug delivery in experimental models and in human diseases would undoubtedly be very helpful for both basic research and clinical management of diseases.

Several organic dyes and metallic NPs have been studied as PAI contrast agents in the past decade. Wang *et al* have demonstrated enhanced photoacoustic signal from Indocyanine Green (ICG), an FDA approved dye that absorbs light in the Near-Infrared (NIR) region.[20] Ashkenazi *et al* has developed ICG embedded ormosil particles conjugated with HER2 for targeted imaging of breast cancer cells.[21] More recently Song *et al* has used Methyline Blue as a contrast agent to detect sentinel lymph node.[22] In comparison with the contrast agents based on organic dyes, metallic NPs could have better stability, less photo bleaching and greater flexibility of tuning their optical spectra, although further investigation is necessary to reduce their toxicity before large scale clinical use can occur.[23] Gold nanoparticles have particularly been used as PAI contrast agents due to their exceptionally strong optical responses in the visible and NIR spectral range.[10,21,24–29] The combination of the unique optical and biological properties of gold nanoparticles makes them a good choice for optical contrast agent. PAI utilizes the strong optical absorption of gold nanoparticles which is due to localized surface-plasmon resonance (LSPR). This is a classical effect in which the electromagnetic field from the light source drives the collective oscillations of free electrons of metallic nanoparticles into resonance. Typically, the absorption cross section of a metal nanoparticle can be an order of magnitude larger than its geometrical cross-sectional area.[30] Employing laser-based PAI, the dynamic distributions of gold nanoshells based contrast agents in small-animal brains have been imaged with both high spatial resolution and satisfactory sensitivity.[20,31] Yang

et al has studied gold nanocages to evaluate the cerebral vortex in rats.[32] Other than performing as contrast agents for imaging, gold NPs have also been widely used as vehicles to achieve drug delivery and agents for photothermal therapeutics.[33–35] Most of reports in literature that have explored metallic NP as contrast agents for the enhancement of PAI sensitivity are generic in nature, lacking specific targeting of tumor cells or inflammatory regions of interest.

Gold Nanorods (GNRs) are a unique kind of gold nanoparticles because of their shape anisotropy, sharp resonances in optical regime and the irrelatively small size, with their diameters approaching the molecular scale. GNRs due to anisotropy in shape have two plasmon resonance peaks, smaller peak in the 500 nm range due to the plasmon oscillation perpendicular to the axis of the rod, while the strong NIR peak, which is tunable by varying the nanorod aspect ratio, originates from the longitudinal oscillations of plasmons along the main axis. Since NIR light transmits through tissue more efficiently than visible light, the additional plasmon resonance makes nanorods promising candidates for in vivo diagnostic and therapeutic applications. This research reports the development of novel GNRs based targeted contrast agents, studied extensively for inflammatory response imaging, tumor imaging and monitoring anti-rheumatic drug delivery (Chapter II&III).[36–38]

Despite the variety and relative effectiveness of PAI contrast agents available, there is an inherent disadvantage in PAI measurements due to the strong attenuation of light in biological tissues as well as the high background signal as a result of intrinsic tissue optical absorption. PAI presents local spatial resolution on the sub-millimeter level however the penetration depth limits its ability to make measurements with satisfactory signal-to-noise ratio deep inside the tissue. In fact, the same problem is present for all nanoparticle contrast agents based on optical emission, which became increasingly popular recently. This inherent problem of light emission can be overcome indirectly by merging it with another imaging modality which can provide high signal-

to-noise ratio even deep inside the tissue and assist to validate the findings of the other technique. The intrinsic disadvantage of limited imaging depth in PAI was overcome by designing radiolabeled targeted contrast agent based on GNRs, to merge PAI with nuclear imaging (Chapter IV). Moreover, by covalent binding of radioisotopes on the surface of targeted GNRs, nuclear imaging such as PET and SPECT can for the first time image the concentration and distribution of gold NP based agents in vivo, which could contribute considerably to understanding of the toxicity and pharmacokinetics of any novel gold nanocolloids in the future (Chapter V).

The idea of targeted contrast agents is extended to another form of widely used clinical imaging technique, X-ray computed tomography (CT). CT is one of the most useful diagnostic tools in hospitals today in terms of availability, efficiency, and cost. Currently, CT is not a molecular imaging modality since relevant targeted and molecularly specific contrast agents have not yet been developed. Present CT contrast agents are predominantly based on iodine containing molecules, which are effective in absorbing X-rays; however, they are nonspecifically targeted because they cannot be conjugated to most biological components or cancer markers and they allow only very short imaging times due to rapid clearance by the kidneys. Chapter VI demonstrates the potential of targeted GNRs based contrast agents for molecular CT imaging.

Understanding and controlling the collective behavior of nanoparticles (NPs) is a challenging problem of fundamental and practical importance.[39] This is particularly true for GNRs because their anisotropy implies additional functionality on the scale of individual particles and their assemblies, enabling a variety of applications from cloaking devices to biological sensing and solar energy conversion.[40–45] One of the most fascinating types of metamaterials that is actively researched is negative refractive index materials (NIMs), which often requires GNRs assembled into various configurations. Among other challenges, one of the major limitations of present day NIMs is their large amount of energy dissipation which frustrates the restoration of

near field modes. To take advantage of exciton-plasmon interactions, an optical system consisting of semiconductor nanoparticles (NPs) and GNRs that can continuously pump energy into the NIM resonator is described in Chapter VII. A key requirement for realizing bulk optical NIMs is controlling orientational order of GNRs. However due to the high dielectric constant of water, aqueous dispersion of low aspect ratio GNRs cannot achieve good alignment upon application of electric field. Chapter VIII describes a simple novel technique for transferring GNRs from aqueous to organic solvents. Field induced orientational control of low aspect ratio GNRs dispersed in toluene was achieved.

Under controlled evaporation individual GNRs were assembled into large 3D supercrystals with uniform hexagonal packing which due to nanoantenna phenomena exhibits strong electric field enhancements in interstitial gaps. Chapter VIII describes the detection of infectious prion proteins using the 3D GNRs supercrystal as surface enhances raman scattering (SERS) substrate. CST MICROWAVE STUDIO simulations are performed to investigate the nanoantenna phenomena. Chapter X concludes the dissertation by giving a brief summary of results and directions for future research work.

CHAPTER II

Photoacoustic Imaging of Early Inflammatory Response Using Gold Nanorods

2.1 Introduction

Excessive and uncontrolled inflammation plays a key role in a variety of systemic diseases including rheumatoid arthritis (RA), systemic lupus erythematosus, and allergic diseases and a key role in atherogenesis. Furthermore, patients with diseases characterized by chronic systemic inflammation are at risk to develop accelerated atherosclerosis.[46,47] Understanding the correlation between inflammation and atherosclerosis may therefore provide prognostic information of considerable clinical utility.[48]

Most myocardial infarctions occur when a plaque ruptures and a clot forms at the site. Inflammation is believed to be a major factor in plaque rupture, and susceptible plaques tend to have a damaged fibrous cap and numerous resident macrophages. Inflammatory mediators promote the secretion of various collagenases, which erode the fibrous cap and prevent its repair by smooth muscle cells. Blood that leaks through the damaged cap coagulates quickly, aided by clot promoters produced by T-lymphocytes and foam cells.[49] Some biomarkers have predictive value for future vascular events among apparently healthy subjects. Prospective epidemiological stud-

ies have found increased vascular risk in association with increased basal levels of inflammatory cytokines such as interleukin-6 (IL-6)and tumor necrosis factor alpha (TNF-α); cell adhesion molecules such as soluble or membrane-bound ICAM-1, P-selectin, and E-selectin; and acute-phase reactants such as C-reactive protein and fibrinogen. In this study, the adhesion molecule intercellular adhesion molecule-1 (ICAM-1) was chosen as a biomarker of inflammation and activation of endothelial cells (ECs). ICAM-1 is also a strong inflammatory mediator in systemic inflammatory diseases such as RA.[50]

Photoacoustic imaging (PAI) can be of exceptional value for detection of inflammation and, in particular, the early forms of immune response. It uses rapid thermal expansion induced by absorption of a laser pulse to create acoustic waves that can propagate to a remote acoustic sensor. The distribution of optical absorption within the object can be imaged by reconstructing the detected acoustic field.[51] The contrast of a photoacoustic image can be enhanced using external agents. Gold nanoparticles conjugated with an antibody have been used to enhance optical absorption (and photoacoustic signal) in targeted cancer tissue and provide high contrast for noninvasive cancer imaging using PAI.[21,52–54] In this study, a single layer of stimulated and unstimulated ECs labeled with bioconjugated gold nanorods (GNRs) were imaged using PAI.

2.2 Experimental section

Human umbilical vein endothelial cells (HUVECs) were maintained on gelatin-coated tissue culture plates in MCDB131 media (Gibco) supplemented with microvascular EC growth factors (Cambrex). Cells were split into a six well plate (0.1×10^6 cells/well, 38 mm in diameter) two days prior to an experiment. Media were changed 24 h after splitting and the cells were left unstimulated or stimulated with the proinflammatory cytokines Interferon-gamma (IFN-γ) (200 ng/mL, Peprotech) and TNF-α

(25 ng/mL, Peprotech) for 16 h. For photoacoustic and fluorescence microscopy measurements, the HUVEC monolayer was washed with cold MCDB131 media. Cells were blocked for 30 min at 4 ℃ in blocking media [MCDB131 1% bovine serum albumin(BSA) 1% horse serum(HS)]; the blocking solution was removed and the cells were incubated for 1 h at 4 ℃ with GNR-conjugated anti-ICAM-1 (Biolegend) or isotype control antibody and diluted fivefold with blocking media. The staining solution was removed and the cells were washed with MCDB131. Monolayers were fixed in 4% paraformaldehye in phosphate-buffered saline PBS for 1 h at room temperature, then washed and stored in PBS at 4 ℃. To confirm ICAM-1 expression in HUVECs, cells were counterstained for 1 h at room temperature with a fluorescein isothiocyanate FITC-conjugated goat antimouse IgG anti-serum 0.5 µg/mL in PBS/1% BSA/1% HS, and the nuclei stained with Hoescht 33342.

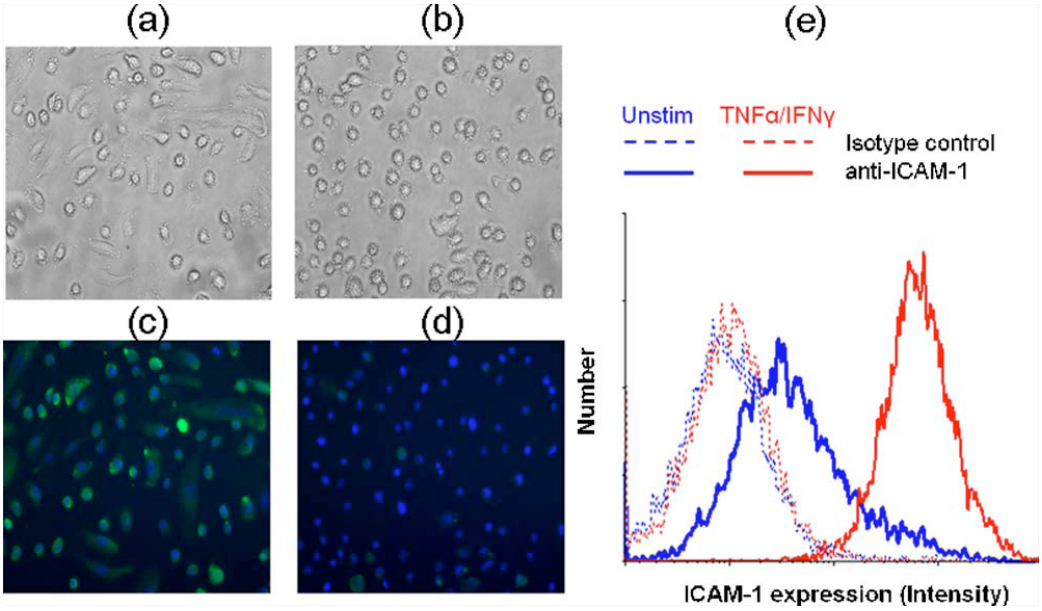

Figure 2.1: Microscope images of (A) stimulated and (B) unstimulated ECs. Fluorescence images of (C) stimulated and (D) unstimulated ECs. ICAM-1 is shown in green and nuclei are in blue. Immunofluorescent measurements were also performed using a flow cytometer (E). ICAM-1 expression reflects that the ECs are well stimulated (red solid line)

Fluorescence microscopy was performed using a Leica inverted microscope and

acquired images analyzed using ABODE PHOTOSHOP (Fig. 2.1). All images were acquired and processed using identical settings. From the same batch, a well of unstimulated or stimulated HUVECs was detached from the plate using trypsin, ethylenediaminetetra-acetic-acid(EDTA) solution, incubated for 0.5 h on ice in blocking media, and labeled with unconjugated anti-ICAM-1 or isotype control antibody (1 µg/mL). Labeled HUVECs were washed with MCDB131 then incubated with a FITC-conjugated goat antimouse IgG antiserum (0.5 µg/mL) in PBS. Levels and intensity of ICAM-1 expression were measured using a Coulter Epics XL flow cytometer and analyzed using WINMDI software (version 2.8) (Fig. 2.1).[55,56]

GNRs of aspect ratio of 3.5 were synthesized.[57,58] Their optical absorption was centered at 700 nm. Synthesized GNRs have a bilayer of surfactant hexadecyltrimethylammonium bromide (CTAB) on their surface acting as a stabilizer to prevent aggregation. After removing excess CTAB, the GNRs form a pellet at the bottom of the tube, which was redispersed in de-ionized water. A layer of Polyacrylic acid (PAA) is absorbed on the surface of GNRs by adding 1.5 mL of 1 mg/mL PAA solution to 1 mL of GNRs solution. Excess PAA in solution was removed by centrifugation and redispersion. The layer of PAA provides the -COOH functional group required for conjugation. PAA-coated nanorods were dispersed in 1 mL of PBS 6.0 buffer solution followed by the addition of 100 µL of 0.2 M (N-ethyl-N′-(3-dimethylaminopropyl)carbodiimide) EDC and 100 µL of 0.2 M (N-hydroxy-succinimide) NHS.[59–62] After 20 min, the reaction mixture was added to 20 µL of antihuman ICAM-1 or mouse IgG2a. The EDC/NHS mixture forms an active ester intermediate with the GNRs which undergoes amidation reaction with the -NH_2 group in the anti-ICAM-1 or IgG2a to yield the conjugate. The reaction mixture was refrigerated overnight after removing the unconjugated antibody.

Unstimulated or stimulated ECs were incubated with GNRs conjugated to anti-ICAM-1. Additional wells were incubated with GNRs alone with no antibody con-

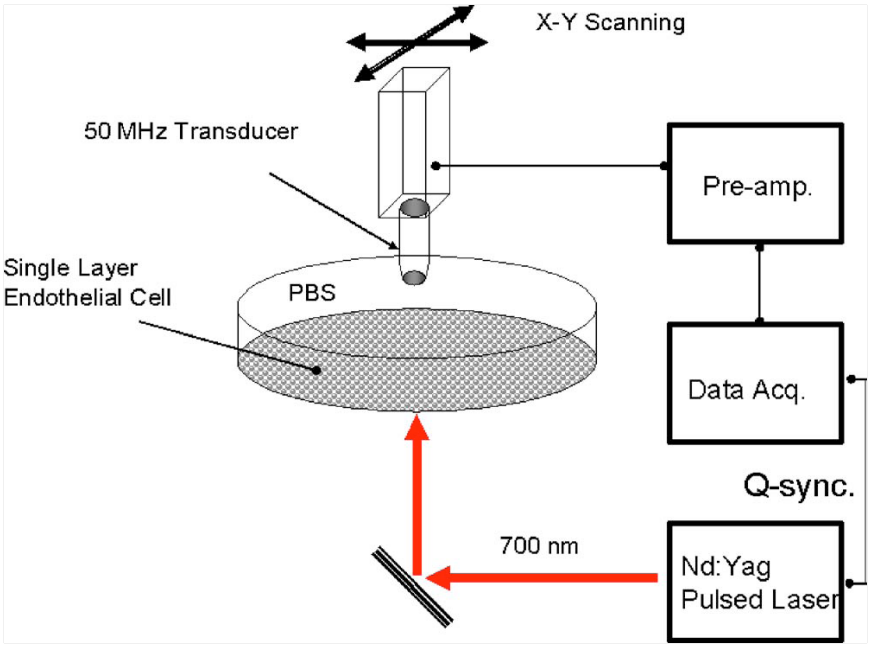

Figure 2.2: Photoacoustic imaging setup

jugation (blank nanorods). These wells serve as controls to estimate nonspecific binding levels of GNRs to cells. The concentration of the GNRs solution was 10^{12} particles/mL (10^3 particles/pL) for every case. The plate was then placed in the sample holder of the photoacoustic scanning setup depicted in Fig. 2.2. A pulse doubled neodymium doped yttrium aluminum garnet laser (Surelite I-20, Continuum, Santa Clara, CA) pumps an optical parametric oscillator (Surelite OPO Plus, Continuum) to generate 5 ns pulses at 20 Hz with 12 mJ pulse energy. The wavelength was tuned to 700 nm. The laser beam was directed to illuminate from the bottom of the cell culturing well (approximately 4 mJ/cm^2 fluence). A focused ultrasonic transducer (LiNbO3, 50 MHz, f/1.5) is used to detect the photoacoustic signal. A motorized X-Y stage was used to map the photoacoustic signal. For the map of cells bound with bioconjugated nanorods, the step size was 50 µm and the step size was 250 µm for the scan of cells bound with blank nanorods. The photoacoustic signal was averaged eight times at each scanning grid point. The transducer output was amplified (model 5910PR, Panametrics), digitized, and recorded by a digital oscilloscope (WaveSurfer

432, LeCroy Corp. Chestnut Ridge, NY) synchronized to the laser.

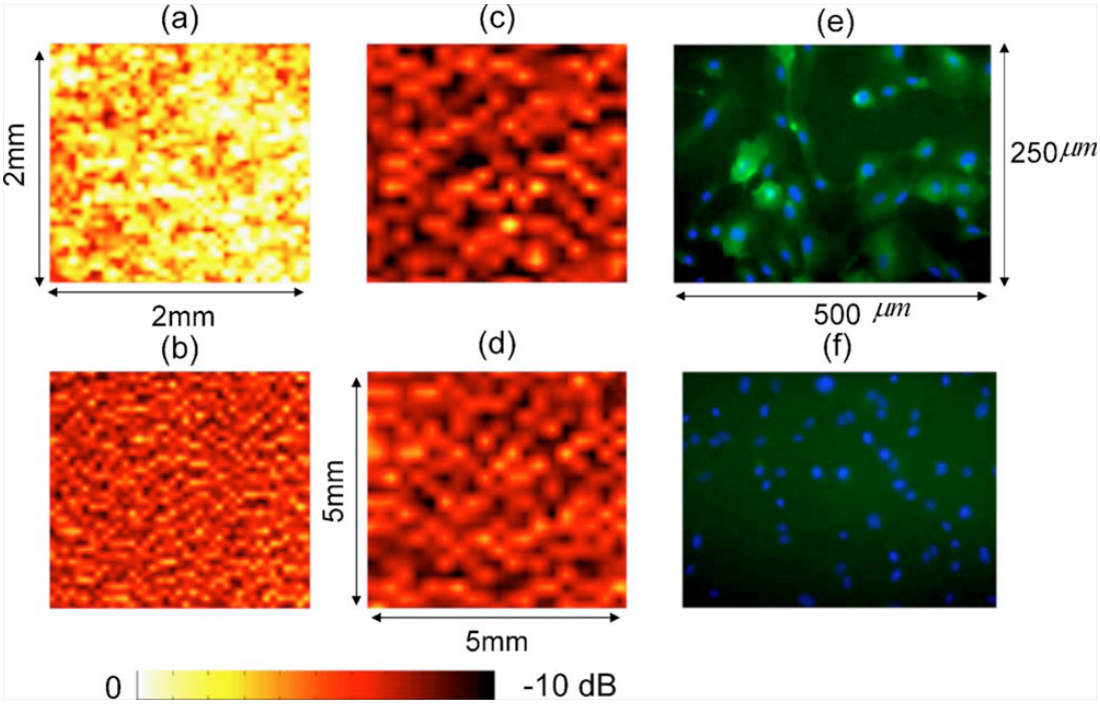

Figure 2.3: Photoacoustic images of (A) stimulated and (B) unstimulated ECs bound with bioconjugated GNRs, and (C) stimulated and (D) unstimulated ECs bound with blank GNRs. Note the scanning step was 50 µm for (A) and (B) and 250 µm for (C) and (D). Fluorescence images of the same ECs used for photoacoustic studies were also taken. The brightness of the fluorescent images differentiate (E) stimulated cell from (F) unstimulated cells and match well to the photoacoustic images (A) and (B). Images were taken over a 250×500 µm^2 around of the center of the photoacoustic images

2.3 Results and Discussion

Photoacoustic images are presented in Fig. 2.3. Photoacoustic intensity from the bioconjugated nano rods bound to stimulated cells was 10 dB higher on average than that from unstimulated cells. The photoacoustic intensity was also uniform over an extended scanning region of 2×2 mm^2. Scanned images at three different spots in the same well result in approximately the same average intensity and were uniform. The photoacoustic intensity from both stimulated and unstimulated cells bound with blank nanorods was insignificant compared to that from cells with bioconjugated nanorods.

This reflects very low nonspecific binding efficiency of blank GNRs to endothelial cells. The same ECs were then counterstained for 1 h at room temperature with a FITC-conjugated goat antimouse IgG antiserum and nuclei stained with Hoechst 33342. Fluorescence microscopy was performed using identical settings used above (Fig. 2.3).

The fluorescence intensity of the images differentiate stimulated from unstimulated cells and match well to the photoacoustic images presented in Fig. 2.3. Gold conjugated isotype control antibody did not show induction of photoacoustic signal upon HUVEC stimulation with TNF-α and (IFN-γ) (not shown), consistent with previous measurements by fluorescence microscopy and flow cytometer shown in Fig. 2.1.

2.4 Conclusions

In summary, the feasibility of molecular imaging of inflammatory responses is demonstrated. Bioconjugated gold nanorod contrast agents targeted stimulated ECs overexpressing ICAM-1 and produced a high contrast for photoacoustic imaging. These images clearly differentiate targeted inflamed cells from control unstimulated ECs. In combination with a commercial ultrasound platform, photoacoustic molecular imaging using GNRs as contrast agents can detect inflammatory response at very early stages in vitro and, potentially, *in vivo*. For *in vivo* applications, a proper laser light delivery system synchronized to an ultrasound platform needs to be developed. Minimum detectable gold nanorod concentration by a commercial ultrasound scanner (Sonix RP, Ultrasonix, BC, Canada) was estimated to be about 10^{11} particles/mL (10^2 particles/pL) in a gel phantom (agarose gel mixed with 5% intralipid). The optical absorption coefficient at this concentration is about 0.7 cm^{-1}. Early detection of inflammation could lead to prompt identification and monitoring of many different diseases. For applications in vascular diseases, light absorption by blood can be a

potential problem. The aspect ratio selectivity of gold nanorod absorption spectra will help this issue. In this study, the peak absorption was intentionally selected to be 700 nm where absorption by blood is minimum ($\sim$2 cm^{-1}).[63] At this wavelength, light can be delivered to some of the major arteries such as the carotid. Based on the absorption coefficient at minimum detectable concentration above, photoacoustic intensity enhancement of 10 dB can be expected for gold nanorod concentration of about 1.0×10^{12} particles/mL (1.0×10^{3} particles/pL). This corresponds to only about 500 nanorods per EC of 10 µm in diameter ($\sim$0.5 pL). In combination with an optical fiber light delivery system, conventional intravascular ultrasound can also access some other major arteries such as the coronary system.

CHAPTER III

Photoacoustic Imaging of Joints Aided by an Etanercept-Conjugated Gold Nanorod Contrast Agent-an *Ex Vivo* Preliminary Rat Study

3.1 Introduction

TNF has been identified as a protein produced by the immune system that plays a major role in the suppression of tumor cell proliferation. TNF-alpha overexpression has been found in patients with acute and chronic inflammatory arthritis both in disease target tissues and in the systemic circulation.[64–68] Because TNF has been implicated as one of the critical pathologic cytokines when over-expressed in the inflammatory cascade, much work has been done to inhibit or antagonize TNF. Three drugs inhibiting TNF, Etanercept (fusion protein), Adalimumab (D2E7) (human monoclonal antibody) and Infliximab, (chimeric monoclonal antibody) have been developed and are currently FDA approved for various types of inflammatory diseases. Although the role of pro-inflammatory cytokines such as TNF-α in the pathogenesis of inflammatory diseases has been shown to be significant, there is a large inter-and intra-individual variability in the level of cytokine expression.[69,70] Obtaining accurate information on cytokine expression in joints affected by inflammatory arthritis could be helpful in optimizing and/or evaluating the efficacy of biological drugs. Currently,

there is no noninvasive nonionizing molecular imaging modality with both high sensitivity and good spatial resolution which can enable drug delivery monitoring and therapeutic evaluation of inflammatory joint diseases.

The objective of this research is to realize molecular imaging and drug delivery monitoring for inflammatory joint diseases with both excellent sensitivity and high resolution by using novel PAI technology aided by the newly developed gold nanorod contrast agent. Gold nanoscale, and more specifically nanorod conjugates, also may have pharmaceutical benefits in light of the history of gold applications in various types of inflammatory arthritis. As an essential step toward our ultimate goal, in this study the bioconjugation between GNRs and Etanercept, an FDA-approved anti-rheumatic drug that inhibits TNF-α, was verified through ELISA experiment. The feasibility of PAI in imaging the distribution of the gold-nanorod-conjugated drug in regional articular tissues was also validated through the study on a rat tail joint model.

3.2 Experimental section

3.2.1 Imaging system

A PAI prototype system for joint imaging was employed in this study, as shown in Fig. 3.1.[71]

The wavelength of the laser light was tuned by the OPO to 680 nm, which is close to the absorption peak of the employed GNRs and enabled good penetration depth in biological tissues. For 2D imaging of a joint cross section, a circular scan was conducted with the sample rotated axially while keeping the transducer and the laser beam static. In order to cover a 2π angle of view, the circular scan was conducted at 240 positions with a constant interval of 1.5°. To reconstruct a photoacoustic image presenting the heterogeneous optical absorption in the sample, a modified back-

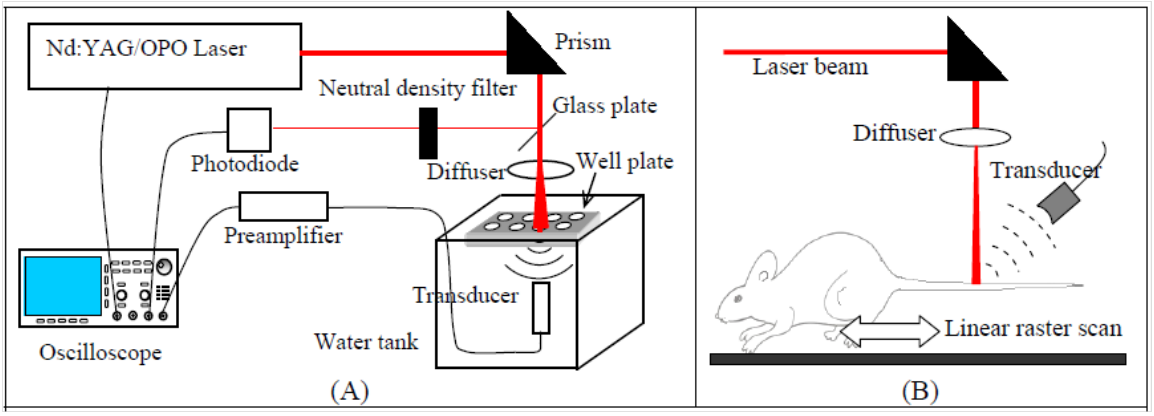

Figure 3.1: (A) Schematic of the PAI setup. (B) Scanning geometry on rat tail joints in situ

projection algorithm was employed.[7,26,72,73] The back-projection was performed in the time domain, where the positions of the absorbing objects were determined by the time-of-flight and the acoustic velocities in the sample. To reconstruct an image, the measured signals, after a derivative, were back-projected into the image space and then integrated over all receiving angles. The transducer (XMS-310, Panametrics) employed in this study had a central frequency of 10 MHz and a full width at half-maximum (FWHM) amplitude bandwidth of ~100%.

3.2.2 GNRs and anti-TNF-α conjugation

One of the key techniques involved in this study is the preparation of bioconjugates of GNRs with Etanercept molecules, complex anti-TNF-α antibodies. GNRs with average aspect ratio of 3 (45 nm by 15 nm) and an absorption peak at 660 nm were synthesized.[30,57,58] Both oxygenated- and deoxygenated-hemoglobin, the two major intrinsic absorbing substances in articular tissues, have comparatively low optical absorption in the spectra region between 650 and 720 nm.[74] By setting the absorption peak of GNRs in this region, we will have better imaging depth and enhanced signal-to-noise ratio in imaging the GNR-based contrast agent in the joint.

The synthesized GNRs have a bilayer of surfactant hexadecyltrimethylammonium

bromide (CTAB) on their surface which acts as a stabilizer to prevent aggregation. The GNRs have a net positive charge on their surface because of the stabilizer. Excess CTAB in the solution is removed by centrifugation at 5900 rpm for 60 min. The GNRs form a pellet at the bottom of the tube which was redispersed in deionized water. The GNRs are finally dispersed in deionized water to achieve a molar concentration of 0.01 M of gold in the solution. A layer of polyacrylic acid (PAA) is adsorbed onto the surface of GNRs by adding 1.5 mL of 1 mg/mL PAA solution to 1 mL of the gold nanorod solution.[30] The mixture is stirred for 3 h followed by two cycles of centrifugation and redispersion to remove excess PAA in the solution. The layer of PAA provides the -COOH functional group required for the conjugation. The PAA-coated GNRs are dispersed in 1 mL of PBS 6.0 buffer solution followed by the addition of 100 µl of 0.2 M EDC (N-ethyl-N-(3-dimethylaminopropyl) carbodiimide) and 100 µl of 0.2 M NHS (N-hydroxy-succinimide).[60–62,75,76] After waiting for 20 min, the reaction mixture is added to 12.5 mg of Etanercept. The EDC/NHS mixture forms an active ester intermediate with the GNRs which undergoes an amidation reaction with the -NH_2 group in the anti-TNF-α to yield the conjugate. The reaction mixture is stored in a refrigerator at 4 ℃ overnight following centrifugation and redispersion in the buffer to remove the unconjugated drug.

3.2.3 Sensitivity of PAI in detecting GNRs

Before the experiments on animals, we validated the maximum sensitivity of the current PAI system in detecting GNRs through a study on a well-controlled phantom. The GNRs were diluted with PBS buffer to a concentration of 10^8 nanorods/mL, that is of the order of 1 pM. Then the nanorod solution was injected into glass tubing with a 1.7 mm inner diameter which was put into the PAI system working at 680 nm. The orientation of the glass tubing was orthogonal to the ultrasound detection beam and the distance between the tubing and the transducer surface was 5 cm. The recorded

signal intensity as a function of time is shown in Fig. 3.2. The gold nanorod solution was injected from 400 s; before that time, the signal was from the background (i.e. saline). With concentration of the order of 1 pM, GNRs can be detected by the PAI system with a signal-to-noise ratio (SNR) up to 4.

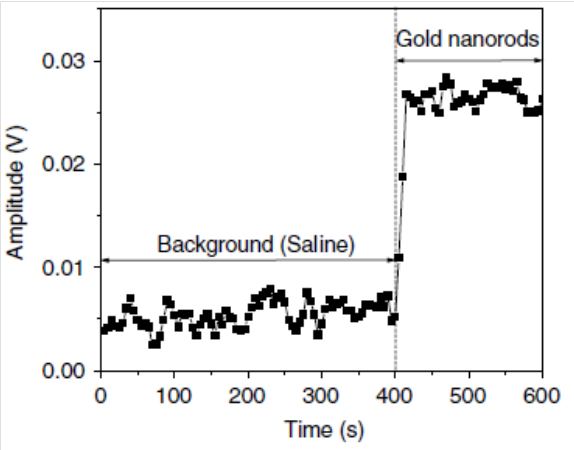

Figure 3.2: Photoacoustic signal from the gold nanorod solution with a concentration of 1 pM

3.2.4 ELISA experiment

An ELISA experiment was performed to prove the bioconjugation and to show that the anti-TNF-α drug conjugated with GNRs was still biologically active. Human TNF-α screening set purchased from ENDOGEN® was used. All experiments were performed in sterile conditions. The wells of the ELISA plate were coated with coating antibody and incubated overnight at room temperature. The coating antibody solution was aspirated next morning and 300 µl of blocking buffer (4% BSA, 5% sucrose in D-PBS buffer) was added to all the wells and incubated for 1 h. The blocking buffer was then aspirated and the plate was allowed to dry for 1 h. Using reagent diluents (4% BSA in D-PBS buffer) lyophilized human TNF-α was reconstituted to a concentration of 2000 pg/mL and coated onto the wells. After incubation for 1 h the wells were washed with wash buffer three times. The conjugated GNRs

were incubated for 1 h followed by three washes. Control experiments with unconjugated GNRs were also performed in parallel. To check for reproducibility/deviations in data, GNRs conjugated with Etanercept were placed in 18 wells, while the control (unconjugated GNRs) was placed in 10 wells. After three washes, absorbance of each well in the ELISA plate was measured using a microplate reader (ν max kinetic microplate reader, Molecular Devices).

3.2.5 Rat model

Rheumatic disease rat models, including those with inflammatory arthritis, have been researched extensively and provide the opportunity to evaluate pathologic progression much more quickly than in humans.[77–79] Rat tail joints, due to their approximate size and morphological similarity to human finger and toe joints, provide reasonable examples for research purposes. In total, four adult Sprague Dawley rats ($\sim$ 300 g, Charles River Laboratory) were included in this study. Whole tails were harvested from the rat bodies within 1 min after the rats were sacrificed. An electrocautery device (SurgiStat, Valleylab) was then used to clot blood and seal vessels. The rat tail was placed in the PAI system along the Z axis (see Fig. 3.1). The first proximal segment of the rat tail was fixed on a rotational stage that, driven by a stepper motor, could rotate the tail around its axis. The imaged joint was about 2.5 cm from the rat trunk, where the diameter of the tail was $\sim$8 mm and the length of a segment was $\sim$10 mm. Administration of Etanercept-conjugated GNRs was conducted intraarticularly through a needle. To obtain histological photographs, rat tails were saved in 10% buffered formalin for 3 days. Tails were then decalcified with formic acid for 4-7 days and monitored with a Faxitron MX-20 X-ray system. Once specimen decalcification was completed they were dehydrated with graded alcohol (Hypercenter XP by Shandon), embedded in paraffin (Paraplast Plus), cut into blocks and sectioned to 7 µm thickness with a Reichert-Jung 20/30 metal knife (paraf-

fin microtome). Hematoxylin and eosin staining of specimen sections on glass slides was conducted. Finally, the histological photographs of specimen sections were taken with a 10× magnification

3.3 Results

3.3.1 Outcomes of ELISA experiment

The absorbance of all the wells, including 18 wells where GNRs conjugated with Etanercept were incubated and 10 wells were unconjugated GNRs were incubated, are shown in Table 3.1. The average absorbance of gold nanorod-Etanercept wells is 0.132±0.028, while the average absorbance for control wells is 0.040±0.016. The absorbance by the conjugated GNRs is more than three times higher compared to the control experiment. This result clearly indicates that the GNRs are conjugated with Etanercept and the nanorod-Etanercept conjugate is still active with a high affinity for TNF-α.

	AuNR-Etanercept			Control	
	1	2	3	4	5
A	0.149	0.106	0.093	0.048	0.038
B	0.16	0.118	0.086	0.026	0.024
C	0.164	0.111	0.072	0.033	0.059
D	0.138	0.16	0.153	0.022	0.053
E	0.149	0.16	0.138	0.068	0.032
F	0.13	0.148	0.144		

Table 3.1: Absorbance of each well in the ELISA plate

After making the measurements with the microplate reader, the wells in the ELISA plate were also put in the PAI system working at 680 nm wavelength to examine the

sensitivity and accuracy of PAI in quantifying the optical absorption from the conjugated GNRs. Considering the possible inhomogeneity of the gold nanorod distribution in each well, PAI measurement of each well was conducted four times each at different locations. The average photoacoustic signal intensity and the standard error for each well is shown in Fig. 3.3, where photoacoustic (PA) measurements present a good linear relationship with the readouts from UV/vis ($p<.0001$).

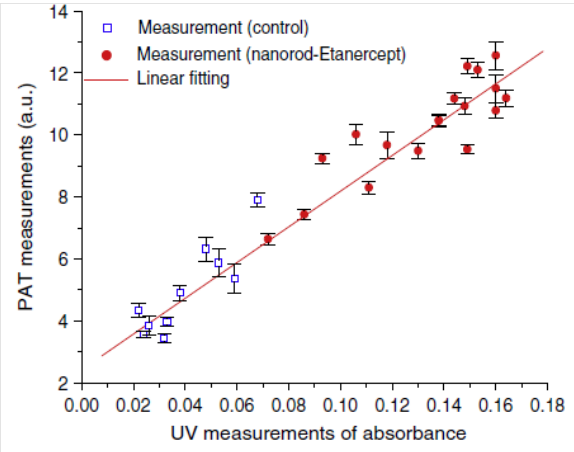

Figure 3.3: Photoacoustic measurements of the optical absorbance of ELISA wells in comparison with the UV/Vis readouts

The small discrepancy between PAI results and UV/vis readouts may come from the fluctuation of laser energy and the inhomogeneous distribution of GNRs in each well. Besides the good correlation between PAI and UV/vis outcomes, we can also see clearly the difference between the PAI results from the GNRs-Etanercept conjugates and those from the control.

3.3.2 Imaging on rat tail joints

2D photoacoustic cross-sectional imaging of rat joints in situ was conducted with laser light at 680 nm. Fig. 3.4 shows an example A-line of the photoacoustic signal from the imaged rat tail joint. The signal from the GNRs diffused in intraarticular connective tissue can be recognized with an excellent SNR of up to 17, where the

amplitude of the noise was measured from the background before the arrival of the signal from the tissue.

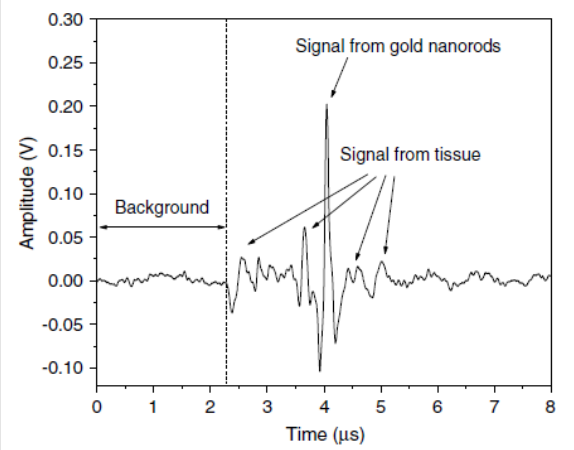

Figure 3.4: A-line photoacoustic signal from the imaged rat tail joint with the contrast enhanced by the GNRs

The image in Fig. 3.5(A) was taken before the administration of Etanercept-conjugated GNRs, while the images in Fig. 3.5(B)&(C) were taken after the first and the second administrations of the contrast agent. The injections were conducted intra-articularly through a needle via the direction indicated by the arrows in the images. For both the first and the second injections, 0.025 mL agent with a gold nanorod concentration of 10^9 nanorods/mL (i.e. 10 pM) was introduced. The total number of GNRs introduced into the regional joint space for each injection was of the order of 10^7. All the other experimental parameters for the images in figures 3.5(A)-(C) were the same, except that the specimen might be moved slightly during the administration of the contrast agent.

With the optical contrast enhanced by the GNRs, the contour of the intra-articular connective tissue is presented much more clearly in the images in Fig. 3.5(B)&(C) in comparison with the image in Fig. 3.5(A), which is based on the intrinsic tissue contrast. The hexagon shaped contour of the intra-articular connective tissue has been verified by the histological photograph of a similar cross section in a rat tail joint. The findings in Fig. 3.5(B)&(C) are also consistent: with more GNRs injected and

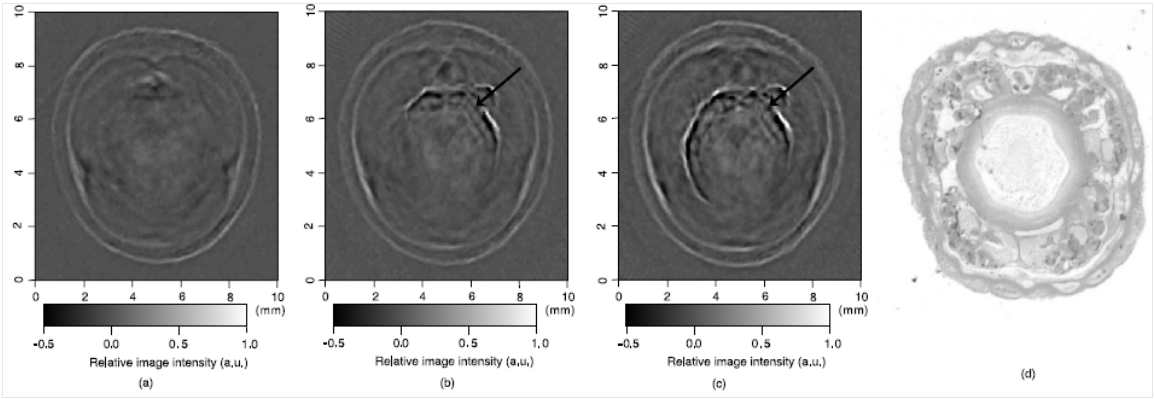

Figure 3.5: 2D cross-sectional PAI of a rat tail joint. (A) Image based on intrinsic contrast, which was taken before the administration of the contrast agent. Images taken after (B) the first and (C) the second administration of Etanercept-conjugated GNRs. For each administration, 0.025 mL agent with a 10 pM concentration was injected intra-articularly through the arrows in the images. (D) Histological photograph of a similar cross section in a rat tail joint showing the morphological features including intra-articular tissue, vessels and muscle

diffused in the intra-articular connective tissue more areas of tissue were 'lightened'. This study has proved the capability of photoacoustic technology in tracing and quantifying goldnanorod-based contrast agents in biological tissues. With our current PAI system, the spatially distributed gold nanorod contrast agent with a concentration down to 10 pM in biological tissues can be imaged with very good signal-to-noise ratio and high spatial resolution.

3.4 Conclusions

In conclusion, this study demonstrates the feasibility of a gold nanorod contrast agent to enhance joint imaging utilizing novel PAI technology. PAI, by combining the merits of both light and ultrasound, overcomes some limitations of conventional optical and ultrasound imaging modalities. With our current system, PAI presents a maximum sensitivity of the order of 10 pM in imaging GNRs in conjugation with an anti-TNF-α drug. This sensitivity is parallel to conventional optical imaging in detection and quantifying a gold nanoparticle contrast agent.[80–82] Unlike conventional

optical technologies, the spatial resolution of PAI is excellent (of the order of 250 µm, and may be improved further by adjusting the detection bandwidth) in visualizing subsurface joint tissues and the spatially distributed contrast agent. The good resolution of PAI especially benefits the imaging of drug delivery and treatment effects in peripheral joints which are among the earliest to be affected by rheumatoid arthritis and are widely accepted to be the best markers of overall joint damage.

With further development of PAI technology, highly sensitive imaging of drug delivery in combination with high resolution high contrast anatomical imaging may be achieved through a single exam without the need for image fusion. PAI may enable investigators to follow the drug and/or the delivery vehicle on its journey through the body to ascertain whether successful drug uptake is occurring in the desired organ, such as arthritic joint tissues. Moreover, the good sensitivity of PAI to joint tissue morphological changes and functional hemodynamic changes may also make this technology promising in the evaluation of treatment efficacy. Other advantages of PAI which will also benefit laboratory research and future clinical practice involving molecular imaging include being nonionizing and relatively cheap when compared to other modalities such as magnetic resonance imaging and nuclear imaging.

In future studies, PAI of drug delivery monitoring will be conducted on arthritic animal models *in vivo* with systemic administration of drug-conjugated GNRs. Efficacy and toxicity of such applications will also be studied. Moreover, a multi-channel ultrasound unit with a well-designed ultrasonic array transducer will be employed to replace the single-element transducer for image acquisition. With this more advanced imaging system, the sensitivity and resolution as well as the speed of PAI for molecular imaging may be improved significantly.

CHAPTER IV

Dual Mode Imaging with Radiolabeled Gold Nanorods

4.1 Introduction

Nanoparticle bioconjugates represent contrast agents for a variety of imaging and treatment techniques which take advantage of unique light-absorption, emissive, or magnetic properties of quantum confined solids.[83–87] One of them, photoacoustic imaging (PAI), is a non-ionizing, non-invasive biomedical imaging modality which combines the merits of both light and ultrasound.[8,9,16,34] In PAI, a short pulsed laser is used to illuminate the tissue and generate photoacoustic waves due to thermoelastic expansion. The laser generated signal is then measured by broadband ultrasound transducer(s) to reconstruct the image in the tissue sample. PAI is highly sensitive to the optical absorption contrast in the tissue; while its spatial resolution is limited mainly by ultrasound detection rather than by the overwhelming light scattering as in diffuse optical imaging.

Despite the variety and relative effectiveness of PAI contrast agents available, there is an inherent disadvantage in PAI measurements due to the strong attenuation of light in biological tissues as well as the high background signal as a result of intrinsic tissue optical absorption. PAI presents local spatial resolution on the sub-millimeter

level however the penetration depth limits its ability to make measurements with satisfactory signal-to-noise ratio deep inside the tissue. In fact, the same problem is present for all nanoparticle contrast agents based on optical emission, which became increasingly popular recently.[88,89] This inherent problem of light emission can be overcome indirectly by merging it with another imaging modality which can provide high signal-to-noise ratio even deep inside the tissue and assist to validate the findings of the other technique.

In this study, we have successfully fabricated a targeted optical and nuclear dual-modality agent by radiolabeling GNRs with [^{125}I] to monitor anti-TNF-α drug delivery. The high contrast-to-noise ratio and good quantification of nuclear imaging provide a gold standard and assist to validate PAI findings; while PAI helps overcome the spatial resolution limitations of nuclear imaging and demonstrates regional information with improved accuracy. As demonstrated in our initial experiments on rat joints in situ, the distribution of radiolabeled GNRs in articular tissue can be presented by both PAI and Single-Photon Emission Computed Tomography (SPECT). Moreover, by covalent binding of radioisotopes on the surface of targeted gold NPs, nuclear imaging such as PET and SPECT can for the first time image the concentration and distribution of gold NP based agents *in vivo*, which could contribute considerably to understanding of the toxicity and pharmacokinetics of any novel gold nanocolloids in the future.

4.2 Experimental Section

4.2.1 PAI setup

The photoacoustic experimental setup is given in Fig. 3.1. Laser pulses from an optical parametric oscillator (OPO) (Vibrant B, Opotek) pumped by an Nd:YAG laser (Brilliant B, Bigsky) were used to illuminate the sample, either a ELISA well

plate as in Fig. 3.1(A) or joints in a rat tail as in Fig. 3.1(B). The laser pulse repetition rate was 10 Hz and each pulse had a width of 5.5 ns. The laser wavelength was tuned to 760 nm, the absorption peak of the GNRs. An optical diffuser was used to expand the laser beam to cover a well or a joint completely. The energy density of the laser pulses incident at the sample was adjusted to less than 10 mJ/cm^2, within the ANSI safety limit. A part of the laser beam was reflected off by a glass plate and was measured by using a photodiode in order to take into account the incident light energy and the laser fluctuation. Neutral density filters were placed in the beam path to limit the maximum amount of light enter into the photodiode. For the experiment on ELISA well plate, an unfocused ultrasonic transducer (XMS-310, Panametrics) with a central frequency of 10 MHz, -6 dB bandwidth of 133% and a diameter of 2 mm was used to collect the photoacoustic (PA) signals from the illuminated well. Part of the well and the transducer were immersed in water for acoustic coupling. For the imaging of rat tail joints, a focused transducer (V312, Panametrics) with a central frequency of 10 MHz, -6 dB bandwidth of 130%, a diameter of 0.25 inch, and a focal length of 0.75 inch was used to conduct a raster scan along the length of the tail. PA signals received by the transducer were amplified (PR5072, Panametrics) and sent into one channel of a digital oscilloscope (TDS 540B, Tektronics) which was triggered by the laser firing. The signal from the photodiode was sent into another channel of the oscilloscope. The signals received by the oscilloscope were digitized, collected and stored in a computer for processing and analysis. The amplitude of the PA signal was divided by the photodiode signal amplitude to get the photoacoustic response.

4.2.2 Gamma imaging setup

Radionuclide imaging was performed using the Gamma Imager (Biospace Lab, Paris). The planar imaging for ELISA experiments was performed with Gamma

Imager detection area facing upwards and a ELISA well plate was placed directly on the parallel hole collimator 1.3/0.2/20 (hole diameter/septum thickness/height in mm). 15 minute duration image was acquired using energy window 15-70 KeV, and the image was then displayed and quantified using Gamma Vision+ software (Version 3.0). Radioactivity was determined by drawing regions of interest (ROI) and calculated based on standard curve, which is generated by scanning a series of standards with known radioactivities.

4.2.3 MicroSPECT/CT

SPECT/Computed Tomography (CT) was performed using a pair of collimators (1.3/0.2/35) stand up to orient the detection area towards the animal (rat tail). The rat tail was fixed on a holder and aligned parallel to the face of detector. After 36 minutes CT scan, a 30 minute gamma imaging was acquired and 2D image was reconstructed using Gamma Acquisition software. The reconstructed fusion image of SPECT/CT could be displayed and quantified using Amira software (Version 3.1).

4.2.4 Synthesis of the GNRs

GNRs are synthesized by a method modified from literature.[57,90–92] Briefly, a seed solution is prepared by reducing Gold (III) Chloride (25 µL, 0.05 M) in Hexadecyltrimethyl ammonium bromide (4.7 ml, 0.1 M) by addition of freshly prepared Sodium Borohydride (0.3 ml, 0.01 M) under vigorous stirring. An aliquot of seed solution (0.24 mL), is added to the growth solution containing Hexadecyltrimethyl ammonium bromide (100 mL, 0.1 M), Gold (III) Chloride (1.0 ml, 0.05 M), Hydrochloric acid (2 mL, 1 M), Ascorbic acid (0.8mL, 0.1 M)and Silver Nitrate (1.2 mL, 0.01 M). The glass beaker is placed in a water bath maintained at 27 ℃ for three hours to complete the synthesis. 50 mL aliquots of the synthesized rods are centrifuged at 10000 rpm for 1 h to obtain pellet of GNRs at the bottom of the tube.

Supernatant is decanted and the pellet is redispersed into 5 mL of deionized water to get a concentration of 10^{13} rods/mL. GNRs with average aspect ratio of 4 are obtained with transverse plasmon peak at 525 nm and longitudinal plasmon peak at around 800 nm. The position of the longitudinal plasmon peak can be fine tuned fairly easily within 600-900 nm range by varying the content of silver nitrate during synthesis.

4.2.5 Gold nanorods and anti-TNF-α conjugation

Bioconjugation was performed by a slightly modified method previously published by our group.[36–38,60–62,93] A layer of polyacrylic acid (PAA) is adsorbed onto the surface of GNRs by adding 1.0 mL of 1 mg/mL PAA solution to 1 mL of the prepared GNRs solution. The mixture is stirred for 3 hours followed by centrifugation to remove excess PAA in the solution. The layer of PAA provides the -COOH functional group required for the conjugation. The PAA-coated GNRs are dispersed in 1 mL of deionized water followed by the addition of 100 µL of 0.2 M EDC (N-ethyl-N-(3-dimethylaminopropyl) carbodiimide) and 100 µL of 0.2 M NHS (N-hydroxysuccinimide). After waiting for 20 min, the reaction mixture is added to 12.5 mg of Etanercept, an FDA approved biologic disease modifying anti-rheumatic drug (DMARD) targeting TNF-α. The EDC/NHS mixture forms an active ester intermediate with the GNRs which undergoes an amidation reaction with the -NH_2 group in the anti-TNF-α to yield the conjugate. The reaction mixture is stored in a refrigerator at 4 ℃ overnight following centrifugation and redispersion in deionized water to remove the unconjugated drug.

4.2.6 Radiolabeling of GNRs with ^{125}I

[^{125}I] Radionuclide in 10^{-5} M NaOH (pH 8-11) purchased from PerkinElmer (100 mCi/mL) was diluted with deionized water. The concentration was determined upon

radioactivity. GNRs (either blank or conjugated with drug) dispersed in fresh deionized water (0.5 mL, 10^{13} rods/mL) was added to 0.5 mL diluted [^{125}I] sodium iodide. The mixture was shaken for 30 minutes at room temperature. The [^{125}I]-iodine labeled GNRs were then washed with deionized water by centrifugation and redispersion.

4.2.7 Outcomes of ELISA experiment

Human TNF-α screening set purchased from ENDOGEN® was used. All experiments were performed in sterile conditions. The wells of the ELISA plate were coated with coating antibody and incubated overnight at room temperature. The coating antibody solution was aspirated next morning and 300 µL of blocking buffer (4% BSA, 5% sucrose in D-PBS buffer) was added to all the wells and incubated for 1 hour. The blocking buffer was then aspirated and the plate was allowed to dry for 1 hour. Using reagent diluents (4% BSA in D-PBS buffer) lyophilized human TNF-α was reconstituted to a concentration of 2000 pg/mL and 100 µL was added into the wells. After incubation for 1 hour, the wells were washed with wash buffer three times. 100 µL of GNRs conjugated with drug were added into each alternating well in Row A; 100 µL GNRs conjugated with drug and radiolabeled (30 µCi) were added into each alternating well in Row C; 100 µL radiolabeled (30 µCi) GNRs into each alternating well in Row E; and 100 µL blank GNRs into each alternating well in Row G. In each row, 4 alternating wells were used in order to average the results. After incubating the samples for 1 hour, the 96 well plate was aspirated and washed with washed buffer three times. The dried plate was analyzed with PAI setup and Gamma imager.

4.2.8 Rat tail joint model

The GNRs concentration in original solution is 10^{13} rods/mL. The original solution was diluted 40 times first with distilled water and then 0.2 mL of solution

was mixed with 0.5 mL of I-125 with radioactivity of 400 µCi for 30 min using a ROTAMIX rotates (Appropriate Technical Resources, Inc., Laurel, MD). The mixture was centrifuged for 4 min at the speed of 5000 cpm in 1 mL tube. Then the radiolabeled GNRs at the bottom of the tube were taken out and diluted again to 0.3 mL with distilled water (∼320 µCi). Therefore, in this solution (named agent #1), the GNRs concentration was 10^{11} rods/mL (i.e. 2×10^{-10} M or 200 pM). After the agent #1 was made, 1 mL of solution was diluted 1:1 with distilled water which makes agent #2 with a GNRs concentration of 1×10^{-10} M (or 100 pM). After that, 1 mL of agent #2 was diluted further 1:1 with distilled water to get agent #3 with a GNRs concentration of 5×10^{-11} M (or 50 pM). As shown in Fig. 4.3(A), 0.02 mL of contrast agents #1, #2 and #3 were injected intra-articularly in every other joint in the rat tail; while same amount of water (i.e. 0.02 mL each) was injected in the other two joints as control. The estimated total amounts of GNRs injected in the three joints were 2×10^{9}, 1×10^{9} and 5×10^{8}, respectively. Considering that some of the GNRs may stay in the upper medium in the tube after centrifuge, the actually number of GNRs injected should be mildly lower. Measured with a Capintec dose calibrator (CRC-543X, Capintec Inc., Ramsey, NJ), the total radioactivities of GNRs injected in the three joints were 15.2 µCi, 7.4 µCi and 3.6 µCi, (roughly at a ratio of 4:2:1)

Whole tails of euthanized rats were imaged. An optical beam with size of 1 cm in diameter and wavelength at 760 nm illuminated the imaged rat tail and generated photoacoustic signals that were acquired with the focused V312 Panametric transducer. The distance between the transducer and the rat tail was about 19 mm which was also the transducer focal length. Considering an f-number of 3 and, the estimated lateral resolution was about 0.55 mm; while the estimated axial resolution was about 0.12 mm. In order to acquire a 2D image along a sagittal section of the tail, the tail immersed in water for ultrasound coupling was positioned through a computer con-

trolled stepper motor while the transducer and the laser beam were kept static. The scanning step was 0.6 mm (similar to the lateral resolution) and the scanning period was 60 mm (i.e. 100 steps). The total period for photoacoustic signal acquisition was about 10 min when the signal at each scanning position was averaged over 50 laser pulses to achieve better signal-to-noise ratio.

4.3 Results

4.3.1 Radiolabeling of GNRs with ^{125}I

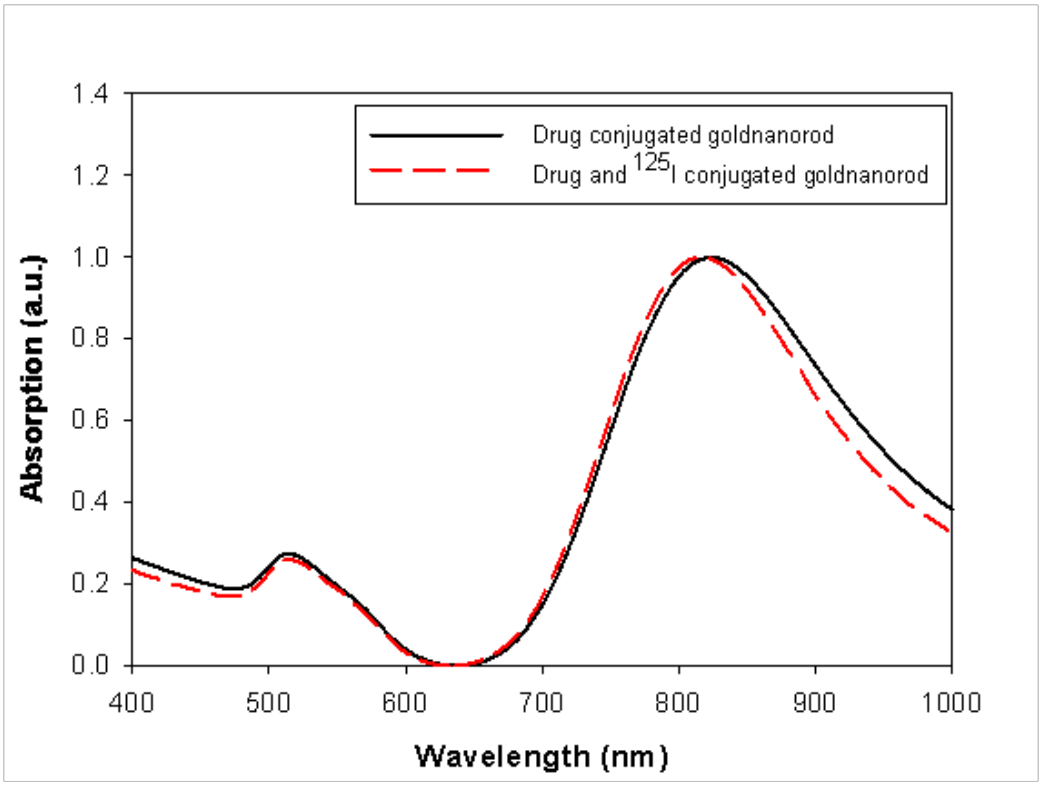

Figure 4.1: UV-Vis spectra of the GNRs solution before and after radiolabeling the drug conjugated GNRs with ^{125}I

The radiolabeling procedures are simple and reliable, with radiochemical yields greater than 80%. GNRs were found to be stable after binding with radioactive iodine. This agreed well with published data which claims that there is high affinity

and strong binding of iodide ions to the surface of GNRs.[94] Figure 4.1 shows the UV-Vis absorption spectra of the GNRs conjugated with drug before and after addition of radioactive iodine. The minor blue shift in the spectrum is due to the change in the surrounding of the GNRs surface due to addition of iodine molecules.

4.3.2 ELISA experiment

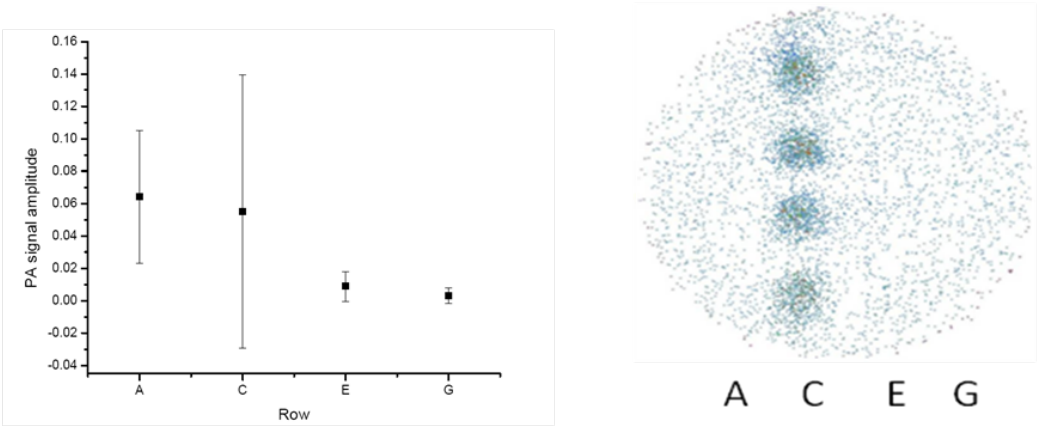

Figure 4.2: Left: Mean ± standard deviation of photoacoustic signal intensity measured from each row of the ELISA plate. Right: γ-camera image of the ELISA plate. Row A contains (GNRs + drug) Row C contains (GNRs + drug + ^{125}I); Row E contains (GNRs +^{125}I); and Row G contains (GNRs). The photoacoustic signal and radioactive image correspond very well

ELISA experiment has been performed to evaluate the biological activity and the specific binding of the synthesized contrast agent carrying anti-TNF-α, which is an important therapeutic agent against arthritis. Row C with radiolabeled conjugated GNRs showed strong signal in both gamma imager and photoacoustic measurements (Fig. 4.2). The control in row E had very weak photoacoustic amplitude (PA) signal and nearly zero radioactivity because the GNRs lacked the anti-TNF-α drug on their surface to cause specific binding on the well plate. Row A with GNRs conjugated with drug showed similar photoacoustic signal amplitude as row C but no radioactivity because it was not radiolabeled with ^{125}I. Another control of row G with blank GNRs also had very weak photoacoustic signal and nearly zero radioactivity. The finding

from the ELISA experiment concludes that the drug conjugated with ^{125}I labeled GNRs retains its biological activity and forms a highly specific system. The ratio of photoacoustic signal for specific (average PA amplitude from area under row C) to non-specific binding (average PA amplitude from area under row E) for the targeted radiolabeled GNRs contrast agent was 6:1. The ratio of signal intensity in the γ-camera image for specific (average intensity from area under row C) to non-specific binding (average intensity from area under row E) for the targeted radiolabeled GNRs contrast agent was 6.125:1. This also shows a strong one to one correspondence in results obtained respectively from the photoacoustic and nuclear imaging setups.

4.3.3 Imaging results on rat tail joints

After the first photoacoustic image was taken (Fig. 4.3(B)), intra-articular injections of contrast agent and water were conducted. Then the second photoacoustic image was taken, as shown in Fig. 4.3(C). The signal enhancement can be seen in the three joints with injected radiolabeled GNRs contrast agent; while no noticeable change can be seen in the two joints with water injected. The maximum signal intensities in the three marked areas in Fig. 4.3(C) show a ratio of 1.16:0.60:0.27 that is close to ratio among the doses of injected contrast agent in the three joints (i.e. 4:2:1). After photoacoustic data were acquired, the rat tail was placed in our microSPECT/CT system. The 2D images of SPECT and CT are shown in Fig. 4.3(E) and Fig. 4.3(A), respectively. As shown in Fig. 4.3(A), the acquired 2D microCT image of the sagittal section of the rat tail shows clearly the bone structure. This microCT image was then fused with the photoacoustic image in Fig. 4.3(C). In the microCT and photoacoustic combined image in Fig. 4.3(D), photoacoustic image presents the distribution of contrast agent and some soft tissue structures; while the microCT image describes detailed bone structure in the tail. With the morphological information presented by the microCT image, we can see clearly that the positions of

signal enhancements in the photoacoustic image were at the intra-articular connective tissues in the three joints containing the contrast agent.

As shown in Fig. 4.3(E), when the GNRs concentration in the target tissue was on the order of 10 pM, the radioactivity from ^{125}I conjugated with the GNRs was sufficient to enable nuclear imaging with excellent signal-to-noise ratio. The counted radioactivities in the three joints with injected contrast agent were 4939, 2702 and 1453 counts/min respectively. The ratio among them is also close to that among the contrast agent doses in the three joints (i.e. 4:2:1). In Fig. 4.3(F), nuclear imaging is fused with the microCT image presenting both the distribution of contrast agent and the morphological tissue structures.

4.4 Discussion

Non-invasive monitoring of drug delivery in experimental models and in clinical settings would undoubtedly be very helpful for both basic research and pharmacologic management of a variety of diseases including rheumatoid arthritis. In this work, by imaging the ^{125}I labeled GNRs, both PAI and SPECT have successfully presented the distribution of GNRs conjugated anti-rheumatic agent in intra-articular connective tissues. In comparison with PAI, nuclear imaging should be superior in whole body imaging and in quantification due to good tissue penetration of γ-rays. However, the target specificity of nuclear imaging can be compromised due to its limited spatial resolution. In contrast, PAI presents spatial resolution on the sub-millimeter level (or even micrometer level by performing photoacoustic microscopy) and, hence can be superior in localizing contrast target taken up by regional target tissues.[95,96] The measurements from PAI, however, is difficult to be quantified, mainly due to the strong attenuation of light in biological tissues as well as the high background signal as a result of intrinsic tissue optical absorption. For the same reasons, we expect that PAI is also inferior in contrast-to-noise ratio compared to nuclear imaging in detecting radi-

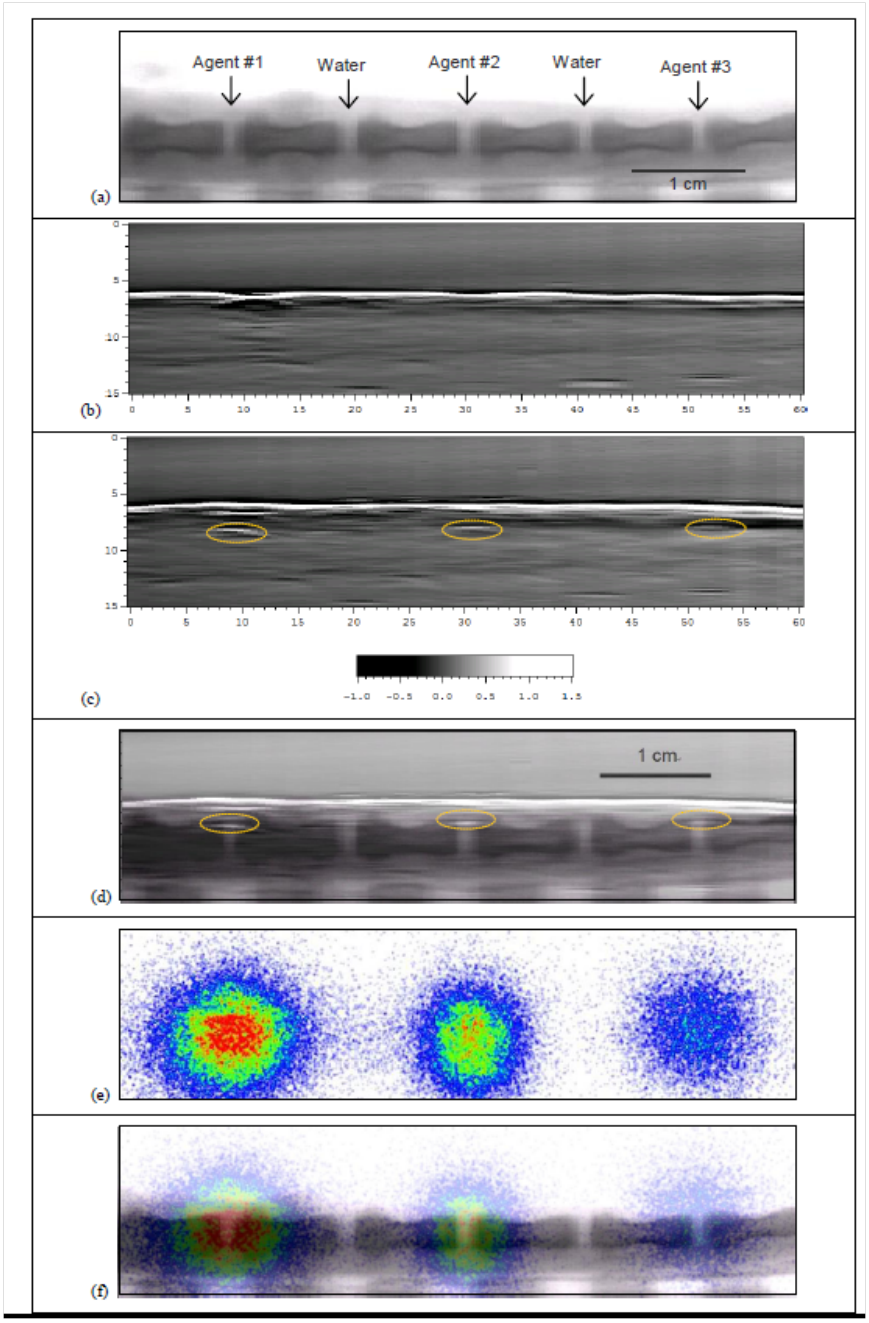

Figure 4.3: *In situ* imaging of radiolabeled GNRs contrast agent in rat tail joints. (A) MicroCT image of a sagittal section of a rat tail with joint sections clearly presented. As marked in the image, intra-articular injection of contrast agent or water as control was conducted in each joint. Photoacoustic image of the sagittal section in the rat tail (B) before and (C) after intra-articular injection of contrast agent. The signal enhancements in the three joints with injected contrast agent are marked with dashed ellipses. (D) The photoacoustic image in (C) fused with the microCT image in (A). (E) SPECT image of the sagittal section in the rat tail presenting the radioactivities in the three joints with the injected contrast agent. (F) The SPECT image in (E) fused with the microCT image in (A)

olabeled optical contrast agents. By fabricating the radiolabeled gold NPs conjugated with drug and performing the dual-modality imaging as described in this work, one may combine the advantage of high contrast-to-noise ratio and good quantification of nuclear imaging with the advantage of high spatial resolution of PAI. Moreover, as an emerging optical imaging modality, adaptation of PAI to functional and molecular imaging is still in the early stages and needs further development. With unparalleled high sensitivity, nuclear imaging especially when combined with microCT could provide a very powerful tool and gold standards to validate the imaging findings from novel PAI technique. On the other hand, while GNRs have been used extensively as optical contrast agents, the radiolabeling and use of NPs as SPECT agents have only recently been explored. NPs are well-suited to the design of SPECT probes, because their relatively large surface area (as compared with traditional small-molecules) can be labeled to a high specific activity. This allows for increased sensitivity of detection and increased payload of targeting ligands and therapeutic isotopes. Using the setups described above, we could image conjugated GNRs with a radioactive label of 5 µCi, down to a concentration of 10 pM in articular tissues. This provides evidences that the technologies of nuclear imaging and optical imaging are directly compatible and complementary.

Furthermore, we feel it is less likely that payloads including ligands and isotopes will significantly alter the natural progression of NPs through the body with exception to designed targeting. Obviously pharmacokinetic testing including *in vivo* evaluation of this contrast agent is needed to characterize how the agent in comparison to control and in pathologic settings such as inflammatory arthritis is treated by physiologic systems. Should the agent, due to its architecture with anti-TNF properties, localize to inflamed joints in the setting of inflammatory arthritis, in addition to monitoring of drug delivery it could be used to characterize quantitatively the degree of inflammation within each inflamed joint. This may be very helpful particularly in animal

and human studies. Limitations of use of this contrast agent in human studies include the amount of ionization subjected to patients and as already mentioned potential toxicities of NPs.

Radioactive iodine-labeled compounds have been used for decades in oncology, thyroid disorder, renal function, and inflammations. By providing functional information, nuclear imaging have shown advantages in identifying the present of abnormality where complex anatomy renders anatomic imaging (CT) less accurate. In addition, functional imaging is always necessary for pharmacokinetic study of new drugs. With the increasing proliferation of hybrid SPECT/CT recently, simultaneous acquisition of anatomic and functional information without alteration in patient position overcomes many of shortcomings and results in accurate localization and metabolic characterization of pathophysiological process. Introducing new radiopharmaceuticals and reintroducing older ones in the context of multimodality have considerably expanded. The potential benefits of combining SPECT/CT with PAI are great.

Radioactive gold nanoparticles have typically been synthesized in the past by bombarding neutron flux on Au-197 (100% isotopic abundance) to transmute into Au-198 by neutron capture, emitting prompt gamma.[97–100] The method of radiolabeling presented in this work is much more simpler, green and requires no sophisticated equipment. Au-198 and Au-199 with strong bate-emitting provide destructive power to kill cancer cell as therapeutic agents. However, there will be a large unnecessary radiation dose to the patient if used as imaging agents. I-125 with pure gamma-emitting apparently is more suitable for imaging utilization. In addition, radioactive iodine is also readily available as I-123 (gamma-emitter) for SPECT, I-124 (positron emitter) for PET, and I-131 (bate-emitter) for therapy. There is a great potential to achieve multiple applications with a single successful compound.

4.5 Conclusions

With intrinsic advantages including small sizes, ease of preparation and bioconjugation, unique optical properties, as well as good biocompatibility, gold NPs including GNRs have been explored for potentially wide application in drug delivery, cellular imaging, and biomedical diagnostics and therapeutics (theranostics). It was shown through the ELISA experiment in this study that the anti-TNF drug molecules keep their bioactivity after conjugation to ^{125}I radiolabeled GNRs and that the conjugated system is highly specific in binding with TNF molecules. Although this work was related to imaging, delivery and therapeutic action of anti-TNF-α, this technique of combining radiolabel functionality and other advantages of gold NPs is quite simple and stable and can easily be extended to targeted imaging of other disorders including cancer. By introducing the radiolabeled gold NPs, nuclear imaging could contribute to the understanding of how gold NPs interact with biological systems within the context of physiologically authentic environments, and could accelerate the clinical applications of these agents by helping to validate and optimize their diagnostic sensitivity, cellular uptake, toxicity, and molecular response. We expect that radiolabeled gold NPs could also become an efficient therapy agent with the combination of the power of radiation therapy and photothermal therapy. Further work is needed to produce more efficient imaging platforms compatible with animal and human use to study the pharmacokinetics and pharmacodynamics of this contrast agent.

CHAPTER V

In Vivo Biodistribution of ^{125}I-Labeled Gold Nanorods using γ-Imaging

5.1 Introduction

Nanoparticles, due to their small sizes and associated unique properties, have been widely used in drug delivery,[101–103] cellular imaging,[104–106] and biomedical diagnostics and therapeutics.[107–110] Plasmonic gold nanostructures possess intriguing physical and chemical properties which are of interest to both fundamental science and biomedical application.[111] Among the most fascinating and useful are optical properties as well as related photothermal properties.[112] These optical properties depend on nanoparticle size and shape.[113,114] One can manipulate the shape of gold nanostructures to control their electronic and associated optical properties for different applications.[115,116] Their remarkable capacity to absorb and scatter light at visible and near-infrared (NIR) regions is essential for optical imaging.[117] In addition, gold nanoparticles can convert optical energy into heat via nonradiative electron relaxation dynamics which endows them with intense photothermal properties.[118–121] Such localized heating effects can be directed toward the eradication of diseased tissue, providing a noninvasive alternative to surgery.[122] Current nanotechnology research suggests that gold nanoparticles form a novel class of optically active dual imaging-

therapy agents.[123–125]

In particular, gold nanorods (GNRs) have attracted much interest because of their small sizes, ease of preparation and bioconjugation, strong absorbing and scattering properties, as well as their well-known biocompatibility.[111,117,126] GNRs with well-defined shapes and sizes are readily synthesized by seeded growth methods, and their longitudinal plasmon resonances (LPRs) can be finely tuned as a function of aspect ratio.[37,111,126] GNRs support a larger absorption cross-section at NIR frequencies per unit volume than most other nanostructures and have narrower line widths due to reduced radiative damping effects with consequently higher optothermal conversion efficiencies.[117,118,127] The LPRs can also support nonlinear optical effects, such as plasmon-enhanced two-photon luminescence (TPL).[117,128] The LPRs are also sensitive to the polarization of the incident excitation; by slightly adjusting the wavelength of a continuous-wave (cw) polarized laser, individual GNRs can be aligned for several minutes in an optical trap.[129] These properties give rise to many exciting possibilities to deploy GNRs for biological imaging and photothermal therapy.[117] Furthermore, the surface chemistry of GNRs allows multiple functionalizations. Capping molecules, such as cetyltrimethylammonium bromide (CTAB), can be replaced or conjugated with many functional groups.[130,131] Target specificity of GNRs can be imparted by tagging with certain biovectors, such as monoclonal antibodies,[132] receptor-specific peptides[111] and other compounds,[133] which can navigate them to desired organs or sites. Recent studies have successfully demonstrated that GNRs with strong near-IR absorption can be conjugated to molecules to facilitate delivery to the tumor for subsequent efficient cancer cell diagnostics and selective photothermal therapy simultaneously.[111,132]

To advance GNRs toward realistic clinical applications and to optimize their diagnostic sensitivity, payload, or therapeutic efficiency, it is becoming urgent to understand how they interact with biological systems and their biodistribution after admin-

istration via injection. Various in vitro studies have provided fundamental information as to how nanoparticle size and surface chemistry greatly impact their interaction with plasma proteins, cellular uptake, toxicity, and molecular response. However, the in vivo environment is far more complex than in vitro model systems.[132,134] For instance, blood contains a variety of ions, as well as proteins, lipids, hydrocarbons, and other components that may affect nanoparticle stability, functionality, and targeting.[132] Studying the stability and functionality of injected GNRs within the in vivo environment is technically challenging.

So far only very few studies have investigated the in vivo behavior of engineered nanostructures. Although multiple studies with polymer colloids had been performed,[135–137] only very limited biodistribution data are available specifically for gold colloids. A relatively recent paper indicates that gold nanorods 65 nm in length and 11 nm in diameter were found to accumulate primarily in liver, kidney, and spleen, which is consistent with macrophage capture.[131] Without surface coating, they were removed by the reticuloendothelial (RES) system from the circulation within 30 min, while after coating with PEG this time was extended to 72 hours. At the same time, a different recent report give data that are difficult to correlate with those cited above. For gold nanoparticles (NPs) 1.9 nm in diameter, which were injected into mice, retention in liver and spleen was low and circulation lifetime was several days.[138] The great difference in observations and controversies in the interpretation of the data is very difficult to explain and requires extensive investigation. The difficulties with evaluation of biodistribution, blood clearance and other key pharmacokinetic parameters of GNR and other NPs is, in large part, related to the lack of a convenient monitoring technique for their distribution within the body. Traditionally it was carried out by radioactive labels, but this technology is grossly underdeveloped for nanoparticles.

This study is the initial investigation of the in vivo behavior of [^{125}I]-iodine labeled gold nanorods, which represent nanoparticles with dual functionalities: plas-

monic and radioactive labels. The stability and metabolism pattern of radiolabeled GNRs in normal rats were successfully examined using γ-scintigraphy. Longitudinal biodistribution studies have been performed repeatedly in the same animal for up to 6 days, therefore decreasing sources of inter-individual variation while being efficient in terms of animal cost and ethical practice. Radiolabeling of GNRs allows systematic study of gold nanoparticles within in vitro and in vivo microenvironments, providing a highly efficient methodology for bioevaluation of different kinds of GNRs and their bioconjugates. The novel protocol reported here could be extensively useful for guidance of the design and the development of new target-specific gold nanoparticles.

5.2 Experimental section

5.2.1 Synthesis of PEGylated GNRs

GNRs of average aspect ratio 4, capped with hexadecyltrimethyl ammonium bromide were synthesized using the seed-mediated growth methods reported in the literatures.[90,91] After synthesis gold nanorods were centrifuged and redispersed in deionized water to a final concentration of 10^{12} rods/mL. Polyethylene glycol thiol molecules were dispersed in deionized water (1 mL, 50 mg/mL) and mixed with GNRs (1 mL, 10^{12} rods/mL). The mixture was allowed to react overnight, followed by centrifugation and redispersion of rods to a final concentration of 10^{12} rods/mL. The zeta potential of bare gold nanorods is +40 mV and after PEGylation is reduced to +8 mV (5000 mol. wt.) and +10 mV (20,000 mol. wt.)

5.2.2 Radiolabeling of GNRs

In general, 0.1 mL of GNRs with concentration of 10^{12} rods/mL in deionized water was placed into a polypropylene microcentrifuge tubes (1.5 mL) and 0.5 mL of diluted [^{125}I]NaI was added, roughly 300 µCi of radioactivity. The vial was ro-

tated on a ROTAMIX rotates (Appropriate Technical Resources, Inc. Laurel, MD). The mixture was then centrifuged at 5000 rpm using a Beckman Microfuge II. The supernatant was decanted and pellets were re-dispersed in 0.1 mL of fresh sterile filtered deionized water. Various reaction times of 2, 10, 20, and 30 minutes have been tested, as well as various centrifugation periods of 5, 10, 15 and 30 minutes. The optical absorption spectra of diluted GNRs in saline solution were measured before and after radiolabeling by using a spectrophotometer (Perkin Elmer, MA, USA) with the sample contained in a 1 cm pathlength plastic cuvette.

5.2.3 Stability of GNRs in blood circulation

The experiments were performed according to the guidelines of the University Committee on Use and Care of Animals, University of Michigan. Male Sprague-Dawley rats (∼250g) were purchased from Charles River Laboratories (Wilmington, MA). The rats were anesthetized using an isoflurane anesthesia machine. Two I.V. catheters were placed into lateral tail veins separately, one for injection of the ^{125}I-GNRs dose and another for extraction of blood samples. The catheters were rinsed with 0.2 mL of saline after injection and every extraction. ^{125}I-labeled gold nanorods prepared as mentioned above were injected into rats through a tail vein, about 120 µCi in 0.1 mL of water for each animal. 3 rats were used for each kind of GNRs. Blood samples (0.1 mL) were collected from another tail vein at set times, from 1 minute to 4 hour post-injection. Radioactivity in each blood sample was counted using a γ-counter (MINAXI Auto-gamma 5000 Series, Packard Instrument Co., Grove, IL).

5.2.4 Long-term biodistribution using γ-imaging

The same group of animals used for blood assays were imaged at set times between blood sampling. After the measurements in day 1, the animals were re-anesthetized and scanned once each day from day 2 to day 6 before they were sacrificed. Each

image was acquired in 5-minute on an anesthetized rat placed in anterior position over the parallel-hole collimator 1.8/0.2/20 (Hole diameter/septum thickness/height in mm) of a Gamma Imager (Biospace Lab, Paris). Radioactivity was then quantified by drawing regions of interest (ROI) using Gamma Vision+ software (Version 3.0). For each animal, ROIs were drawn around the liver/spleen and heart/lung and were saved to be re-used systematically for longitudinal follow-up.

5.3 Results and Discussion

5.3.1 Preparation of ^{125}I-labeled GNRs

GNRs of average aspect ratio 4, either bare or PEGylated, were radiolabeled by simply mixing with [^{125}I] sodium iodide in deionized water at room temperature. The reaction takes place very rapidly and completely, with radiochemical yields greater than 90% by radioactivity count. There were no significant differences observed when the mixtures of [^{125}I] sodium iodide and GNRs were mixed for 2, 10, 20, or 30 minutes prior to centrifugation. This agrees well with the prior reports of high affinity and strong binding of iodide ions to the surface of gold nanorods.[94,126,139] It has previously been reported that iodide ions may affect the shape and size of GNRs.[139] In our case, the concentration of iodide is extremely low and has no significant impact on the optical property of GNRs. Fig. 5.1 shows the absorption spectra of GNRs measured before and after radiolabeling. The longitudinal plasmon peaks remain unchanged in intensity after radiolabeling but show a small plasmon shift due to presence of additional iodine molecules on the surface. [^{125}I]-iodine labeled GNRs are stable for weeks when stored in the refrigerator.

The washing process using centrifugation is critical. Uncompleted centrifugation causes loss of radioactive GNRs in decanted supernatant, resulting in low radiochemical yields. On the other hand, the chance of irreversible nanorod aggregation increases

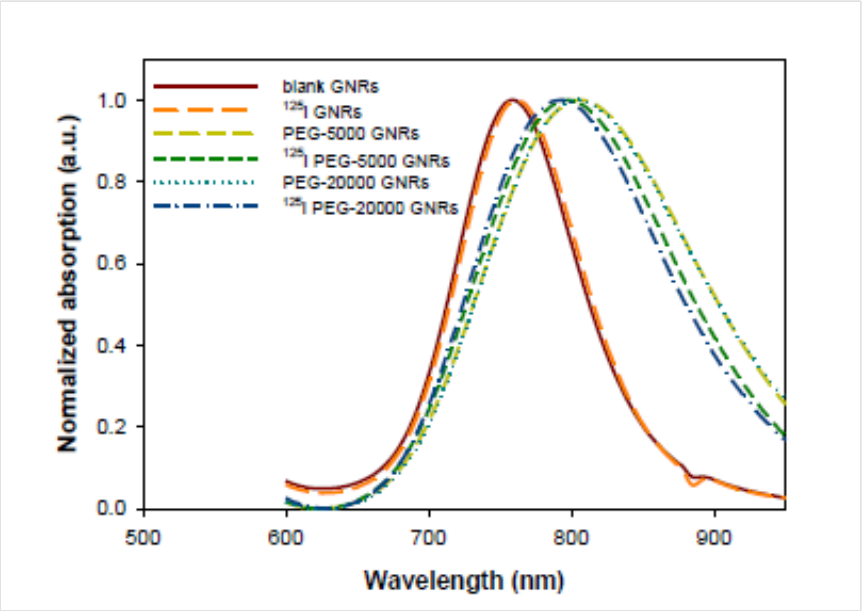

Figure 5.1: UV-Vis of GNRs before and after labeling with ^{125}I

when centrifugation period is extended. A series of experiments were performed to investigate and optimize the conditions. To minimize variations, radiolabeled GNRs were initially washed twice to remove free radioactive iodide and then dispersed in deionized water. Table 5.1 summarizes the percentage of radioactivity collected in pellets after centrifugation for various time periods. It should be noticed that a centrifugation time of 30 minutes at 5000 rpm is necessary to recover all GNRs. However, the possibility of failure to deliver desired product would then be over 30% due to irreversible nanorod aggregation. Therefore, one washing using 15 minutes centrifugation was applied for subsequent animal studies. No further washing will be needed due to high affinity of iodide ions to GNRs.

Injectable doses for animal studies were prepared by mixing 0.5 mL of [^{125}I] sodium iodide with desired activity and 0.1 mL of GNRs (10^{12} rods/mL) for 5 minutes, and then centrifuging at 5000 rpm for 15 minutes. The supernatant was decanted and pellets were re-dispersed in 0.1 mL of fresh sterile filtered deionized water.

Total time (min)	Radioactivity in pellets (% from total, n = 12)	Aggregation (%)
5	60±6.1	0
10	74.4±3.3	0
15	90.0±3.1	0
30	99.4±0.6	33.3

Table 5.1: Summary of centrifugation for various periods

5.3.2 Stability of GNRs in blood circulation

The stability of injected GNRs within body is a key issue for successful targeting of GNRs because they must be able to circulate in the blood long enough to find their targets.[132] However, the RES of the body filters nanoparticles from blood circulation based on their size and surface characteristics.[76,117] Rapid clearance of nanoparticles from blood limits their targeting capabilities. Polyethylene glycol (PEG) has well-established "stealth" properties that can shield nanoparticles from fouling by serum proteins (opsonization) and reduce their rate of clearance by the RES.[117,131] The beneficiary effects of PEGylation on the clearance time of injected nanoparticles have been demonstrated.[132,140] Therefore, we synthesized three different kinds of GNRs, normal bare GNR, PEGylated GNR with PEG 5,000 mol. wt. and PEG 20,000 mol. wt., and examined their stabilities in blood circulation.

To determine the circulating time of gold nanorods, we assayed blood samples from rats using γ-scintigraphy. The time-activity curves are shown in Fig. 5.2, and indicate significant differences between bare GNRs and PEGylated GNRs. Injected bare GNRs were cleared out from blood circulation within 10 minutes, while greater than 50% of PEG coated GNRs remained in the blood after 4 hours. This is in good agreement with previous studies which have shown that a surface brush layer of PEG reduces the adsorption of blood RES factors to the particle surface hence decreasing the rate of particle clearance.[76,141] We have also found that it is irrelevant whether

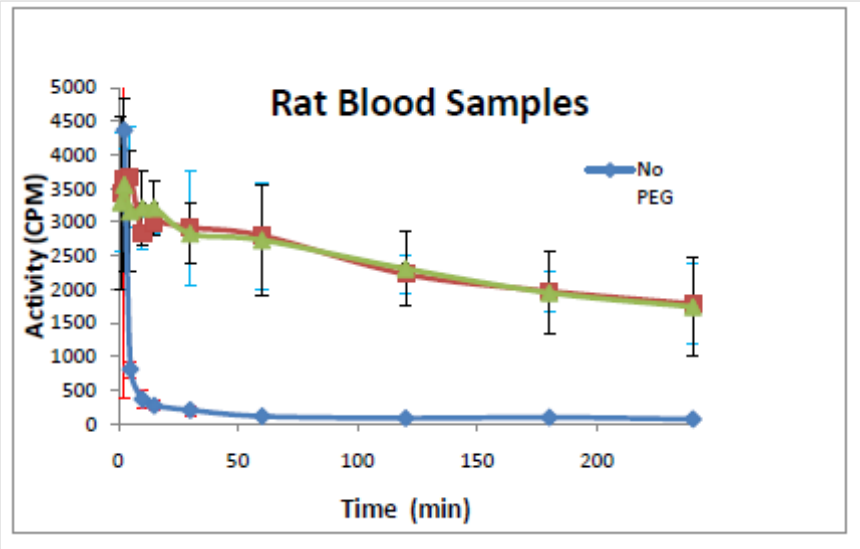

Figure 5.2: Blood time-activity curves

5,000 or 20,000 molecular weight is used.

The blood assay method described above is easy and reliable, providing initial information of novel gold nanorods in biosystems. The γ-scintigraphy is highly sensitive. Only a low dose of radioactivity has to be administrated and a small amount of blood sample needs to be drawn for measurement. This simple assay would be the first step for screening any newly designed target-specific GNRs.

5.3.3 Long-term biodistribution using γ-imaging

The next experiment evaluated the relatively long-term biodistribution in rat for up to 6 days using γ-imaging. The same group of animals used for blood assays were imaged at set times between blood sampling. Each image was acquired in 5-minute on an anesthetized rat placed in anterior position over the parallel-hole collimator of a Gamma Imager. Radioactivity was then quantified by drawing regions of interest (ROI). For each animal, ROIs were drawn around the liver/spleen and heart/lung and were saved to be re-used systematically for longitudinal follow-up. Figure 5.3 shows typical rat gamma images.

The linearity and precision of gamma detection were determined by scanning a

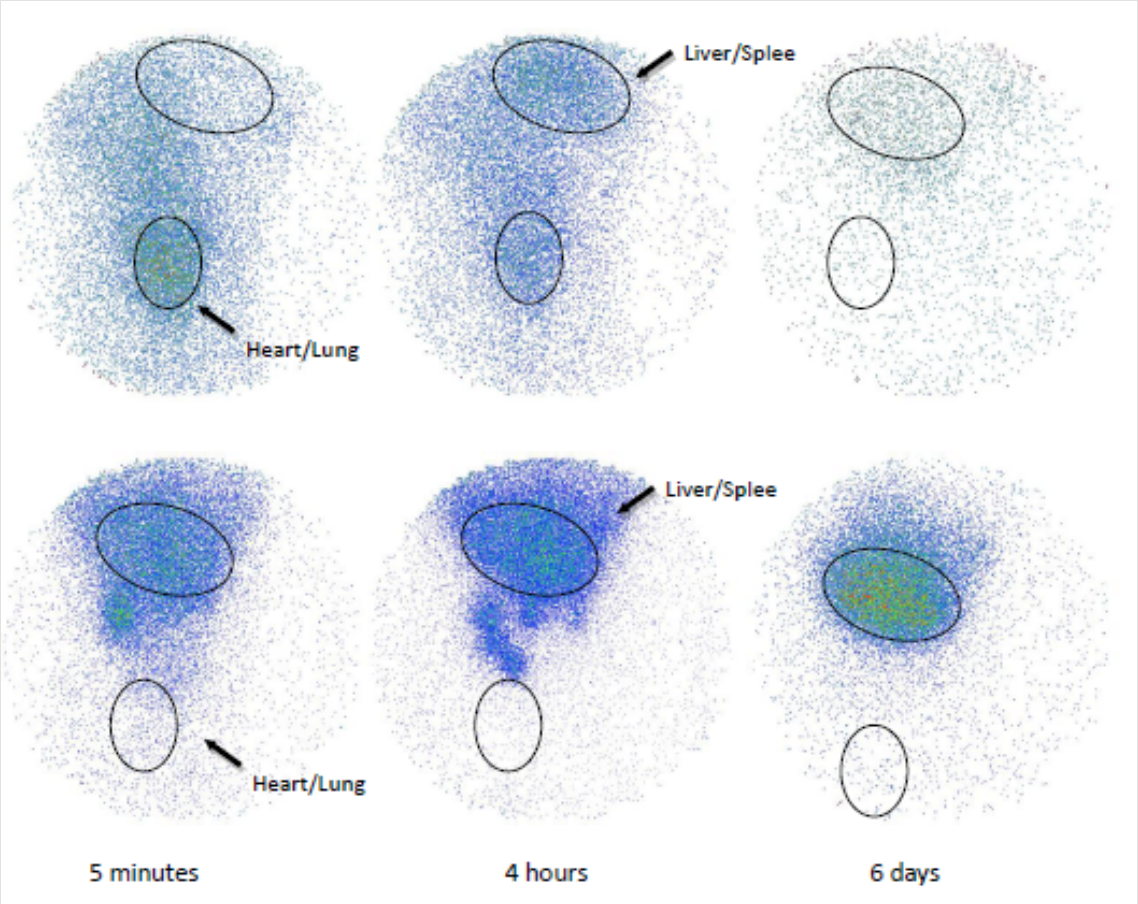

Figure 5.3: Gamma images at different post-injection time. The upper three images are from a rat injected with PEGylated GNRs. The lower three images are from a rat injected with bare GNRs.

series of standards with known radioactivities. The standards were prepared by serial dilution of a ^{125}I-GNRs injection sample. Each standard was imaged for 5-minute acquisition 8 times in various positions over the parallel-hole collimator. Radioactivity was then quantified by drawing regions of interest around the standard. Figure 5.4 shows good correlation between radioactivities counted by a Capintec well and radioactivities measured by scintigraphic acquisition of the Gamma Imager. The coefficient of determination (R2) value was greater than 0.99, indicating accurate and reliable measurement. The exact position of the sample on the camera head was shown to be irrelevant. Radioactivities in liver/spleen and heart/lung determined by the Gamma Imager were converted to injection dose based on this standard curve.

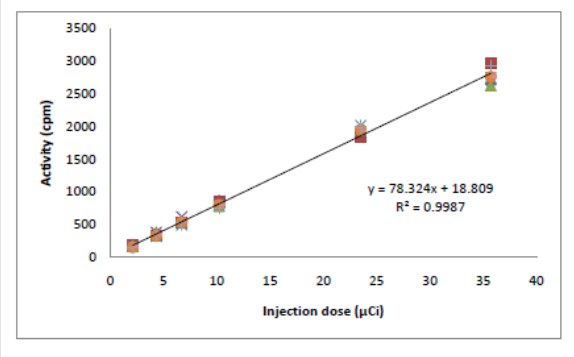

Figure 5.4: ^{125}I-GNRs standard curve

The uptakes of liver/spleen and heart/lung were then normalized to % of the injected dose for each animal. Results are shown in Fig. 5.5. Uncoated bare gold nanorods were found accumulated quickly in the liver and spleen area within 5 minutes. It should be noted that, for bare GNRs, radioactivity was retained in the liver and spleen for days. In contrast, PEG coated gold nanorods remained in the blood pool for much longer period, but the long term accumulation was minimal in liver and spleen area.

The liver/spleen and heart/lung areas were chosen as regions of interest because GNR particles accumulate in the liver and spleen when they are removed from blood; while they can be seen in the heart and lung when they are still freely circulating in the blood. Figure 5.5 shows the significant differences of uptakes between bare GNRs and PEGylated GNRs, and more importantly, the distinct metabolism pattern. The bare gold nanorods were retained in the liver and spleen for days. This indicates that bare metal particles are broken down and cleared from the body with difficulty. In contrast, PEG coated gold nanorods remained in the blood pool for much longer period, but the long term accumulation was minimal in liver and spleen area. The observed efficient metabolism clearance pattern provides evidence that PEGylated GNRs have low cytotoxicity and are more biocompatible within the body. They are hence ideal candidates for target-specific duel agents for diagnostics and selective photothermal therapy. The trends described here need to be tested in more detail with

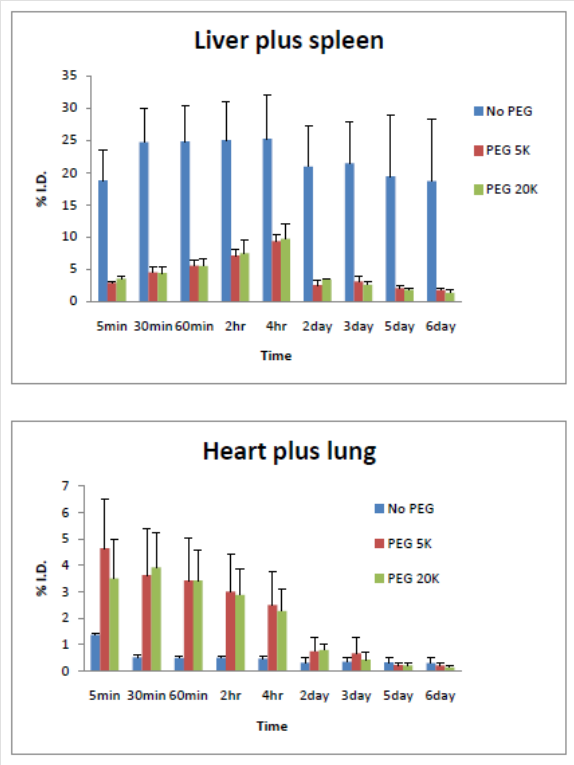

Figure 5.5: Activities in liver/spleen and heart/lung vs. time

a wider range of gold nanorods and will be reported in due course. This methodology provides a highly efficient tool for monitoring in vivo behaviors of virtually any gold nanocolloids.

In addition, we have successfully utilized GNRs to enhance the contrast in photoacoustic tomography (PAT).[37] We expect that radioisotope labeled GNRs can lead to the development of dual-modality imaging with the combination of nuclear imaging, like SPECT or PET, and PAI. Furthermore, it is hopeful that radiolabeled GNRs will become an efficient therapy agent with the combination of the power of radiation therapy and photothermal therapy.

5.4 Conclusions

We have optimized the radiolabeling procedures, facilitating reproducible and reliable production of injectable doses for animal studies. This simple setup can

be further developed to deliver injectable dose for clinical application. GNRs were successfully visualized by Iodine-125 tag allowing highly sensitive detection. The blood assay method described here is easy and reliable, providing initial information of novel gold nanorods in biosystems. Longitudinal biodistribution studies have been performed repeatedly in the same animal, therefore decreasing sources of inter-individual variations and also being beneficial in terms of animal cost and ethical practice. Comparing with the previously reported methods, the methodology developed here provide a highly efficient and universal protocol for monitoring in vivo behaviors of gold nanoparticles, GNRs, and other noble metal nanocolloids.

The preliminary animal results are very promising. PEGylated GNRs are ideal candidates for target-specific duel agents for diagnostics and selective photothermal therapy. With this powerful tool in hand, more work can be done to advance GNR technology to a level for clinical use in regards to clearance, safety, efficacy of deliverance and targeting. Encouraged by the preliminary study reported here, further investigations of GNRs with various sizes, shapes, and different conjugates are investigation. Radiolabeled gold nanorods hold promise to enable the development of multifunctional nanomedical platforms for simultaneous targeting, imaging, and therapy administration.

CHAPTER VI

Targeted Gold Nanoparticles Enable Molecular CT Imaging of Cancer

6.1 Introduction

Imaging plays a critical role in overall cancer management: in diagnostics, staging, radiation planning, and evaluation of treatment efficiency. Standard clinical imaging modalities such as computed tomography (CT), magnetic resonance imaging (MRI), and ultrasound can be categorized as structural imaging modalities; they are able to identify anatomical patterns and to provide basic information regarding tumor location, size, and spread based on endogenous contrast. However, these imaging modalities are not efficient in detecting tumors and metastases that are smaller than 0.5 cm and they can barely distinguish between benign and cancerous tumors.[142]

Molecular imaging is an emerging field that integrates molecular biology with *in vivo* imaging in order to gain information regarding biological processes and to identify diseases based on molecular markers, which usually appear before the clinical presentation of the disease. Currently, positron emission tomography and single photon emission tomography are the main molecular imaging modalities in clinical use, however, they provide only functional information regarding molecular processes and metabolites, which is indirect and nonspecific to distinct cells or diseases.[143,144]

Recently, various types of targeted nanoprobes have been developed for optical and MRI molecular imaging such as superparamagnetic nanoparticles;[145–148] quantum dots,[149–151] and gold nanoparticles as cancer optical imaging probes.[152–154] CT is one of the most useful diagnostic tools in hospitals today in terms of availability, efficiency, and cost. Currently, CT is not a molecular imaging modality since relevant targeted and molecularly specific contrast agents have not yet been developed. Present CT contrast agents are predominantly based on iodine containing molecules, which are effective in absorbing X-rays; however, they are nonspecifically targeted because they cannot be conjugated to most biological components or cancer markers and they allow only very short imaging times due to rapid clearance by the kidneys.

Figure 6.1: First ever medical X-ray image (1895) taken by Roentgen. "Hand with Ring" print of Wilhelm Roentgen's first medical X-ray, taken on 22 December 1895. It dramatically showed the bones of her fingers; however the real size of her finger's soft tissue could be garnered from the clearly visible gold ring on her finger. Likewise, below we show that ringing the tumor cells with gold nanoparticles makes it effectively more visible to CT. Note that the size of the ring maps the width of the finger's soft tissue. Radiology Centennial, Inc. copyrighted in 1993.

Gold induces a strong X-ray attenuation, as was first demonstrated, inadvertently, by Wilhelm Roentgen, in the first X-ray human image (Fig. 6.1). Gold nanoparticles have, in addition, unique physical, chemical, and biological properties, which make them an ideal candidate for CT contrast agents. The ability of CT to distinguish between different tissues is based on the fact that different tissues provide different

degrees of X-ray attenuation, where the attenuation coefficient is determined by the atomic number and electron density of the tissue; the higher the atomic number and electron density, the higher the attenuation coefficient. The atomic number and electron density of gold (79 and 19.32 g/cm^3, respectively) are much higher than those of thecurrently used iodine (53 and 4.9 g/cm^3). Note that for CT imaging the total amount of gold per unit volume (voxel) is the only important parameter regardless of the shape of the particles. In addition, gold nanoparticles provide a high degree of flexibility in terms of functional groups for coating and targeting and have also proved to be nontoxic and biocompatible *in vivo*.[155,156]

Recent progress toward nanotechnology based CT imaging has been made by Hainfeld *et al*;[157] they demonstrated the feasibility of gold nanoparticles to induce *in vivo* vascular contrast enhancement in CT imaging, however the gold particles were not targeted as they were not conjugated to specific biomarkers. More recently, hybrid nanoparticles such as antibiofouling polymer-coated gold nanoparticles,[158,159] gadolinium-coated gold nanoparticles,[160] PEG-coated nanoparticles,[161] and polymer-coated Bi_2S_3 nanoparticles[162] have been developed as vascular CT contrast agents. In this study, we describe a new platform for *in vivo* CT molecular imaging based on new class of immuno-targeted gold nanoprobes that selectively and sensitively target tumor specific antigens. These gold nanoprobes form a concentrated assembly on the cancer cells, yielding a distinguishable X-ray attenuation, which is not typical for nondecorated cells or tissue. This transforms the targeted cancer into highly distinct and easy to diagnose features.

While a CT molecular imaging agent would potentially have broad applicability for many cancer types, for this research we have chosen to work with head and neck cancer, which is the fifth most common cancer worldwide.[163] Squamous cell carcinoma (SCC) represents more than 90% of all head and neck cancers. Many SCC of the head and neck present as advanced tumors for which the true extent is difficult

to determine from present CT and physical examination. Cure rates for oral cancers have declined in recent years,[164] and better diagnostic tools are needed for accurate staging and discovery of tumor extent. Previously it has been demonstrated that SCC is characterized by significant overexpression of the A9 antigen,[165] which is also called the $\alpha 6\beta 4$ integrin,[166] and that there is a strong correlation between the A9 expression level and metastatic behavior.[167] It has also been demonstrated that the UM-A9 antibody can home onto SCC tumors *in vivo*.[168] An additional reason for choosing head and neck cancer was because one of its major diagnostic challenges today is a reliable detection of involved lymph nodes because their status is one of the most important prognosis predictors and is also critical for appropriate treatment. However, assessment of lymph nodes based on structural imaging features is limited in sensitivity and specificity and fails to distinguish between non-neoplastic and malignant processes. These limitations lead to the routine performance of prophylactic procedures such as extensive neck dissection and radiation and, on the other hand, a lack of treatment for undiagnosed small metastases, which is the first cause of the reappearance of cancer. Hence, the development of more sensitive *in vivo* imaging techniques is of major importance and could substantially improve head and neck cancer diagnosis, treatment, and potential cure.

In these experiments, we synthesized GNRs and conjugated them with UM-A9 antibodies, which home specifically to SCC head and neck cancer.[168] We examined their feasibility to effectively induce contrast enhancement in CT imaging, as a specific and sensitive targeted probe in head and neck cancer. Note that for CT imaging the total amount of gold per unit volume (voxel) is the only important parameter, regardless the shape of the particles. GNRs are more advantageous in comparison with spherical nanoparticles because they offer a complementary method of detection for some cancers based on their IR adsorption.[154,169] Most importantly, in comparison with other techniques utilizing optical properties of GNRs, CT scans are not limited

by the depth of cancer in the tissue.

6.2 Experimental section

6.2.1 GNRs synthesis and conjugation

GNRs were synthesized using the seed mediated growth method.[57] The mean length was 45 nm and the mean diameter was 15 nm with gold concentration of 2.5 mg/mL. Antibody conjugation: The bioconjugation of the GNRs to the UM-A9 antibody was achieved according to the method described by Kim et al.[38] Briefly, a layer of biocompatible[36,37,170] PAA was adsorbed onto the surface of GNRs followed by addition of EDC/NHS. PAA-coated nanorods were dispersed in 1 mL of PBS (pH 6.0) buffer, followed by 100 µL EDC and 100 µL of 0.2 M NHS mixture to provide active sites on GNRs that undergo amidation reaction with the antibodies. The amount of antibody added is 20 µg per 1.96 mg of molecular gold. The mixture was stored overnight in refrigerator at 4 ℃, followed by centrifugation and redispersion in ultrapure water to remove unbound antibody in the solution.

Cell culture: UM-SCC-1 and UM-SCC-5 human head and neck cancer cell lines and the negative control samples of fibrosarcoma (UM-FS-1) and melanoma (UM-Mel-1), which are known not to express the A9 antigen, were cultured in DMEM media supplemented with 10% fetal bovine serum, 1 mM sodium pyruvate, 100 units/mL penicillin, 100 µg/mL streptomycin sulfate, and 292 µg/mL L-glutamine (all from InVitrogen, Carlsbad CA).

Cells-GNRs binding: One milliliter of cell suspension (10^6 cells/mL) was mixed with 1 mL of antibody-coated GNRs solution (2.5 mg/mL) and allowed to interact for 90 min at room temperature. Then, the solution was 3 times centrifuged at 1000 rpm for 5 min to wash out unbound antibody from the GNRs-antibody complexes; after each centrifugation step, the mixture was redispersed in PBS solution (1 mL

total volume).

6.2.2 CT scan experiment

All scans were performed using clinical CT at 80 kVp (GE Lightspeed QX/I; General Electric, Waukesha, WI). The suspensions, in cuvettes, were scanned using a shaped Styrofoam assembly to hold the samples in place. Two SCC human head and neck cancer cell lines (10^6 cells/mL) were used; oral cancer UM-SCC-1 and larynx cancer UM-SCC-5. Both cancerous cell lines were shown before to have a significant overexpression of the A9 antigen.[165] CT imaging was performed on the SCC cells, which were targeted with the UM-A9 antibody-coated GNRs. The following negative control experiments were performed: (A) CT imaging of the same head and neck cancer cells (UM-SCC-1 and UM-SCC-5) in a suspension, without the addition of nanoparticles, (B) CT imaging of the same head and neck cancer cells that were targeted with GNRs that were coated with antibodies that do not match with the SCC cells (KHRI-3), and (C) CT imaging of noncancerous cells (normal fibroblast cells) and of other types of cancer cells (melanoma) that were targeted with the UM-A9 antibodies-coated GNRs. CT imaging of a solution of bare GNRs (suspended in water, without any cells) provides the positive control.

6.3 Results

6.3.1 CT scan

The attenuation values (HU) that were obtained from the CT imaging are shown in Fig. 6.2. As shown in Fig. 6.2, the change in the attenuation coefficient (with respect to water) of the SCC cancer cells that were targeted by the A9 antibody-coated GNRs is over 5 times higher than that of the nontargeted SCC cancer cells (32 and 28 HU vs 168 and 172 HU, respectively). This demonstrates that the GNRs were attached to the

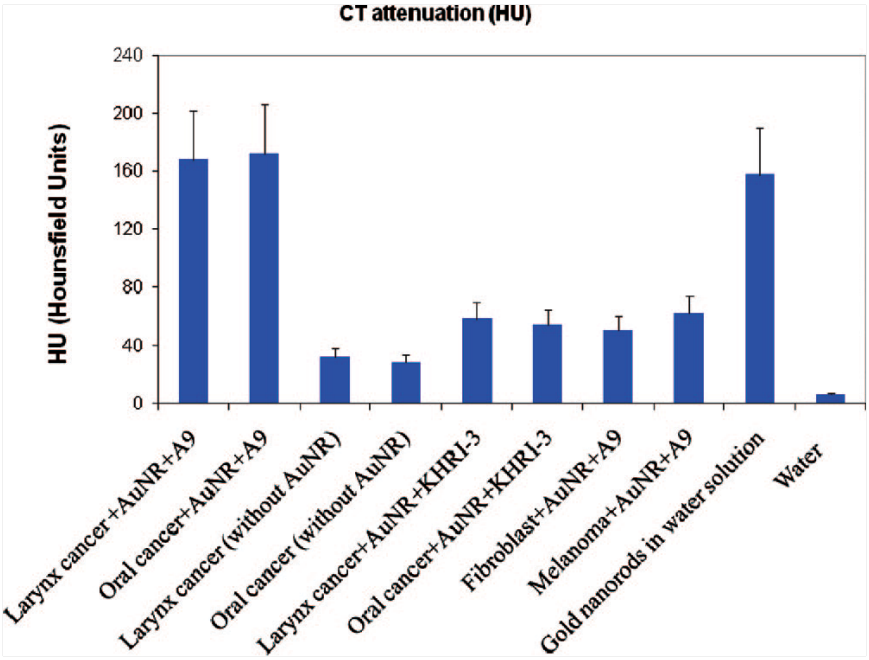

Figure 6.2: CT attenuation (HU) of SCC head and neck cancer cells and positive and negative control samples. Bar graph with standard deviation of 3 samples: larynx and oral cancer cells that were targeted with A9 antibody-coated GNRs, larynx and oral cancer cells without GNRs, larynx and oral cancer cells targeted with nanorods that are coated with nonmatching antibodies (KHRI-3); normal fibroblast and melanoma cells targeted with A9 antibodies, bare GNRs in water solution (2.5 mg/mL), and water

cancer cells with high density, yielding a distinguishable CT attenuation number that is higher than that for typical soft tissue (typical attenuation values for solid tissue are in the range of 0-50 HU), thus making the targeted cells detectable in sufficient concentration. The attenuation values observed for the negative control samples that were targeted with GNRs (larynx and oral cancer cells targeted with nanorods that are coated with nonmatching antibodies and normal fibroblast and melanoma cells targeted with A9 antibodies) revealed relatively low nonspecific binding (58, 54, 50, 62 HU, respectively) and demonstrate that head and neck tumors may show a likely enhancement of 3-4 times the local contrast of nontargeted tissue *in vivo*. Such a specificity and local enhancement is consistent with a previous study investigating the potential use of UM-A9 as a radiolabeled imaging agent for human squamous

carcinoma tumors *in vivo*.[168] The attenuation value observed for the positive control sample, the bare GNRs, is 158 HU; this high number was expected because the sample contained a high concentration of gold (2.5 mg/mL).

In these experiments, we tested 1 mL samples that contained 10^6 SCC cancer cells. Assuming the size of one SCC cancer cell is approximately 10 µm, there may be sufficient differential signal from tumors as small as 1 mm^3 to provide detectable contrast, nearly at the limit of resolution for clinical CT scanning. Another important parameter that should be noted is the high differential contrasts that have been obtained in the above experiments. The signal (HU obtained from the targeted SCC) is significantly higher than the background value (defined as the HU obtained from the control experiments). The enhancement of local signal increases local CT attenuation above the normal values for soft tissue, thus providing encouraging initial indications that sufficient specificity can be obtained in *in vivo* experiments.

6.3.2 Light scattering images of targeted and nontargeted SCC head and neck cancer cells

SCC head and neck cancer cells that were targeted with UM-A9 antibody-coated GNRs and SCC that were incubated with nonmatching antibodies (R-KHRI-3) coated GNRs were placed on a slide for dark field microscope imaging.

Figure 6.3 shows, for the scattering images, clearly distinguishable differences between the specifically and selectively targeted SCC cells and those that were exposed to nonmatching coated GNRs. The SCC cancer cells (oral and larynx cancer) that were targeted with the nonmatching antibody-coated GNRs yielded only a small amount of scattered light, resulting from the nonspecific binding. Yet, these images clearly illustrate that only the correctly conjugated nanoparticles bind specifically, with high concentrations, to the surfaces of the SCC cells.

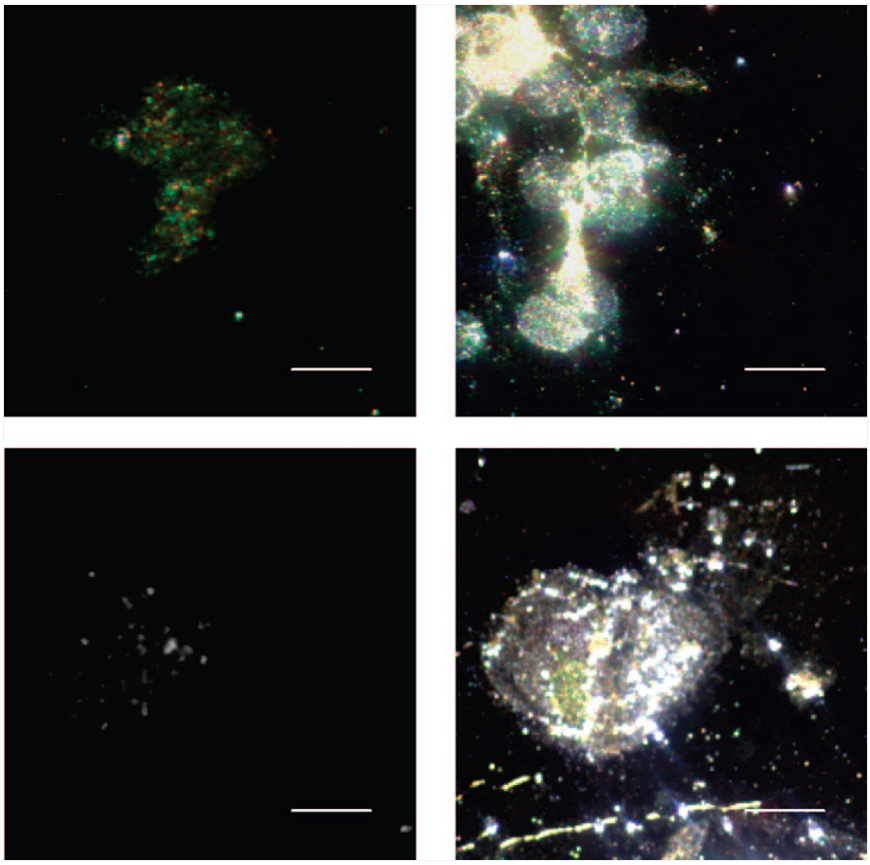

Figure 6.3: Dark field microscope images of SCC head and neck cancer cells. Dark field microscope images of SCC head and neck cancer cells (oral cancer upper images, larynx cancer lower images) after incubation with nonmatching antibody-coated GNRs (left) vs matching UM-A9 antibody-coated GNRs (right). Scale bar: 10 µm

6.4 Conclusions

In conclusion, these proof of principle experiments demonstrated that we may be able to identify, through CT scans, the existence of SCC cancer cells; the concentrated assembly of gold nanoparticles that form exclusively on the targeted cancer cells yield a strong selective X-ray attenuation that is distinct from the attenuation obtained by identical but untargeted cancer cells or by normal cells.

We expect that the CT molecular imaging technique will revolutionize modern head and neck cancer diagnosis and staging, by allowing reliable and sensitive detection of lymph nodes and other metastasis, which are not available today. This might also prevent or minimize the now routinely performed neck dissection, which

is associated with considerable morbidity. The importance of such a technique is further reinforced because of the vast availability and the extensive use of CT in clinics today and will provide the ability to perform simultaneously macroscopic (CT) and microscopic (molecular based CT) imaging.

CHAPTER VII

Optical Emission and Energy Transfer in Nanoparticle-Nanorod Assemblies: Potential Energy Pump System for Negative Refractive Index Materials

7.1 Introduction

One of the most fascinating types of metamaterials that is actively researched is negative refractive index materials (NIMs). Early theoretical discussions by Veselago showed that an isotropic media with both negative permittivity, ϵ, and permeability, μ, will exhibit a negative refractive index along with several other interesting properties.[171] However, such materials remained a curiosity for decades because no naturally occurring materials exhibit simultaneous negative μ and ϵ over a common frequency range. Recent theoretical demonstration by Pendry showed that an ideal Veselago lens (flat slab in vacuum with $\epsilon = \mu = -1$) can not only focus light from an object to form an image but can do so with subwavelength resolution ($\Delta x < \lambda$).[1] Such lens has been termed the "perfect lens" and has created a new surge of interest in the development of artificial metamaterials with negative refractive index. NIMs have also been suggested as novel materials for usage in biological and security imaging,

biomolecular fingerprinting, remote sensing, cloaking devices, and guidance in zero visibility weather condition.[43–45]

The two most common approaches to fabricate NIMs take advantage of photonic crystals[3,172–174] or plasmonic periodic metal dielectric nanostructures.[175–177] NIM photonic crystals are based on the excitation of photonic band gaps with negative slope to support negative phase velocity in the medium and are limited in their performance due to scattering from surface imperfections. In metal-dielectric nanostructures the displacement currents near plasmonic resonances are used to produce both negative permittivity and negative permeability. One-dimensional gold and silver nanostructures in various arrangements have been theoretically and experimentally shown to have negative refractive index.[178] Importantly, operating near plasmonic resonances in metallic NIMs makes their response strongly dispersive and lossy;[179] thus, restraining the restoration of near field modes which are required for sub wavelength resolution in the image. One way to reduce losses in metallic systems is to operate away from the resonances,[180] however this would weaken the diamagnetic response of the medium potentially causing it to no longer have the effective negative permeability. The other way is to compensate the losses by providing a gain medium. The conventional way of adding a gain medium is by sandwiching a 2D layer between the NIM, but this requires an impedance match at the interface to avoid losses by reflection.[181,182] Submerging entire metallic nanoparticles (NPs) in dye molecules which act as a gain medium has also been suggested.[183] Dyes, however, have limited lifetime and bleach rapidly. As well, there are inherent optical limitations related to Stocks shift in organic dyes that limit their applicability to NIMs.

In this paper, we demonstrate that semiconductor NPs assembled with metallic nanorods or similar optical media can be used as a potential gain material for NIMs. Both experiments and corresponding theoretical calculations describing coupled optical oscillators in semiconductor (exciton) and metal (plasmon) clearly in-

dicate that the excitonic energy of NPs can be funneled into the plasmon of gold nanorods (GNRs). The actual manufacturing of such assemblies was accomplished using fairly universal the biotin-streptavidin (B-SA) bioconjugation strategy between CdTe NPs and GNRs. Strong quenching of CdTe NPs, which indicates energy transfer into GNRs was observed. Given sufficient intensity and coherence of the excitation of NPs away from the resonance band of GNRs, the energy transfer can compensate for losses in NIMs.

7.2 Experimental section

7.2.1 Materials

Hexadecyltrimethylammonium bromide (CTAB), silver nitrate, ascorbic acid, sodium borohydride, gold(III) chloride, L-cystine, thioglycolic acid (TGA) were purchased from Aldrich and used without further purification. Deionized water (Barnstead, E-pure system) with 18 MΩ was used in preparation of solutions. Streptavidin (SA) and D-biotin (B) were obtained from Aldrich. 1-Ethyl-3-(3-dimethylamino propyl) carbodiimide hydrochloride (EDC) and N-hydroxy-sulfosuccinimide (NHS) were purchased from Aldrich and Merck for bioconjugation, respectively.

7.2.2 Synthesis and bioconjugation of GNRs

GNRs of average aspect ratio 3.7 (length 48 nm and width 13 nm) were synthesized by a method described elsewhere.[57,92] Synthesized GNRs were purified by removing excess salts and stabilizer using centrifugation and redispersion into deionized water. The GNRs are dispersed in deionized water to achieve a concentration of 10^{-8} M of GNRs in the solution. CdTe NPs were synthesized with L-cystine stabilizer (average diameter 3 nm) for bioconjugated assembly as reported previously.[184] The particles were used as synthesized (average concentration 10^{-5} M of NPs) without any fur-

ther purification. Binding of biotin to L-cystine NPs is performed as described in literature.[185,186]

A layer of poly(acrylic acid) (PAA) is adsorbed onto the surface of GNRs by adding 1.5 mL of 1 mg/mL PAA solution to 1 mL of the stock gold GNRs solution. The mixture is stirred for 3 h followed by two cycles of centrifugation and redispersion to remove excess PAA in the solution.[187] The layer of PAA provides the -COOH functional group required for the conjugation. The PAA coated nanorods are dispersed in 1 mL of PBS 6.0 buffer solution followed by the addition of 100 µL of 0.2 M EDC and 100 µL of 0.2 M NHS. After 20 min, the reaction mixture is added with 20 µL of SA. The EDC/NHS mixture forms an active ester intermediate with the gold nanorods which undergoes amidation reaction with the -NH_2 group in SA to yield the conjugate. The reaction mixture is stored in refrigerator at 4 ℃ overnight following centrifugation and redispersion in buffer to remove the unconjugated SA. Photoluminescence spectrums were recorded using Fluoromax-3 spectrofluorometer (Jobin Yvon/SPEX Horiba, NJ). UV-visible absorption spectra were recorded using Agilent (former HP) UV-vis spectrophotometer.

7.3 Results

We used two approaches for the preparation of NP-GNR complexes: electrostatic and bioconjugation. In the electrostatic method of assembly we used positively charged GNRs and negatively charged NPs bearing thioglycolic acid as a stabilizer. Electrostatically bound structures were appealing to us because they can potentially reduce the gap between the nanoscale building blocks, and thus, increase the resonance amplitude in exciton-plasmon hybrid states. However, NP-GNR superstructures assembled electrostatically displayed approximately an order of magnitude lower efficiency of NP→GNR energy transfer than protein-bound systems potentially due to the dynamic nature of the electrostatic assemblies where NPs migrate in and out

of the range of plasmon-exciton interactions with GNRs. Thus, all the data presented here refer to the system with B-SA linker.

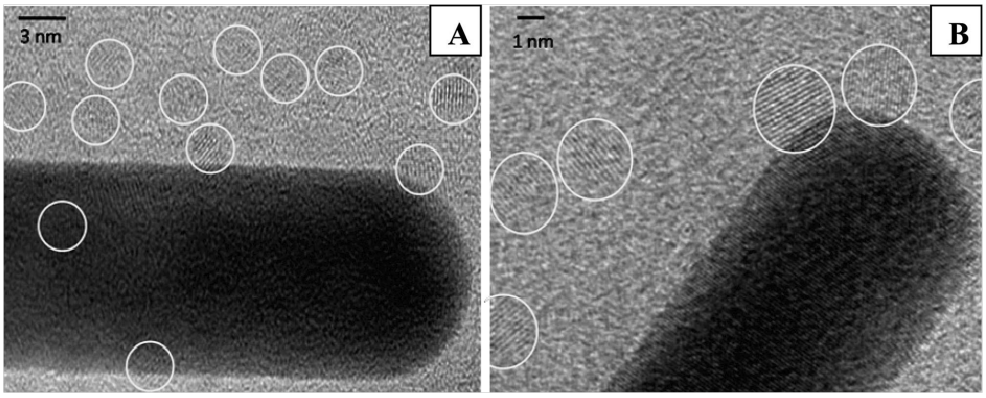

Figure 7.1: (A) TEM image of bioconjugated assembly, ratio of NPs/GNR=25. (B) HRTEM image showing the lattice structure of NP bioconjugated to GNR

Structure of the NP-GNR Complexes. Bioconjugates of NPs and other nanocolloids bearing biological groups with strong mutual affinity allow one to create sophisticated NP assemblies.[60,188–191] As such, due to specific binding between SA and B, mixing of GNR-SA and NP-B leads to superstructures with NPs attached to the surface of GNRs (Fig. 7.1). The same conclusion can be reached from the study of electrokinetic ζ potentials of the nanocolloids (Table 7.1). As the ratio of the number of CdTe NPs per GNR (i.e., NP/GNR ratio) increases, the zeta potential gradually changes from positive to negative. The change of sign of zeta potential is reflective of the increase of the density of NPs attached to GNRs. The separation between the NP and GNR in bioconjugated structures is due to the presence of bilayers of CTAB, streptavidin-biotin and L-cystine.

Assuming the simple case of attachment via SA-B connection, the distance between the center of the NPs and the surface of the GNR is estimated to be Δ_{BA}=6.5 nm. Distances between the two components are established from TEM images at higher magnification to give an average NP-GNR distance of 5 nm which coincides with the estimates above quite well. In case of formation of additional shells of NPs attracted by, for instance, strong van der Waals forces to the initial coating of NPs,

NP/GNR ratio	lifetime (ns)	ζ potential (mV)
∞	26.66	-31.1
1000	13	-0.90
500	7.07	6.6
333	4.33	4.7
250	3	5.2
125	2	4.1
50	0.62(extrapolatedvalue)	5.4
25	0.31(extrapolatedvalue)	5.3
0	NA	30.6

Table 7.1: Lifetime Values and Electrokinetic (ζ) Potentials for Bioconjugated Assembly at Various NP/GNR Ratios

the distance between the GNR surface will increase by a few more nanometers depending on the NP layer geometry. The signs of NP clustering around GNRs beyond a simple monolayer can be seen in Fig. 7.1(A). This process can be treated as if the self-assembly of the first layer catalyzes the adherence of the NP in the second layer. At the same time it is self-limited due to strong repulsion of similarly charged NPs in the shells. The same processes are observed during the layer-by-layer assembly of NPs.

One also needs to remember that the NP-GNR bioconjugates are 3D structures, which creates difficulties in traditional TEM imaging. Bringing both components of the assemblies, NPs and GNRs, in focus at the same time, becomes more difficult than for much simpler 2D arrangements of GNRs or NPs separately. However, we were able to do it when both building blocks are properly positioned. In Fig. 7.1(B) one can clearly distinguish the lattice planes corresponding to CdTe particles and GNR. The CdTe NPs show a lattice spacing of 0.249 nm which corresponds to the (111) plane of CdTe nanocrystal with a literature value of lattice spacing of 0.229 nm.[192] The distribution of the NPs along the length of the rod is fairly random; no preference is given to the ends of the rods or their sides (Fig. 7.1). We also see evidence (Fig. 7.1(A)) of NP clustering around the GNRs and formation of double

shells. The primary bond between the first layer of NPs and GNRs is of SA-B nature, while subsequently the particles in the secondary shell are attached by nonspecific interactions.

7.3.1 Optical properties

Based on previous studies,[60,185,188–191,193] NP-GNR distances observed in Fig. 7.1 are expected to result in strong interactions between exciton and plasmon states in the semiconductor and metallic particles, respectively. This interaction can result in both luminescence enhancement[194,195] as well as quenching.[60,196] NP superstructures studied previously included the assemblies of CdTe NWs and GNPs.[193] The general geometrical configuration of the superstructure in the present case is similar to those reported before[60,185,190,193] with the exception that the symmetries CdTe and Au components are switched, i.e. the axial rod like structures here are made from metal as opposed to the semiconductor wires in the previous publication. This results in radical differences in optical behavior of the superstructures. In the present case, when the rods are made from gold, we observe very strong quenching of CdTe excitons that are attributed to energy transfer from NP to GNRs via a resonance state (Fig. 7.2(A-C)), as opposed to the enhancement of exciton emission due to coupled field stimulation from Au NPs observed previously.

The quenching of NP luminescence in bioconjugated superstructures progresses over a period of 30 min, following the typical B-SA binding kinetics.[60,73,197] Upon addition of NP-B into a solution containing GNR-SA we find that initially there is a fast drop in PL intensity within first 3 min, followed by much slower gradual decrease over the next 27 min. The early stages of the kinetic curve should cover mostly the formation of B-SA links, while the later stages should mostly describe attachment via nonspecific interactions. At the moment these two parts are difficult to separate. However, more detailed investigation of this process will make it possible

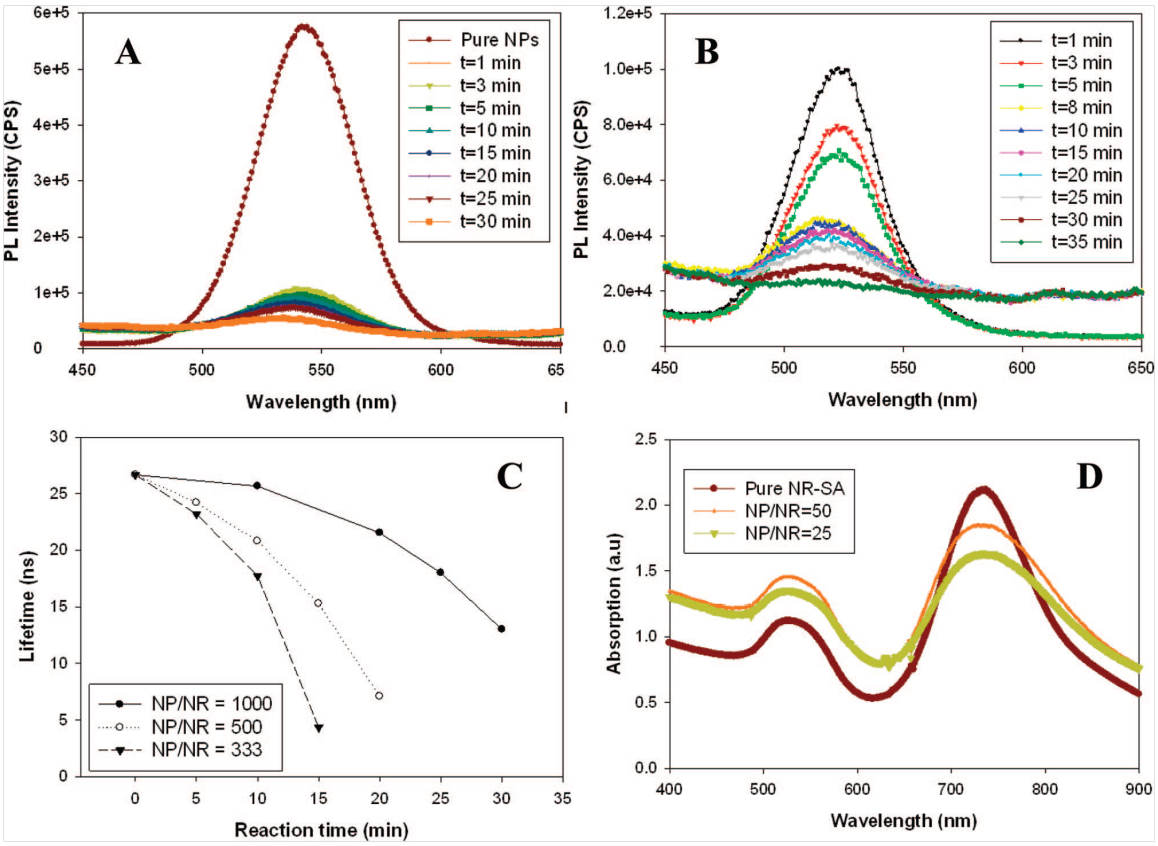

Figure 7.2: (A) Consecutive fluorescent spectra for the formation of NP-GNR bioconjugated assembly with NP/GNR=125. (B) Consecutive fluorescent spectra for the formation of NP-GNR bioconjugated assembly with NP/GNR=12.5. (C) Change of lifetime values of NPs during the period of formation of bioconjugated NP-GNR assembly. (D) UV-vis of GNR-SA before and after assembly with NP-B. Excitation wavelength 350 nm.

when such data might be necessary. Note there is an increase of the background signal in the "wings" of the luminescence peak for the later stages of assembly, which is attributed to stronger scattering of the assembled structures. When one compares quenching data from the two systems with NP/GNR ratios different by 10 times (Figure 7.2(A)&(B)), the kinetics becomes about 10 times slower in accordance with general theory of reaction rates ∂[NP-GNR]/∂t=k[NP][GNR], giving the degree of quenching over a period of ca. 30 min for NP/GNR=12.5 approximately equal to that observed for 3 min for NP/GNR=125. Importantly, for both NP/GNR ratios the final state is almost complete quenching of NP luminescence (Fig. 7.2(A)&(B)).

The CdTe fluorescence peak spanning 480 to 580 nm overlaps with the transverse plasmon resonance (480-550 nm) of the GNR. The coupling of excitons from NP with plasmons is believed to be able to funnel energy into the GNR.[198] NPs are excited in the near UV wavelengths and would interact minimally with the incident light (optical wavelengths) and avoid any undesirable effects on the effective properties of the material at optical wavelengths. The presence of CdTe NPs around GNR, however, slightly dampen and broaden the plasmonic response of the GNRs (Fig. 7.2(D)), which may or may not be significant for actual NIM structures. Slight broadening of the plasmon resonance may actually be advantageous for NIMs as it provides a broader wavelength range over which the NIM response could be realized. The broadening of the plasmon peak and the presence of semiconductor NPs at the interface may actually serve as a convenient control parameter to vary the degree of resonance/ off-resonance excitation for NIM structures.

The conjugated NPs remain stable in solution and show same plasmon absorption as in Figure 7.2(D) for 7 days. The plasmonic absorption starts decreasing after 7 days and the solution shows aggregated particles after 12 days which may be caused due to protein denaturation. Since the NP-GNR assembly is robust one can use these structures by depositing them onto substrates or thin films. The stability period is also sufficient to carry out any polymerization reaction necessary to permanently fix the assemblies.

The effect of superstructure formation on the lifetime of CdTe excitons was also measured (Table 7.1 and Fig. 7.2(C)). For small NP/GNR ratios this is fairly difficult to do due to low overall luminescence and strong quenching, but for ratios in the range of 333-1000 the lifetime, τ, can be measured during the assembly process. As expected, formation of the NP-GNR superstructure results in significant decrease of the emission lifetime because of the NP$\rightarrow$GNR energy transfer processes. Larger NP/GNR ratios results in slower kinetics which indicates the change in general kinetic

description of the process for high concentrations of NPs and potential saturation processes when the amount of NPs is sufficient to occupy all available surfaces on GNRs. Simple geometrical calculations for closely packed structure of CdTe NPs on GNRs with the dimensions used here correspond to 70 NPs per one GNR, however, apparently greater number of NPs may cluster around the GNRs in 2 or more shells due to the nonspecific clustering of NPs. We observed complete quenching as NP/GNR ratio reached 25. So, we were unable to experimentally measure the lifetime of the assembly at this ratio because of the low luminescence intensity. We use the Stern-Volmer quenching kinetics (Eq. 7.1) to fit the experimental data from higher NP/NR ratios and obtain theoretical value of lifetime at lower NP/GNR where experimental data is difficult to measure.

$$\frac{\tau^0}{\tau} = 1 + \mathbf{K}_a \tau^0 [Q] \tag{7.1}$$

Where $\mathbf{K}_a$, is the bimolecular reaction rate constant for the elementary reaction of

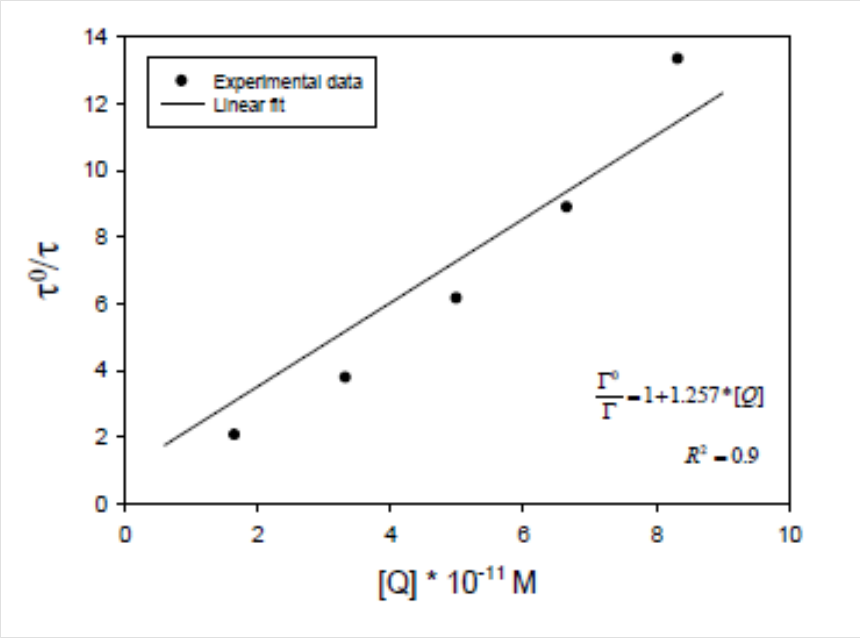

Figure 7.3: Stern-Volmer fit of the experimental data given in Table 7.1

the excited state with the particular quencher Q, τ^0 is the lifetime in the absence of a quencher (i.e., absence of NR in our case) and τ is the lifetime in presence of quencher

concentration [Q]. Concentration of the quencher [Q] i.e., GNR is calculated by their final concentration in the solution. Linear fit of the experimental data gives us the value of $\mathbf{K}_a\tau^0$=1.257 mol^{-1}. The value of lifetime obtained for NP/GNR=50 and 25 corresponding to [Q] = 33.33×10^{-11} M and 66.66×10^{-11} M gives us a lifetime value of 0.621 ns and 0.314 ns respectively.

The lifetime data shown in Table 7.1, the data in Fig. 7.2(C), and the quantum yield for the NPs equal to Y=0.115 were used as input parameters in the theoretical calculations described below as well as in the ensuing discussion.

7.3.2 Blue shift of emission peak

Interestingly, we observe a noticeable blue shift in the emission spectra of NPs by ∼5 nm as formation of the bioconjugated assembly proceeds (Fig. 7.2(A),(B) and 7.4).

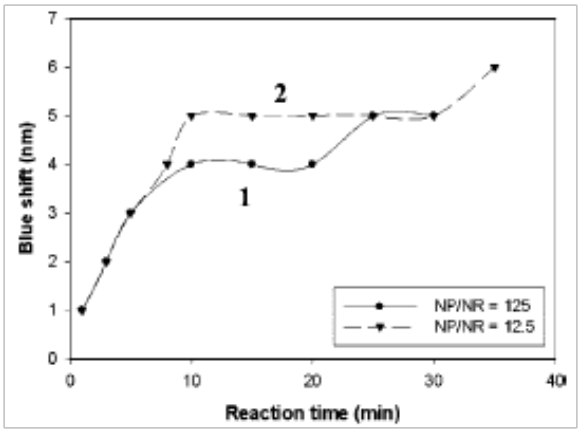

Figure 7.4: Position of the maximum of emission peak during the period of formation of two bioconjugated assemblies with GNR=125 (1) and GNR=12.5 (2)

This shift may come from the reduction of Coulomb binding energy, $E_{Coulomb}$, of an exciton in CdTe NPs due to an enhanced dielectric screening in a bioconjugated assembly according to the standard equation of quantum confinement effect in

semiconductor NPs:

$$E_{exc} = E_{bulk} + h^2/2m^*d^2 - E_{Coulomb} \tag{7.2}$$

where E_{exc} is the energy of emitted exciton considered to be equal to band gap energy in the quantum confined state, E_{bulk}, is the band gap in the bulk state, h is Plank constant, m^* is the reduced mass of electron and hole $m^* = 1/m_e + 1/m_h$, d is the diameter of the NP. Upon assembly, the Coulomb interaction between an electron and hole inside CdTe NP becomes slightly lower since the average dielectric constant of the surrounding increases due to the presence of the neighboring metal and semiconductor NPs.

7.4 Theoretical model and Discussion

Quenching of emission and shortening of exciton lifetime in the NP-GNR superstructures can be explained using a model based on the exciton-plasmon resonance (Fig. 7.5) taking place when emission peak of excitons in NPs and adsorption peak of the plasmons in GNRs display a spectral overlap. In a NP-GNR complex, oscillators corresponding to excitons in NPs and plasmons in GNRs couple via simple Coulomb forces. Since NP-GNR complexes are in liquid, they are randomly oriented with respect to the incident electric field, $\vec{E_0}$ (Fig. 7.5(A)). To obtain analytical estimates, we will treat GNRs as infinite cylinders. In addition, we will consider here the near field regime where $\lambda >> d$ is the wavelength of light and NP-GNR distance, respectively. Considering the data in Figure 1, this assumption is certainly valid.The electric field in the vicinity of infinite metal cylinder is described by the potential: $\phi = -\vec{E_0}\vec{r} + (\epsilon_{Au} - \epsilon_0)/(\epsilon_{Au} + \epsilon_0) \bullet (a^2{}_{GNR}/4\rho^2)\vec{E_0}\vec{r}$, where a_{GNR} is the GNR diameter, ρ is the distance to the GNR axis, and ϵ_{Au} and ϵ_0 are the dielectric constants of metal and matrix, respectively. The light absorption rate in a CdTe NP

is proportional to $\left\langle \vec{E} \bullet \vec{E}^{*} \right\rangle_{\Omega}$, where $\vec{E}$ is the electric field in the vicinity of GNR and Ω is the solid angle. Averaging over Ω is introduced to take into account random orientations of GNRs with respect to the incident light. After simple algebra, we obtain $\left\langle \vec{\mathbf{E}} \bullet \vec{\mathbf{E}}^{*} \right\rangle_{\Omega} = E_0^2[1 + (2/3)\gamma\gamma^{*}(a_{GNR}^4/d^4)]$, where $\gamma = (\epsilon_{Au} - \epsilon_0)/(\epsilon_{Au} + \epsilon_0)$. The intensity of emission from a CdTe NP is derived from the rate equations published previously for molecular systems with fluorescent dyes.[194]Note that molecular and nanoscale superstructures have an important difference. An excitation in molecular systems is described by one exciton with a given direction of dipole moment. A spherical NP has three optically active excitons with optical dipoles along x, y, and z axes. Due to fast spin relaxation at room temperature, we can assume that optical excitation creates almost equal populations of excitons with different orientation in respect to a NP axis. Therefore, to calculate the resultant emission of a NP, we have to take into account all three orientations of excitons. At room temperature, the emission intensity of NP is given by[188,199]

$$\mathbf{I}_{emiss}(\lambda_1, \lambda_{emiss}) = \frac{\mathbf{P}(\lambda_{emiss}) \bullet \gamma_{rad}^0 \bullet \mathbf{P}(\lambda_1) \bullet \mathbf{I}_{abs}^0}{\mathbf{P}(\lambda_{emiss}) \bullet \gamma_{rad}^0 + \gamma_{non-rad}^0 + \gamma_{transfer}(\lambda_{emiss})} \tag{7.3}$$

where λ_1 and λ_{emiss} are the wavelengths of exciting light and emitted photons, respectively, $\mathbf{P}(\lambda) = \left\langle \vec{\mathbf{E}} \bullet \vec{\mathbf{E}}^{*} \right\rangle_{\Omega} / E_0^2$ is the averaged field enhancement factor for a NP in the vicinity of a GNR, and I_{abs}^0 and γ_{rad}^0 are the light absorption and radiative rates of a CdTe NP in the absence of a GNR. The denominator in Eq. 7.3 represents the total recombination rate of an exciton $\gamma_{rec} = P(\lambda_{emiss}) \bullet \gamma_{rad}^0 + \gamma_{non-rad}^0 + \gamma_{transfer}(\lambda_{emiss})$, where $\gamma_{non-rad}^0$ is the nonradiative recombination rate and $\gamma_{transfer}(\omega_{emiss})$ is the rate of NP→GNR energy transfer. The parameter $\mathbf{P}(\lambda_{emiss}) \bullet \gamma_{rad}^0$ in Eq. 7.3 describes the radiative emission rate of an exciton in a NP in the presence of a GNR. Similarly, $\mathbf{P}(\lambda_1) \bullet \mathbf{I}_{abs}^0$ is a metal-modified absorption rate of a CdTe NP. In particular, we can see that the factor $\mathbf{P}(\lambda)$ is an important parameter of the system. From Eq. 7.3, we obtain the ratio between emission intensities before and after conjugation:

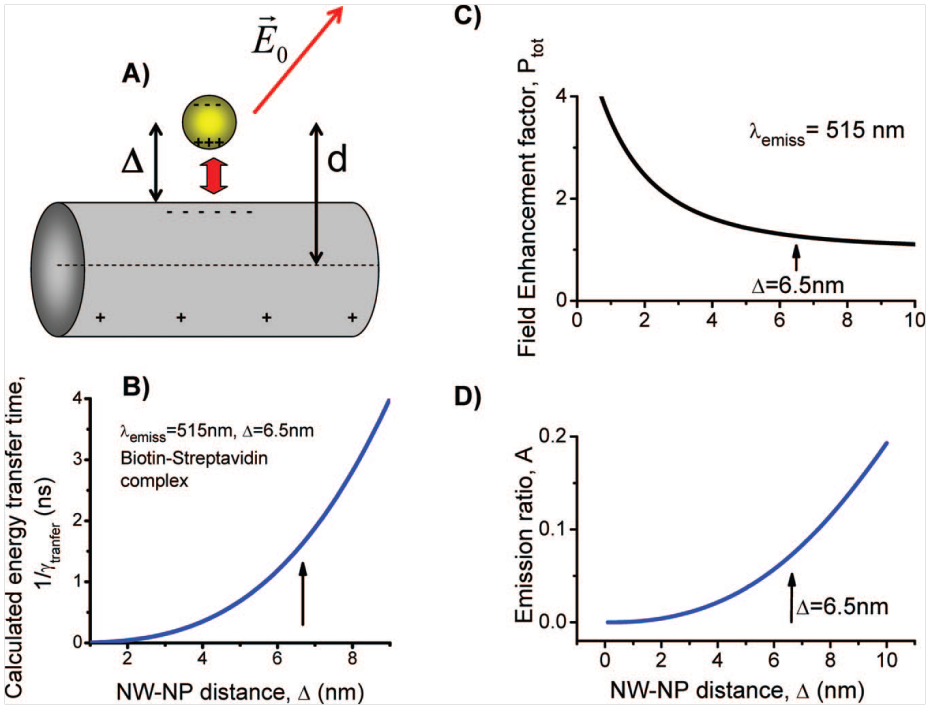

Figure 7.5: (A) Model of NP-GNR system. Red arrow shows the process of energy transfer. (B) Calculated energy rate as a function of NP-GNR separation. (C and D) Theoretical results for enhancement factor and emission ratio

$$\mathbf{A}(d,\lambda_1,\lambda_{emiss}) = \frac{\mathbf{I}_{emiss,complex}}{\mathbf{I}_{emiss,0}} = \mathbf{P}_{tot}\frac{\gamma_{rad,av,0}+\gamma_{non-rad}}{\gamma_{transfer}+\gamma_{rad,av,0}\mathbf{P}(\lambda_{emiss})+\gamma_{non-rad}} \quad (7.4)$$

where $\mathbf{P}_{tot} = \mathbf{P}(\lambda_1)\mathbf{P}(\lambda_{emiss})$ is the resultant field enhancement factor for the emission; $\gamma_{non-rad} = (1-\mathbf{Y}) \bullet \gamma^0_{rec}$ and $\gamma^0_{rad} = \mathbf{Y} \bullet \gamma^0_{rec}$ where $\mathbf{Y}$ is the quantum yield and $\gamma^0_{rec} = 1/\tau^0_{rec}$ is the recombination rate of excitons in NPs in the absence of metal GNRs. The transfer rate $\gamma_{transfer}$ describes the process of Forster like energy transfer NP→GNR (Fig. 7.5(A)). This process comes from the Coulomb interaction between a photoexcited exciton in a CdTe-NP and plasmons in a GNR. A convenient formalism to calculate the rate $\gamma_{transfer}$ is based on the response function.[188,199]

Here we give a result for small NP-GNR distances, $\Delta < a_{GNR}$:

$$\gamma_{transfer} = \frac{(ed_{exc})^2}{\hbar\epsilon_{eff}^2}\frac{\epsilon_0}{3\Delta^3}Im\frac{(\epsilon_m - \epsilon_0)}{\epsilon_m + \epsilon_0}) \tag{7.5}$$

where $\epsilon_{eff} = (2\epsilon_0 + \epsilon_{NP})/3$ and d_{exc} is the exciton dipole moment and ϵ_{NP} is the dielectric constant of CdTe. We note that the transfer rate in Eq. 7.5 was calculated as an averaged transfer rate of three types of excitons in a CdTe NP: $\gamma_{transfer} = (\gamma_{tr,x} + \gamma_{tr,y} + \gamma_{tr,z})/3$, where $\gamma_{tr,i}$ is the transfer rate for the exciton with a dipole moment in the i-direction.

For small distances ($\Delta < R_{GNR}$), $\gamma_{transfer} \propto 1/\Delta^3$.[200] For large distances ($\Delta > R_{GNR}$), Eq. 7.5 is no longer applicable and $\gamma_{transfer} \propto 1/\Delta^5$.[190] Equation 7.5 was used to obtain estimates for bioconjugated complexes with the following parameters: a_{GNR}=15 nm, $R_{NP} \approx 1.5nm$ (CdTe NP radius) and Δ=6.5 nm (length of SA-B linker length). Exciton emission from our CdTe NPs has the following characteristics: τ_{rad}^0=26.6 ns and Y≈0.115 (see above). The dielectric constant of the metal was taken from the tables[201] and the other dielectric parameters were chosen as $\epsilon_{NP} = \epsilon_{CdTe} = 7.2$ and $\epsilon_0 = \epsilon_{water} = 1.8$. The exciton dipole moment was estimated from the radiative time: d_{exec}= 0.53 Å. Results of calculations are summarized in Fig. 7.5(B-D). For the assembly, we obtain an energy transfer time of $1/\gamma_{transfer} \approx 1.51ns$. The calculated lifetime of an exciton in the NP-GNR superstructure is $1/\gamma_{rec}^0 = 1/(\mathbf{P}\cdot\gamma_{rad} + \gamma_{non-rad}^0 + \gamma_{transfer}) \approx 1.4ns$. Regarding the emission intensity, the following emission ratio was calculated: A≈0.07. Overall, our theoretical data are in qualitative agreement with the experimental data (Table 7.1 and Fig. 7.2(A-B)). Importantly, our theory reveals microscopic mechanisms of energy exchange in the NP-GNR assemblies. We note that the calculated exciton lifetime in the bioassembly ($1/\gamma_{rec} \approx 1.6ns$) is close to the observed lifetime (2 ns) for NP/GNR=125 from Table 7.1. However, the extrapolated lifetimes for very small NP-GNR ratios are essentially

shorter (Table 7.1). We see two possible ways to explain it: (1) extrapolation using the Stern-Volmer kinetics is not always reliable or (2) there may be an additional mechanism of quenching of emission in the system.

Considering the trend of experimental points in Stern-Volmer plot (Figure S1, Supporting Information), which indicates that the for small NP/GNR ratios the lifetime becomes shorter, we believe that additional mechanisms of energy transfer/quenching are possible which can be represented by charge transfer reactions. Finally, the physical reasons why the lifetime strongly depends on the NP/GNR ratio should also be discussed. In experiments (Table 7.1), we clearly see this tendency: the lifetime becomes strongly reduced with decrease of the NP/GNR ratio. Physically, this can be explained in the following way: when NP/GNR$>$ 70, NPs cannot form a single shell around a GNR and arrange themselves in two or more layers. Moreover, even for relatively small NP/GNR ratio, not all NPs may form a single shell and be very close to the metal surface. Some of NPs may be on the top of other NPs (see Fig. 7.1). This means that the average NP-GNR distance is dependent on NP/GNR ratio and therefore, the NP-GNR transfer time becomes dependent on it too, becoming shorter when smaller number of NPs is present (Stern-Volmer fit, Fig. 7.3). One can also can notice that the blue shift in Fig. 7.4 is larger for NP/GNR=12.5; this behavior is consistent with the same distance dependence as was described above for lifetimes. For smaller NP/GNR ratio (12.5), the blue shift should be indeed larger since NPs are located on average closer to the metal surface and the metal screening effect is stronger. For the larger ratio (125$>$70), the blue shift should be smaller since the average NP-GNR distance is increased. We also should compare the experimental and theoretical emission ratios, A. For the assembled structures with NP/GNR=125, we see a nice overall correspondence of theory and experiment: $A_{theory} \approx 0.07$ and $A_{exper} \approx 0.08$. Finally we should note that the plasmon-induced field enhancement in our system is small, $P_{tot} \approx 1$. Therefore, the energy transfer process plays the main

role and leads to strong emission quenching as opposed to emission enhancement.

7.5 Conclusions

We have demonstrated NP-GNR superstructures which can act as potential energy transfer pumps and help reduce the absorptive metallic losses. Excitons created optically in NPs become converted into plasmons in metal GNRs via the Forster energy transfer mechanism and intermediate exciton-plasmon hybrid resonant state. In this way, the plasmon population inside the metal component can be sustained via off resonance light adsorption. The excitation wavelength of NPs can be far from the plasmon resonance wavelength of GNR, say in UV absorption bands of CdTe, such as 350 nm as we used in this work, hence the emission of NP would interfere minimally with the incident light at optical wavelengths unlike similar systems that can be created from dyes. Additionally, the energy transfer in NP systems is likely to be more efficient than in analogous dye-based structures due to better resonance conditions with plasmons in GNRs and fast spin relaxation to match the required one for a particular place on the GNRs. We see the need to reveal in greater detail the exciton-plasmon interactions in semiconductor-metal assemblies with GNRs and potential competing mechanisms of energy relaxation requiring single-particle spectroscopy and pump-probe techniques.

As a part of the concluding remarks, we also want to make two points about applications of such systems for NIMs. (1) The GNR from gold or other metal will likely to form the basic structure on the NIM metamaterials. Advanced methods of manufacturing, such as nanoscale lithography, selforganization of polymeric block structures, or layer-by-layer deposition, which can also produce layers of NP and GNR separated by a thin (1-2 nm) layer of polymer, are probably the most suitable approaches to their manufacturing. Regardless of the method, bioconjugation processes provides a universal method of attaching semiconductor NPs to the base metallic structure. (2)

NPs present a natural advantage over the dyes for NIM materials with gain because of much wider absorption spectrum which makes possible separation of pumping light from the spectral window where NIM response can be observed.

CHAPTER VIII

Field Induced Orientational Order of Gold Nanorods Dispersed in Organic Solvents

8.1 Introduction

GNRs are promising building blocks of negative index metamaterials due to their negative electric susceptibility at optical frequencies. There are two absorption peaks in the optical response, associated with plasmon resonances for polarizations parallel and perpendicular to the rod axis. Because the susceptibility at optical frequencies is strongly anisotropic, a key requirement for realizing bulk optical negative index materials is controlling orientational order. Low frequency electric fields may be expected to align GNRs, however, such alignment is not at all straightforward, since the susceptibility anisotropy at low frequencies far from resonance is small.

Previous work[202] showed the alignment of long (aspect ratio >10) GNRs in aqueous solvents, where only the transverse absorption peak was in the visible spectrum. Short (small aspect ratio) rods, where both plasmon resonances are in the visible, do not align well in such systems, at least in part due to the large dielectric constant of water at low frequencies. Organic solvents, with low dielectric constants overcome this obstacle. Another reason for using organics as the suspension medium is the improved stability against GNR aggregation. GNRs are solubilized in polar solvents by

ionic surfactants. These also stabilize the suspension; their dissociation is responsible for the electrostatic repulsion of particles. In such systems, the particles are in a secondary (local) energy minimum due to electrostatic interactions, and will eventually aggregate since the global energy minimum occurs when the particles are in contact. By contrast, metallic NPs can be solubilized in organic solvents by organic polymer surfactants which can be covalently bonded to the surface of the GNRs. Such a system is stabilized against aggregation by the entropic repulsion of the polymer chains, and the system remains in the global free energy minimum indefinitely.

We have developed a novel method for dispersing GNRs in non-aqueous solvents. This enables the production of NP suspensions which remain stable against aggregation indefinitely. The GNRs in these suspensions can be aligned by external electric fields even if their aspect ratio is small (<3) and both plasmon resonances are in the visible. Importantly, by controlling the aligning electric field, the alignment can be varied as a function of time unlike other alignment methods proposed for alignment of axial structures in organic matrixes.[203,204] GNRs synthesized by wet chemistry are limited to dispersion in water because the surfactant CTAB, essential for growth for rods, is soluble in water only. Transfer of GNRs from aqueous to organic solvents (phase transfer) has been achieved previously using water-immiscible ionic liquids but this method is limited in its efficiency of phase transfer.[205] The rods lose their plasmon peaks and appear to aggregate after transfer into the organic solvent. Gold, having high chemical affinity for thiol, seems to be the easiest choice for the replacement of surfactants but presents its own challenges due to large Van der Waals forces and the resulting agglomeration. Zubarev *et al* have used a slow and delicate process for replacing the surfactant CTAB with polystyrene.[206] Chen *et al* have reported phase transfer from aqueous solvents to toluene using a combination of mercaptosuccinic acid and tetraoctylammonium bromide.[207] We introduce here a very simple and generic new way of transferring GNRs from aqueous solutions into a wide variety of

organic solvents.

8.2 Experimental Section

8.2.1 Synthesis of GNRs

GNRs were synthesized using the method described in literature.[57] Briefly, the process involves reducing gold ions by a strong reducing agent ($NaBH_4$) which then form spherical NPs that act as a seed when added into a growth solution containing gold ions and the surfactant hexadecyltrimethyl ammonium bromide (CTAB). Typically, seed solutions are made by mixing CTAB solution (5.0 mL, 0.20 M) with HAuCl4 (5.0 mL of 0.0005 M) followed by the addition of ice-cold $NaBH_4$ (0.6 ml, 0.010 M) under vigorous stirring for 2 minutes. The growth solutions are made by adding $AgNO_3$ (0.6 ml, 0.004 M) to CTAB solutions (10 mL, 0.2 M) followed by addition of HAuCl4 (10 mL, 0.001M) and ascorbic acid (140 µL, 0.0788 M). To grow rods, 24 µL of seed solution is added to the prepared growth solution and kept in a water bath at 28 ℃ for 12 hours. The synthesized gold rods have bilayers of positively charged surfactants on the surface and are dispersed in water. Excess stabilizer in the solution is removed by centrifugation and redispersion of the rods in pure deionized water. The process is repeated two times and 20 mL of synthesized rods are concentrated into 1 mL of aqueous dispersion.

8.2.2 Phase transfer of GNRs into organic solvernts

To achieve dispersion in an organic solvent, we typically use a 5 mL glass vial in which 1 mL of concentrated aqueous rod solution is added to 1 mL of polystyrene thiol (55,000 mol. wt.) solution in tetrahydrofuran (THF) (25 mg/mL) and the mixture is vigorously shaken by hand for 1 minute. The reaction leads to instantaneous aggregation and the aggregates adhere to the glass wall, leaving behind colorless

water and THF mixture. The aggregates have no specific shape or size. The water and THF mixture is next decanted and the remaining moisture in the glass vial is removed by drying with a heat gun (100 ℃ for 3 minutes). The gold rods inside the aggregates have been grafted with polystyrene molecules and can be dispersed in any on a wide variety of organic solvents(see Fig. 8.2(B)). Typically 1 mL of toluene is added to the vial containing the aggregates and sonicated for 15 minutes to get a homogeneous dispersion.

8.2.3 Field induced alignment of GNRs in organic solvent

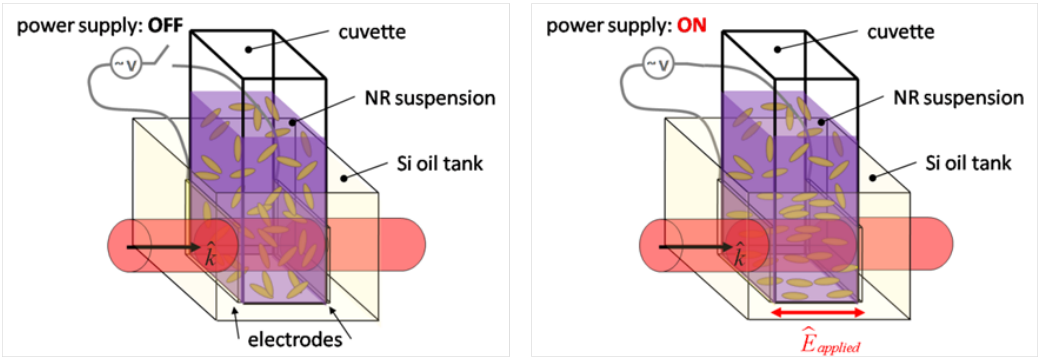

Figure 8.1: Experimental geometry for homeotropic alignment

The experimental setup is shown in Fig. 8.1. A 0.35 mL, 1 mm path length, cuvette containing the GNRs dispersed in toluene having 12.7×15.2 mm ITO coated glass electrodes glued to the outside surface of the cuvette rather than inside the cuvette to prevent dielectric breakdown of the solvent and any ion issues. The cuvette with electrodes is submersed into transformer oil (Clearco STO-50) to prevent ionization of the air. The GNR solution is filled well above the height of the electrodes. A 15kV, 60Hz neon transformer (Franceformer 15030P) with a Variac is used to apply an electric field on the GNR solution. The absorbance is measured with a spectrometer (Oceanoptics HR4000CG-UV-NIR with Mikropack DH-2000 light source). For the experiment we apply 15 kV across a 3 mm cuvette (1 mm path length), the maximum free space field is 5×10^6 [V/m]. By applying an electric field across the sample

we orient the GNRs in a homeotropic alignment.

8.3 Results

8.3.1 Phase transfer of GNRs into organic solvernts

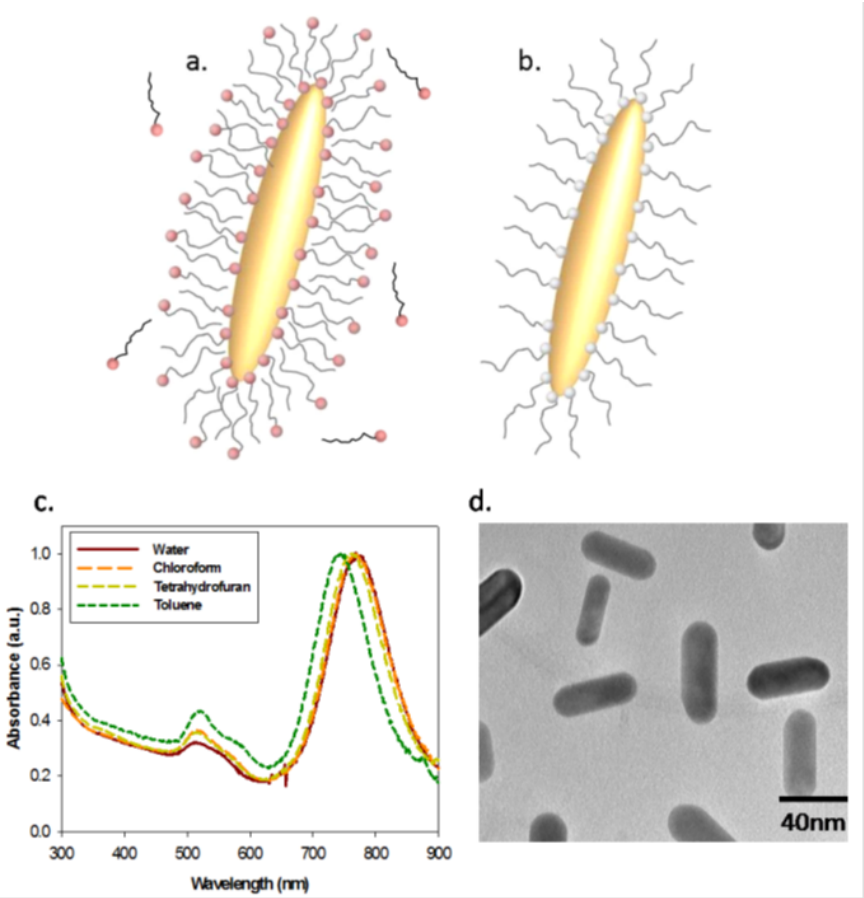

Figure 8.2: (A) Schematic of CTAB stabilized aqueous GNR. Red spheres indicate positively charged head group (B) Schematic of polystyrene stabilized organic GNR. White spheres indicate thiol head group. (C) UV-Vis absorption spectrum of GNRs dispersed in various solvents (D) TEM images of GNRs dispersed in toluene

The choice of THF as a solvent for polystyrene thiol is critical for the reaction because its solubility in water facilitates reaction between thiol molecules and the gold atoms on the surface of rods. The nature of CTAB binding on the gold surface is dynamic in nature, and the high affinity of sulfur groups for the gold causes immediate covalent bonding of gold and polystyrene thiol. As the reaction proceeds towards

completion, the rods change from hydrophilic to hydrophobic and become insoluble in the water and THF mixture which leads to their aggregation. Drying the aggregates helps remove traces of THF which may be left behind. The aggregates dissolve and redisperse into individual rods when introduced into an organic solvent. The intermediate step of aggregation of rods does not in any way affect the shape or size of the rods. The resulting dispersion shows both of the characteristic transverse and longitudinal plasmon peaks in the absorption spectrum, with the same intensity as in the aqueous solvent, but shifted due to change in the dielectric properties of the surrounding fluid.[207,208]

8.3.2 Field induced alignment of GNRs in organic solvent

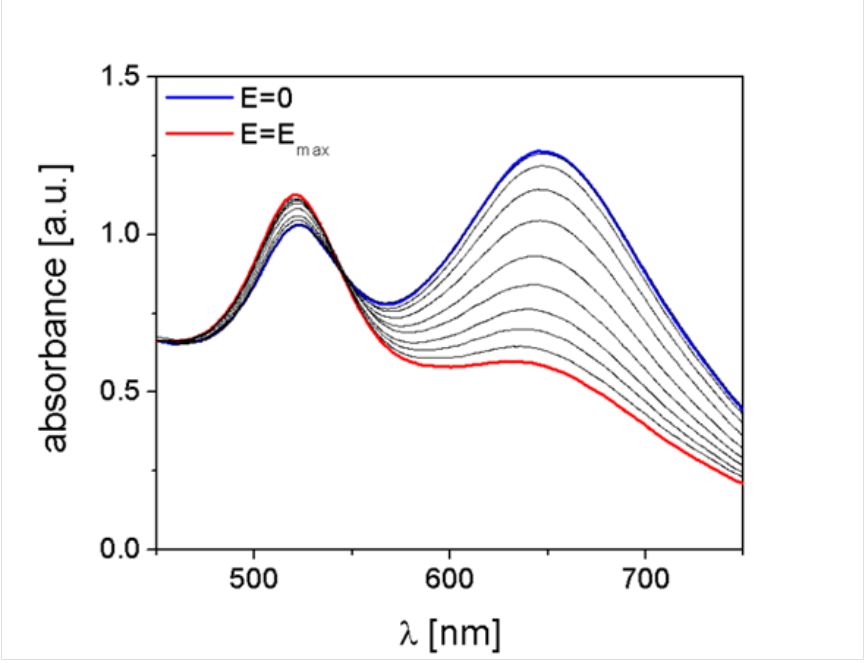

Figure 8.3: Experimental absorbance Vs. wavelength for changing applied electric field

Fig. 8.3 is an absorbance spectrum for GNRs in toluene. The sample size of the GNRs is approximately 40 nm × 15 nm and the volume fraction is, $\phi \approx 10^{-5}$. The transverse mode wavelength, $\lambda_{\parallel}$, is at 525 nm and the longitudinal wavelength, $\lambda_{\perp}$

is at 659 nm. As the external electric field is increased we see suppression of the longitudinal peak and a slight increase in the transverse peak as expected from the previous studies of aligned GNR composites.[209]

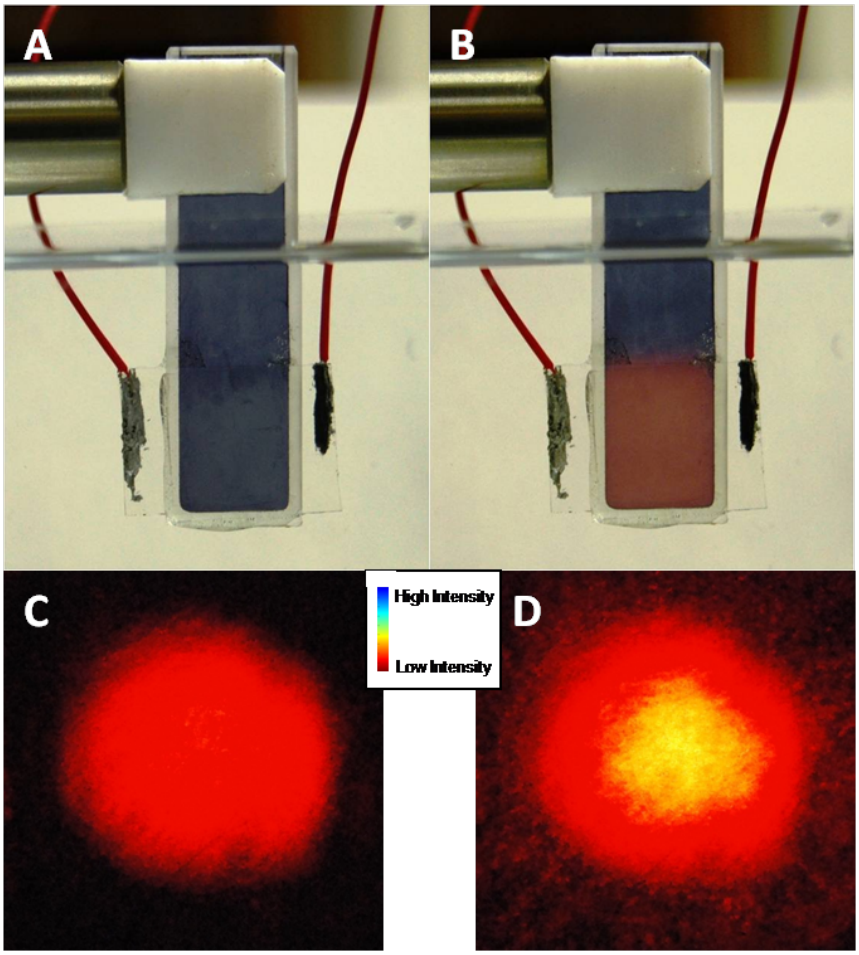

Figure 8.4: Color change with field turned off (A) and turned on (B). Intesity change with field turned off (C) and turned on (D)

A white light source (Mikropack DH-2000 light source) was shot through the sample. We observe a drastic change in the apparent transmissive color when the GNRs are oriented (Fig. 8.4 (A-B). The transmissive color appears to be blue in the isotropic phase. When the field is applied, the longitudinal peak is suppressed, and the transmissive color appears to be red. A Melles-Griot (25-LHP-925-249) 30 mW HeNe laser is shot through the sample. In Fig. 8.4 (C-D) when the field is applied and the longitudinal peak is suppressed and we see an increase in the transmitted

intensity.

8.4 Discussion

The anisotropic susceptibility of GNRs is reponsible for the alignment of these particles with an external electric field. The induced dipole moment of an inclusion with dielectric constant and whose shape is an ellipsoid of revolution in a dielectric host with dielectric constant, ε_1, is given by,

$$p_\alpha = V\varepsilon_0\chi_{\alpha\beta}E_\beta \tag{8.1}$$

where V is the volume, **E** is the applied field, and the susceptibility tensor, $\chi_{\alpha\beta}$, is,

$$\chi_{\alpha\beta} = \varepsilon_1 \begin{bmatrix} \frac{1}{N_\perp + \frac{\varepsilon_1}{\varepsilon_2 - \varepsilon_1}} & 0 & 0 \\ 0 & \frac{1}{N_\perp + \frac{\varepsilon_1}{\varepsilon_2 - \varepsilon_1}} & 0 \\ 0 & 0 & \frac{1}{N_\parallel + \frac{\varepsilon_1}{\varepsilon_2 - \varepsilon_1}} \end{bmatrix} \tag{8.2}$$

where $N_\parallel$ and $N_\perp$ are the depolarizing factors for fields parallel and perpendicular to the long axis of the ellipsoid.[210] The frequency dependence of the dielectric constant of Au may be approximated by the Drude model[211] where

$$\varepsilon_2 = 1 - \frac{\omega_p^2}{\omega^2 + i\beta\omega} \tag{8.3}$$

Here ω_p is the plasma and β is the collision frequency. The energy of the inclusion in the field is[212]

$$U = -\frac{1}{2}p_\alpha E_\alpha = -\frac{1}{2}V\varepsilon_0\chi_{\alpha\beta}E_\alpha E_\beta \tag{8.4}$$

If the frequency of the applied field **E** is 60 Hz, ε_2 is large and negative, and the

energy U, can be written as

$$U \simeq -\frac{1}{2} V \varepsilon_0 \varepsilon_1 E^2 \left(\frac{1}{N_\perp} - \left(\frac{1}{N_\parallel} - \frac{1}{N_\perp} \right) \cos^2(\theta) \right) \tag{8.5}$$

where θ is the angle between $\mathbf{E}$ and the long axis of the ellipsoid. Since $N_\parallel < N_\perp$ for prolate ellipsoids, the GNRs tend to align with the field. In equilibrium, the degree of alignment of the inclusions is given by the orientational order parameter

$$S = \left\langle \frac{1}{2} \left(3\cos^2(\theta) - 1 \right) \right\rangle = \frac{\int \frac{1}{2} \left(3\cos^2(\theta) - 1 \right) e^{-\frac{U}{kT}} \sin\theta d\theta}{\int e^{-\frac{U}{kT}} \sin\theta d\theta} \tag{8.6}$$

To achieve alignment, the energy U must the comparable to kT, and writing $-\frac{U}{kT} = const. + \left(\frac{E}{E_c} \right)^2 \cos^2(\theta)$ the field to align the particles must be comparable to

$$E_c = \sqrt{\frac{2kT}{V \varepsilon_0 \varepsilon_1 \left(\frac{1}{N_\perp} - \frac{1}{N_\parallel} \right)}} \tag{8.7}$$

If the length and width of a GNR are 40×15 nm and, assuming ellipsoidal shape, $N_\parallel = 0.125$ and $N_\perp = 0.438$, and since for toluene $\varepsilon_1 \simeq 2.2$, at $T = 300K$, Eq. 8.7 gives $E_c = 1.94 \times 10^6$ V/m. Thus a large field, on the order of 1 $V/\mu m$, is required to align the GNRs.

Two physical parameters must be taken into consideration regarding the externally applied electric field. The first is the magnitude of electric field that must be applied in order to get strong orientational alignment. The energy of the applied field must be greater than the thermal energy fighting to disorient the GNR, i.e. $\Delta \mathbf{E}^2 > kT$. We can estimate the field strength assuming where ε_0 is the permittivity of free space, V is the volume of a GNR, $\mathbf{E} \approx \sqrt{\frac{kT}{\varepsilon_0 V}} = \sqrt{\frac{10^{-21}}{10^{-11} \times 10^{-23}}}$. We must apply fields on the order of one million volts per meter before we can expect to see any kind of alignment. The second is the reduction in electric field strength from the depolarizing fields in the solvent. If we compare the relative electric field strength

between two linear dielectrics, water and toluene, the fields scale as, $E_2 = \frac{\varepsilon_1}{\varepsilon_2} E_1$. The dielectric constant of water (aqueous) is 80.4 whereas toluene (non-aqueous) only has a dielectric constant of 2.2. The large dielectric constant of water severally inhibits the ability to experimentally achieve strong alignment of short aspect ratio GNRs. The effective electric field in the suspension is reduced by a factor of 40 in water when compared with toluene. It is then imperative to use a non-aqueous solvent, such as toluene, for alignment in GNR suspensions.

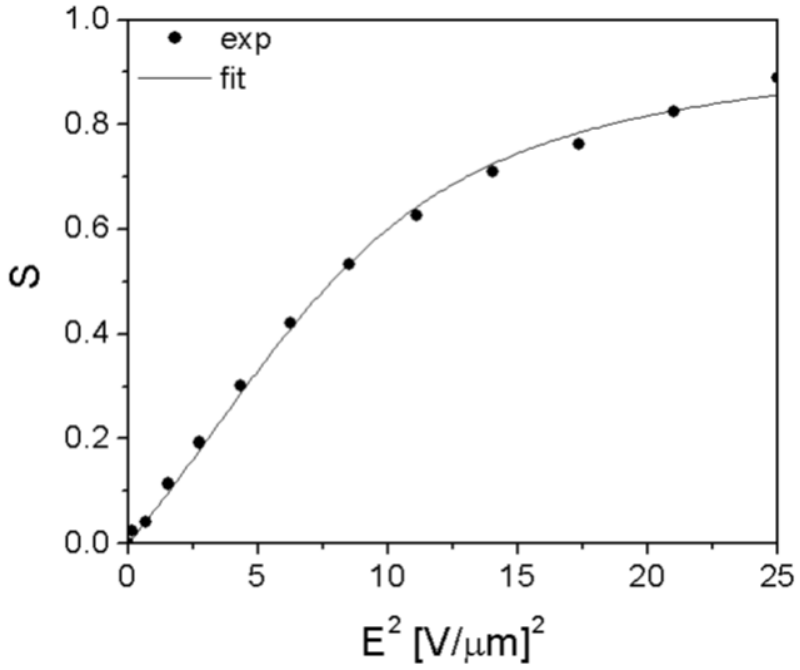

Figure 8.5: Order paramater S as function of electric field strength

The two principal plasmon resonances from the GNR susceptibility tensor give rise to two characteristic absorption peaks, the transverse mode wavelength, $\lambda_{\parallel}$ and longitudinal mode wavelength, $\lambda_{\perp}$, in the visible spectrum. We measure the absorbance, αx, of a suspension of GNRs in a non-aqueous solvent as a function of electric field strength ($\mathbf{E}^2$) with both plasmon resonances in the visible. The absorbance is linearly proportional to the GNRs orientation. If an electric field is applied parallel to $\vec{k}$, the GNRs align with the field, we observe a suppression of the longitudinal peak absorp-

tion as the field strength is increased (see Fig. 8.3). For the isotropic case, S=0, the absorbance is at a maximum and when the GNRs are completely aligned, S=1, the absorbance is at a minimum. Depending on the geometry of the external field we can suppress one of the absorption peaks while isolating the complementary absorption peak (see Fig. 8.3). We are able to achieve a high degree of alignment with an order parameter of S≈0.9 (see Fig. 8.5)

8.5 Conclusions

Alignment of non-aqueous GNRs in solution was achieved with a maximum order parameter of S≈0.9. A simple method for phase transfer of GNRs from aqueous to non-aqueous solvent was developed. We developed a method to characterize the orientational order of the system by measuring the absorbance versus externally applied electric field. Due to the high degree of orientational order we observed transmissive color and intensity changes in the GNR suspension.

CHAPTER IX

Real-Time Detection of Scrambled Prions on 3D-Supercrystals of Gold Nanorods

9.1 Introduction

Prions are hard-to-detect infectious agents that cause a number of fatal neurodegenerative diseases in mammalians such as bovine spongiform encephalopathy (BSE), scrapie of sheep, and Creutzfeldt-Jakob Disease (CJD) of humans,[213] and recently traced as well to other neurodegenerative syndromes as Alzheimer[214] and Parkinson.[214] Invariably, all of these diseases involve the modification of the endogenous and functional prion protein (PrP^{C}) into a non-functional but much more stable form (PrP^{SC}) giving rise to the so-called amyloid plaques in the brain and other nervous tissues.[215] Notably, and in contrast with common infectious agents carrying a nucleic acid genome, prions appear to encipher strain-specific properties in the tertiary structure of PrP^{SC}. The α-helix structure of the endogenous PrP^{C} is refolded into the β-sheet PrP^{SC} through a post-translational process mediated by the PrP^{SC} itself, acting as a template, thus generating a chain reaction that leads to neurodegeneration.[216] The high stability of this new β-sheet conformation of PrP^{SC} provides the miss-folded proteins with unprecedented biological, chemical and physical resistance toward for example proteases, nucleases, formaldehyde, UV light or temperature. All

these features render PrP^{SC} an extraordinary infectious agent as it can be transmitted by ingestion of contaminated food (PrP^{SC} resist conventional food sterilization procedures without denaturation), or through contact with contaminated biofluids such as saliva, urine or blood. On the other hand, because prions essentially are not exogenous agents but endogenous proteins refolded into a non-functional structure, they promote very weak or no immune responses. Thus, detection of its presence for contention in cattle or diagnosis in humans is very difficult even by state-of-the-art immunological methods such as FIA, RIA or ELISA.[217] Thus the confirmation of BSE, scrapie or CJD still relies on the post-mortem imaging analysis of the degenerated tissues of the suspected individuals. This usually results in late response implying risk of pandemic outbreak, with additional important economic consequences. Society therefore urges for the development of novel detection techniques capable of accurately detecting/diagnosing the presence of prions in the blood of infected but not clinically sick animals to avoid the dissemination of the disease. Recent studies show that the concentration of prions in infected presymptomatic individuals stays around 5 to 20 infective prion units per mL of blood (equivalent to the attomol regime) raising to more than 100 in the early stages of the disease.[218] This point is very important as infected individuals and their fluids, including blood for transfusions,[219,220] can transmit the disease during pre-symptomatic stages, which, together with the long latency of the syndrome (sometimes even years), makes prion detection critical to avoid outbreaks.[221]

From the several approaches that have been developed for the pre-symptomatic detection of prions in biofluids, only two, protein misfolding cyclic amplification (PCMA)[222] and immunological methods,[223] have offered any promising results. However, PCMA analogously to PCR, relies on the conversion of the endogenous prion into the scrambled entity, which for common detectors may take weeks, with subsequent delays in achieving the results and increased risk of contagion for the laboratory

personnel. Immunological methods, based on the recognition of prions by capture and detection with specific antibodies also present severe drawbacks including the cross reactivity of PrP^{C} and PrP^{SC}, which requires the digestion of the sample with protease K, a process that may take several weeks, additionally increasing the uncertainty of the final results. None of the prion detection schemes have resulted yet in a method that allows fast, on-line monitoring of potentially contaminated products prior to consumption. In this context, surface enhanced Raman scattering (SERS) spectroscopy emerges as a viable alternative for the much needed direct detection of PrP^{SC} in biological fluids. SERS is not only one of the most sensitive analytical techniques but also can be used under biological conditions, and it is extremely sensitive to conformational changes in macromolecules such as proteins.[224] Unfortunately, SERS enhancement factors (EFs) obtained for conventional (non fluorescent) proteins are still very low, ranging between 10^3 and 10^5, despite much higher EFs obtained for highly aromatic molecules making possible even single molecule regimes of detection. There are two additional very serious challenges as well. Both quantitative detection by SERS and reproducible geometry of the "hot spot" necessary for SERS are difficult to achieve. The way to solve these challenges is to design and fabricate a highly organized photonic structure[225] that provides a high electromagnetic field enhancement in a reproducible geometry.[226,227] Recent demonstration of near field focalization by nanoantennas[228,229] has paved the way for development of ultrasensitive SERS substrates which can concentrate the near field within certain confined regions allowing one to obtain extremely high EFs.[230–232] Such a nanoantenna effect was predicted and found for nanorod (GNR) dimers, where the maximum focalization was found at the GNR tips.[233,234] One can hypothesize, therefore, that a highly organized system of GNRs acting as an extended nanoantenna may yield the desired answers to the SERS challenges of prion detection.

9.2 Experimental Section

9.2.1 Materials

Tetrachloroauric acid, silver nitrate, sodium borohydride, ascorbic acid, trisodium citrate, hydrochloric acid, cetyltrimethyl ammonium bromide (CTAB), oleylamine (OA, technical grade, 70%), chloroform (99%), ethanol (EtOH), benzenethiol (BT), serum albumin (SA), phosphate buffered solution (PBS) solution, prion protein fragment 106-126 (PrP^{C}), prion protein fragment 106-126 scrambled (PrP^{SC}) and bovine serum were purchased from Sigma-Aldrich. 1Naphthalenethiol (1-NAT) was obtained from Acros Organics. All chemicals were used as received. All glassware was washed with aqua regia prior to the experiments. Milli-Q deionized water (resistivity >18 $M\Omega cm^{-1}$) was used for all preparations.

9.2.2 Synthesis of monodisperse GNRs and supercrystals

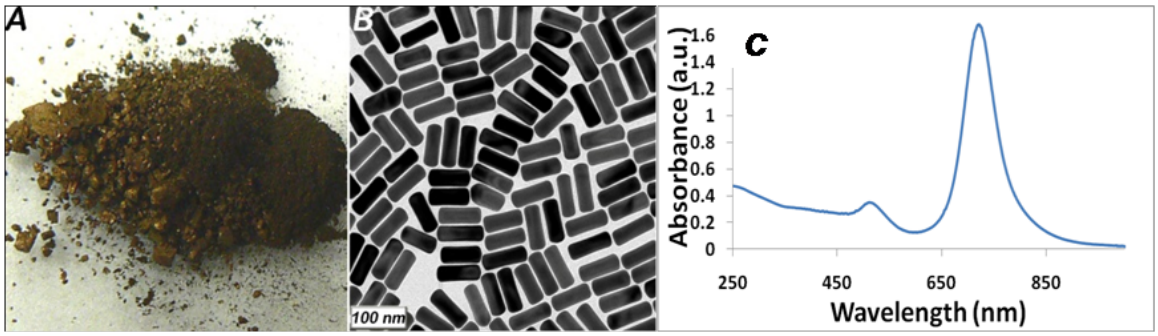

Figure 9.1: (A)Photograph of one gram of isolated gold nanorods and (B) their TEM image; (C) UV-vis absorption spectrum of NRs dispersion in water, used for the preparation of the supercrysals

GNRs were prepared by a modification of the usual seeded-growth method. Specifically, the growth solution was prepared by a two-fold increase in the concentration of Au (III) ions, $AgNO_3$, and ascorbic acid, whereas the amount of seed particles solution was increased from 12 µL to 9.6 mL as compared with the conventional method (see Section 9.2.4). The presence of a slight excess of ascorbic acid (0.1 mol equiv.

with respect to gold) promotes the growth of GNRs as soon as the seed solution is added. The GNRs reach the size of 45 nm in length and 10 nm in width within 2 h, at which point the growth stops although there is still nearly 80 % of the initial gold chloride present in solution. All these ions can be reduced and deposited onto the surface of the GNRs if an additional amount of ascorbic acid (1.1 mol equiv) is introduced at a very slow rate (0.001 mol equiv per hour). This slow process requires nearly 100 h, but as long as the rate of reduction is kept at that level, all gold ions are converted into metallic gold and deposited onto the original GNRs. The overall amount of the isolated GNRs produced by this protocol is more than one gram (Fig. 9.1(A)). This process leads to an amplification of the NRs dimensions, which reach 75 nm in length and 25 nm in diameter. Most importantly, the yield of the reaction becomes nearly quantitative (∼100 %) and the size distribution of NRs becomes much narrower (σ ∼3%) as shown in Fig. 9.1(B). Due to their narrow size distribution the GNRs have sharp peaks in the UV-vis absorption spectrum and (Fig. 9.1(C)) can crystallize into 3D colloidal crystals when a drop of their aqueous suspension is cast on a substrate and allowed to dry very slowly (7 days) in a saturated moist atmosphere.

9.2.3 Preparation of flexible gold ultra-long nanowire films for comparison of SERS effects

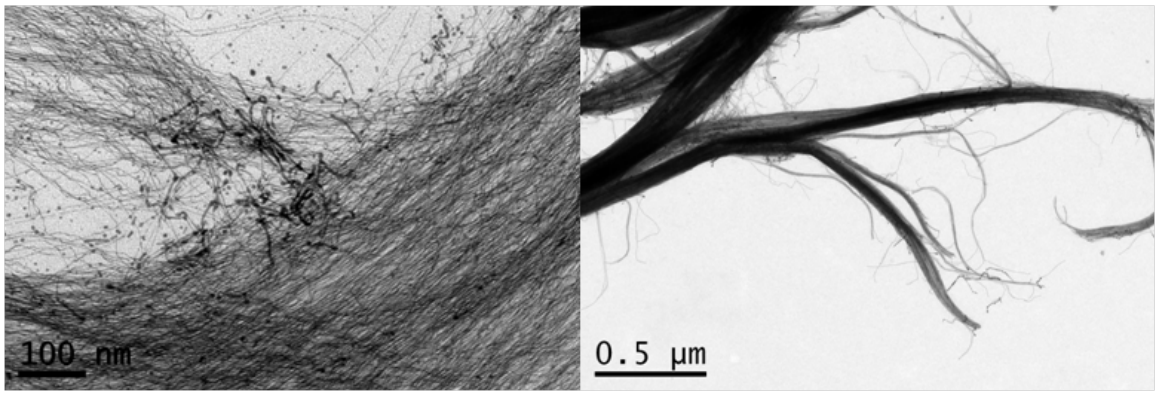

Figure 9.2: TEM images of the ultra-long rod nanowires at different magnifications

In a typical synthesis, $HAuCl_4$ (2.60 mg) was dissolved in OA (5 mL) by vortexing the mixture at room temperature until the solution turned from pale yellow, the characteristic color of OA, to an intense orange color, which indicates complex formation between Au^{3+} and OA. Thereafter, the solution was left undisturbed for 24 h, during which time the solution color changed again gradually from orange to pale yellow, indicating the reduction of Au^{3+} to Au^{+}. Next, the gold solution was aged for 5 days in a thermostatic bath at 35 ℃. Then, to 1 mL of this solution, 3 mL of $CHCl_3$ and 3 mL ethanol were added. The solution was centrifuged at 5000 rpm for 20 min. The supernatant was discarded and the precipitate redispersed in 3 mL $CHCl_3$. A second centrifugation step (4000 rpm, 60 min) was carried out after the addition of ethanol (3 mL), the supernatant was discarded and the precipitate redispersed in 3 mL $CHCl_3$ (Fig. 9.2). Films were prepared by drop-casting and air-drying 10 µL of the suspension on an ITO slide.

9.2.4 Preparation of gold nanorod films

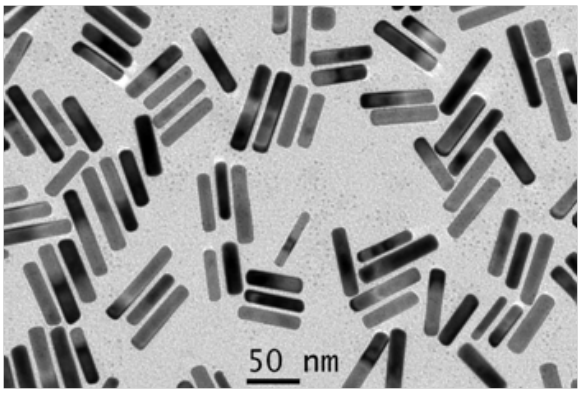

Figure 9.3: TEM image of the "as prepared" rods used for comparison

A solution of gold seeds was prepared by borohydride reduction of $HAuCl_4$ (0.25 mM, 5 mL) in aqueous CTAB solution (0.1 M). An aliquot of seed solution (24 µL) was added to a growth solution (10 mL) containing CTAB (0.1 M), $HAuCl_4$ (0.5 mM), ascorbic acid (0.8 mM), silver nitrate (0.12 mM) and HCl (19 mM). For the

deposition of the gold nanorods on silicon wafers, 2 mL of the as prepared suspension was centrifuged twice for 15 min, first at 6500 rpm and then at 4000 rpm. After discarding the supernatant, the precipitate was redispersed finally in 1 or 0.25 mL of water either to obtain non-aggregated particles (Fig. 9.3) or aggregated films made of rods with predominantly parallel orientation, respectively, by spin-coating 10 µL of the suspension on ITO slides. To prepare the fractal film of nanorods, the as prepared suspension was centrifuged five times (6000 rpm, 15 minutes) and, after discarding the supernatant, 10 µL of the precipitate, redispersed in 0.25 mL of water, was drop-cast on a ITO slide.

9.2.5 Preparation of citrate reduced silver nanoparticle fractal films

Silver nanoparticles were reduced by adding 1 mL of trisodium citrate (1%) to 50 mL boiling solution of $AgNO_3$ 10^{-3} M under stirring. The resulting solution was centrifuged (6000 rpm, 15 min) and, after discarding the supernatant, 10 µL of the precipitate was drop-cast on a ITO slide.

9.2.6 Characterization

TEM images were obtained using a JEOL JEM 1010 transmission electron microscope operating at an acceleration voltage of 100 kV. Solid thin films were characterized using a field emission scanning electron microscope (FE-SEM, JEOL JSM-6700f). Gold nanorod supercrystals were imaged and their scattering spectra acquired using a 100 W halogen lamp illumination source on a Nikon Eclipse TE-2000 inverted optical microscope coupled to a Nikon Dark-field Condenser (Dry, 0.95-0.80 NA). The scattered light from selected supercrystal areas was collected with a Nikon Plan Fluor ELWD 40×/0.60 NA objective and focused onto the entrance slit of a MicroSpec 2150i imaging spectrometer coupled with a TE-cooled CCD camera (PIXIS 1024B ACTON Princeton Instruments). The light scattered by the supercrystals was recorded in the

dark-field microscope with collection times of 20 s. SERS experiments were conducted with a micro-Raman Renishaw InVia Reflex system attached to a Leica microscope, a 2-dimensional CCD camera and an automated stage with 100 nm spatial resolution. The spectrograph used high-resolution gratings (1200 or 1800 g/mm) with additional bandpass-filter optics. Several laser excitation energies were employed, including laser lines at 633 (HeNe), 785 (diode) and 830 nm (diode). All measurements were made in confocal mode in backscattering geometry using a 100×/0.90 NA objective which provides a resolution of 500 nm. SERS maps were collected by using the Renishaw StreamLine accessory with a step size of 500 nm.

In order to characterize the gold crystal rods films, BT was adsorbed in gas phase over the whole surface of the films by casting a drop of BT (0.1 M in ethanol) in a Petri box where the film was also contained. Surfaces were then mapped using the Renishaw StreamLine accessory, taking mapping areas of 25×35 μm^2, with a step-size of 0.5 nm (1440 spectra each) upon excitation with three different laser lines: 633, 785 and 830 nm. Acquisition times were set to 200 ms with power at the sample of 1 mW. For comparison, the same experiments (following the same protocol) were carried out on the rest of the films (i.e. non-interacting GNRs, GNRs aggregated parallel to each other, fractally aggregated GNRs, and fractally aggregated AgNPs). Samples on ITO were cleaned with plasma previously to scanning electron microscopy characterization and SERS analysis. In the case of the supercrystals, samples were as well cleaned after the analyte exposure to check the efficiency in removing the organics and the possibility of reusing the sample. Plasma was generated in a Solarus™(Model 950) Advanced Plasma Cleaning System under the following conditions: 27.5 sccm (standard cubic centimeters per minute) O_2, 6.4 sccm H_2, 70 mTorr and exposition of 2 min.

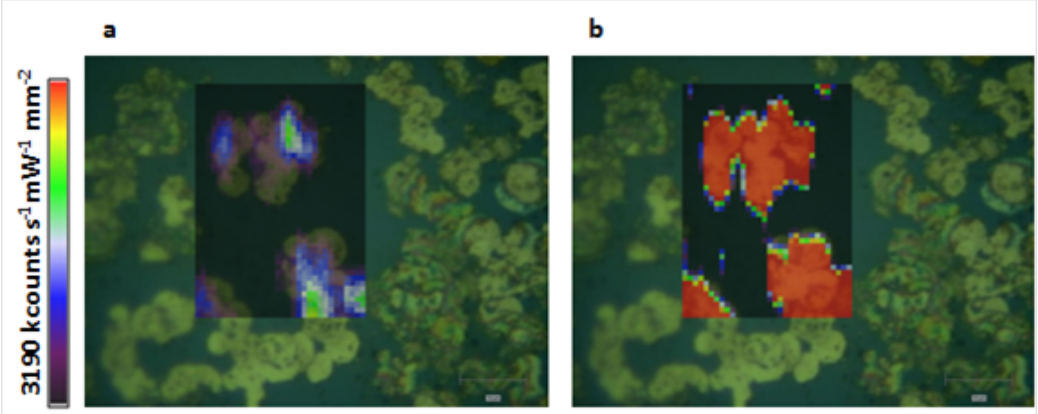

Figure 9.4: Effect of the plasma cleaning treatment. SERS mapping of BT adsorbed onto a supercrystal film before (A) and after (B) the plasma treatment. As observed, a substantial increase in the SERS intensity was obtained after cleaning mainly because of the removal of all the stabilizing agents present on the gold surfaces. Notably, no change in morphology of the supercrystal structure was observed. (λ_{ex}: 785 nm; StremLine maps carried out in confocal mode in backscattering geometry using a 100×/0.90 NA objective; acquisition time: 200 ms; power at the sample 1 mW; step-size 500 nm)

9.2.7 Reusability of the supercrystal films

Material recyclability was tested by exposing the substrate to BT in gas phase, cleaning the sample with the H_2-O_2 plasma (see above), and casting a dilute solution of 1-NAT (10 µL, 10^{-4}M). After each exposure, the sample was mapped with the Renishaw StreamLine accessory (55×67 µm^2, 500 nm step size with a total spectra collection of 14310 points) with the 785 nm laser line in the same conditions as described above. Mapping was carried out in two different spectral windows from BT 905 to 1190 cm^{-1} characteristic of BT and from 1670 to 1580 cm^{-1}, characteristic of 1-NAT. This procedure was repeated in several samples several times to ensure reproducibility.

9.2.8 Prion detection

Stock solutions of PrP^C and PrP^{SC} 10^{-4} M were prepared in PBS (12 mM NaCl, 0.27 mM KCl and 1 mM phosphate buffer salts). From these, PrP^{SC} solution was

consistently diluted in PrP^C solution (100, 50, 25, 10, 1 and 0% in PrP^{SC}). Then, 10 mL samples of each solution were cast each onto a different supercrystal film and studied with SERS (λ_{ex}: 785 nm, 10s, 1 mW of power at the sample). Ten points were collected for each sample to ensure reproducibility. This process was repeated as well on a single crystal film, cleaning it with the plasma after each analysis, with similar results. After setting the detection limit of PrP^{SC} in PrP^C to 1%, absolute detection limits of PrP^{SC} were determined by diluting the stock solution containing 1% of PrP^{SC} in 95% of PrP^{SC} until concentrations of 10^{-11} M. SERS spectra were acquired in the same conditions as described above. To probe the viability of this method to be implemented in real samples with no need for any complicated separation protocol, the same experiment was repeated using bovine serum as solution.

9.3 Results

We produced 75 nm × 25 nm (aspect ratio 3) GNRs on the basis of the seed-mediated method.[226,235] Modifications of the synthetic protocol resulted in improvements of the resulting GNRs, which are quite significant: (1) a 1000-fold increase in the amount of GNRs synthesized in one batch (Fig. 9.1) and, (2) very narrow size distributions ($\sim$ 3%). Consequently, GNRs were able to spontaneously and reproducibly crystallize into three-dimensional (3D) colloidal crystals (supercrystals) arranged as individual islands of fairly uniform dimensions (Fig. 9.5(A)) when the aqueous GNR dispersions were slowly dried in humid atmosphere (Fig. 9.5). Both the diameter (Fig. 9.5(B)) and height of individual GNR islands were in the range of one micron, which corresponds to $\sim$15 layers of GNRs perpendicular to the substrate. SEM examination revealed that the crystalline assemblies do not contain any grain boundaries and the orientational and positional order of individual GNRs is the same throughout the entire structure and from island to an island. The separation between the adjacent GNRs is approximately 3 nm, which corresponds to a

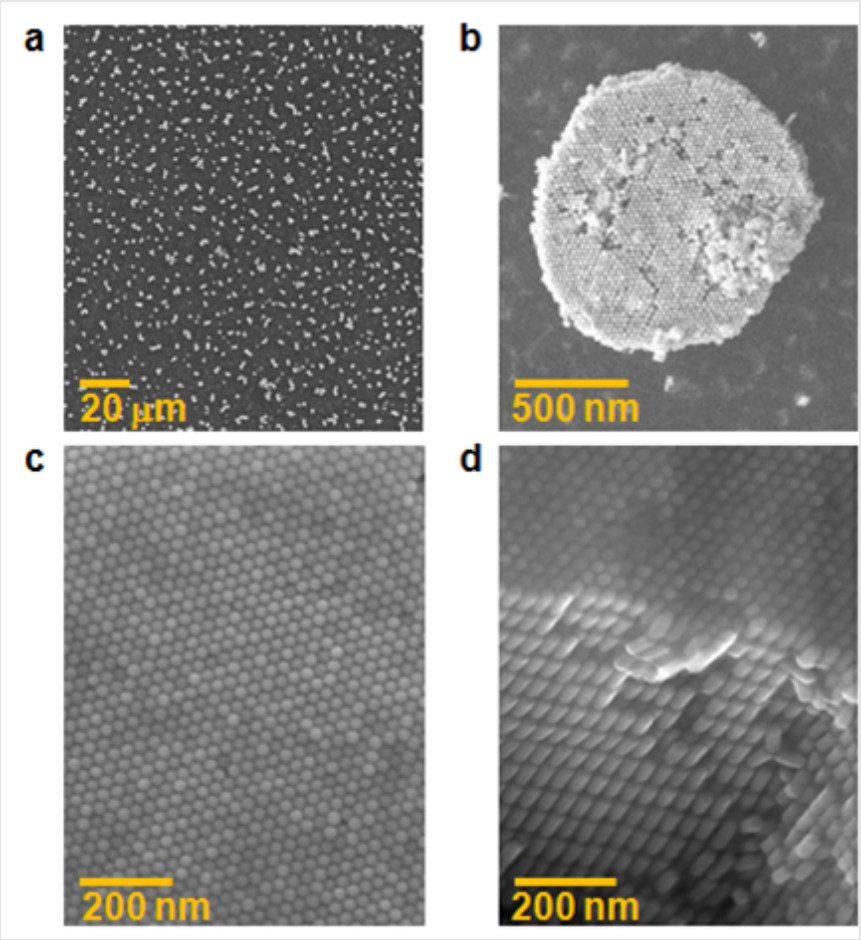

Figure 9.5: Nanorod supercrystals morphology. (A-C) SEM images corresponding to different magnifications of a typical nanorod supercrystal island film. (D) View from the edge of the supercrystal

bilayer of the cationic surfactant cetyltrimethyl-ammonium bromide (CTAB), and has been described as the optimal separation between particles for the generation of hot spots.[236,237]

The optical response of the supercrystals (Fig. 9.6(D)) was characterized using an inverted dark field microscope. The localized surface plasmon resonance (LSPR) was found to be very homogeneous throughout the entire surface and exhibits a maximum at 696 nm. Electric near-field enhancement simulations of different rod supercrystals support the hypothesis of the nanoantenna effect. Comparison of the simulations for a three layer rod-stacked supercrystal (Fig. 9.6(E)) and a single rod monolayer

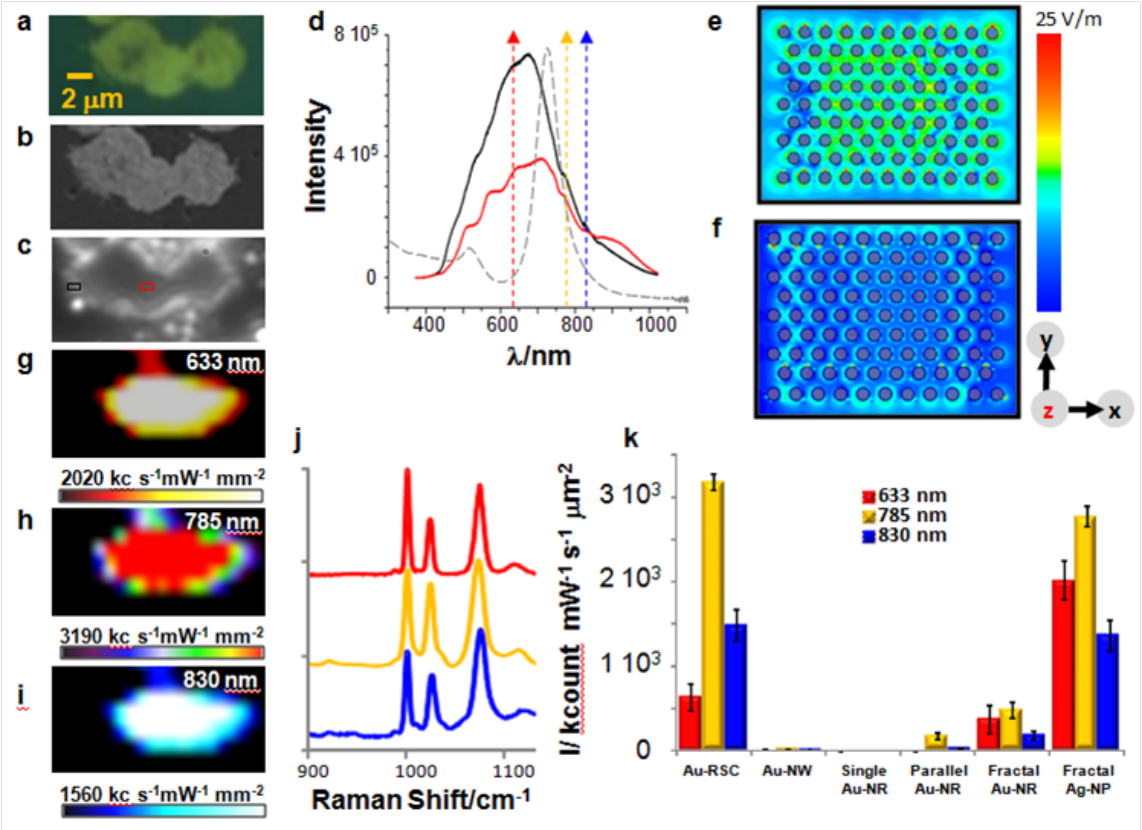

Figure 9.6: Optical properties of the nanorod supercrystals. (A-C) Optical, SEM, and dark field images of a GNR supercrystal, respectively, after plasma-etching removal of surfactant coating of the GNRs. (D) Localized surface plasmon resonance bands of the rods in solution (grey) and within a supercrystal, either at the center (black) or at the edges (red). Dotted arrows indicate the excitation laser lines used for SERS. (E-F), Electric field enhancement maps calculated for the top part of a three layer rod-stacked supercrystal (E) and for the same location in a single monolayer (F). (G-J), SERS intensity maps corresponding to the supercrystal in fig. (A), for BT as excited with a 633 nm (G), 785 nm (H) and 830 nm (I) laser lines, representative SERS spectra for each laser being presented in (J). (K) Comparison of the SERS intensities provided by a gold rod supercrystal (Au-RSC) film with common SERS substrates including, aggregated ultra-long nanowires (Au-NW), single rods, parallel and fractally aggregated gold GNRs (Single GNR, Parallel GNR and Fractal GNR, respectively), and fractally aggregated silver nanoparticles (Fractal Ag-NP). The intensity is the result of averaging over 50 different spots.

(Fig. 9.6(F)) indicate increased plasmon concentration on the top surface as layers of rods are added. Note that the field intensity between the rods in the middle of the stack is also very high (Fig. 9.7). The island morphology of the GNR film with tall columns of supercrystals (Fig. 9.5(A,B))helps taking advantage of the interstitial hot

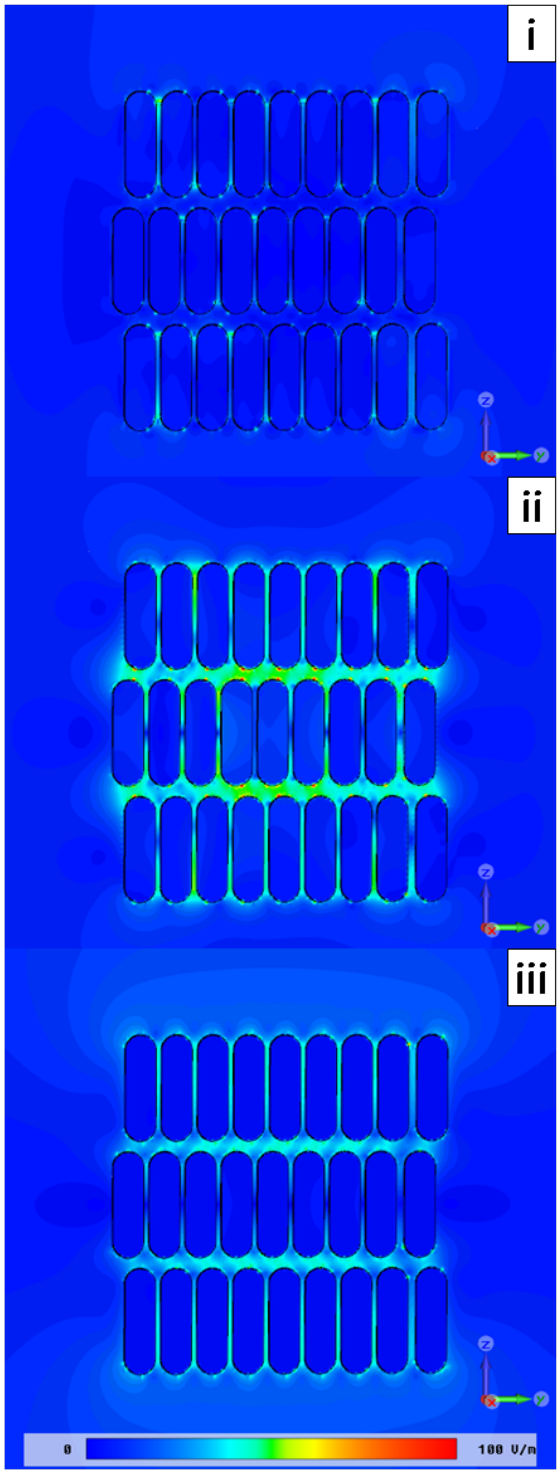

Figure 9.7: Simulated electric field map in the cross-section of supercrystal. Electric field map in the cross-section of the supercrystal at wavelengths (i) 428nm (ii) 750nm and (iii) 1000nm. The field enhancement in the gaps between subsequent layers of GNRs is clearly visible at the intermediate wavelength

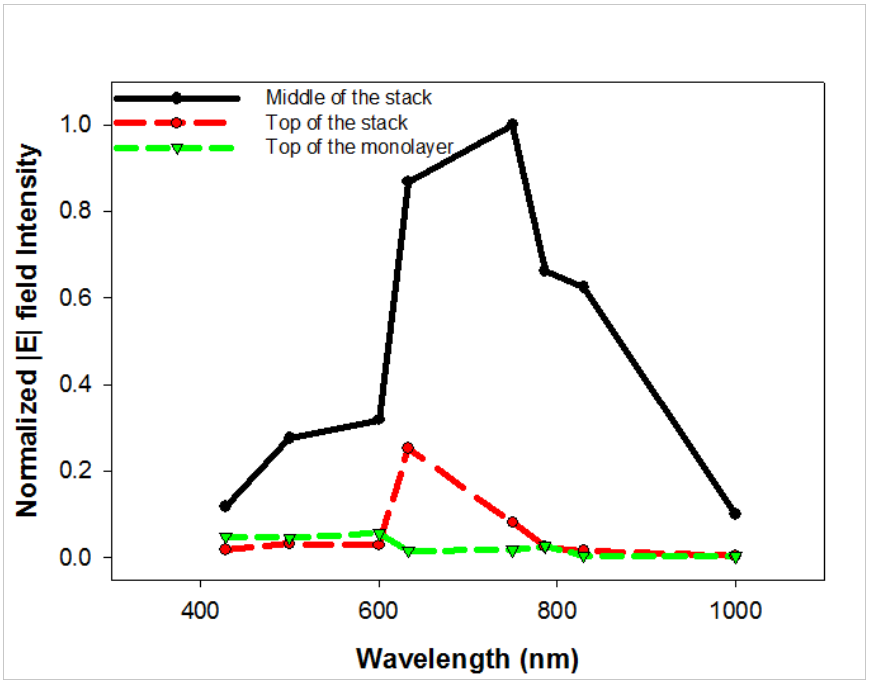

Figure 9.8: Simulated electric field intensity at various wavelengths in the cross-section of the crystal

spots accessible for analytes from the solution as well. Characterization of the SERS enhancing efficiency of GNR supercrystals was carried out in the same area, using benzenethiol (BT). A highly homogeneous intensity was registered for three different laser lines with an extremely high intensity for all of them, which is again consistent with the electric field calculations as shown in Fig. 9.8. The monolayer of GNRs have a very weak EF enhancement which is observed both theoretically (Fig. 9.8) and experimentally (Fig. 9.6(K)). The CST MICROWAVE STUDIO simulations can however include an error of upto 10% in the calculated electric fields due to limitations on number of mesh cells which could not be increased further because of limited computational capability. The electric field enhancements observed theoretically also do not include the specific interactions between the analyte molecules and the metal surface which can cause small deviations from the experimentally observed results. Extensive comparative testing revealed that GNR supercrystals as SERS substrates were largely superior to previously used arrangements of nanoparticles and GNRs,

including single particle, and fractally aggregated or parallel GNRs (Fig. 9.6(K)).[238] Additionally, islands of GNR supercrystals offer additional advantages for bioanalysis compared to the best SERS substrates so far, i.e. fractal Ag films.

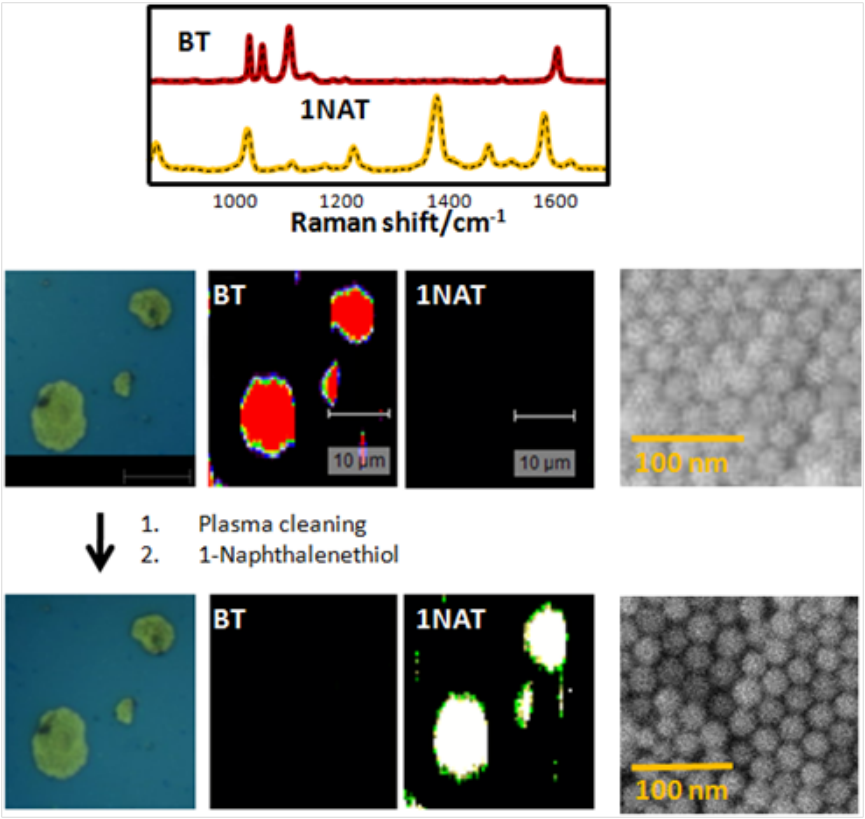

Figure 9.9: Reusability of supercrystals after plasma cleaning. SEM images and SERS spectra and mapping of a supercrystal before and after cleaning the first analyte (BT) and adding a different one (1-NAT)

They include higher chemical stability of gold over silver, reproducibility, and highly homogeneous distribution of field intensity making possible quantitative SERS detection of complex biomolecules. To that one might add as well mechanical stability of the islands of the GNR supercrystal, which allows multiple use of the substrates upon plasma etching of the previous analyte, which can be exemplified by SERS analysis of BT and a second molecular probe (1-naphthalenethiol, 1-NAT) on the same GNR crystal upon plasma etching of BT (Fig. 9.9). Notably, after cleaning, no signal of BT was registered even when mapping a large area (30×30 μm^2) while

the morphology of the supercrystal remained unalterated and the SERS intensity was still extremely high.

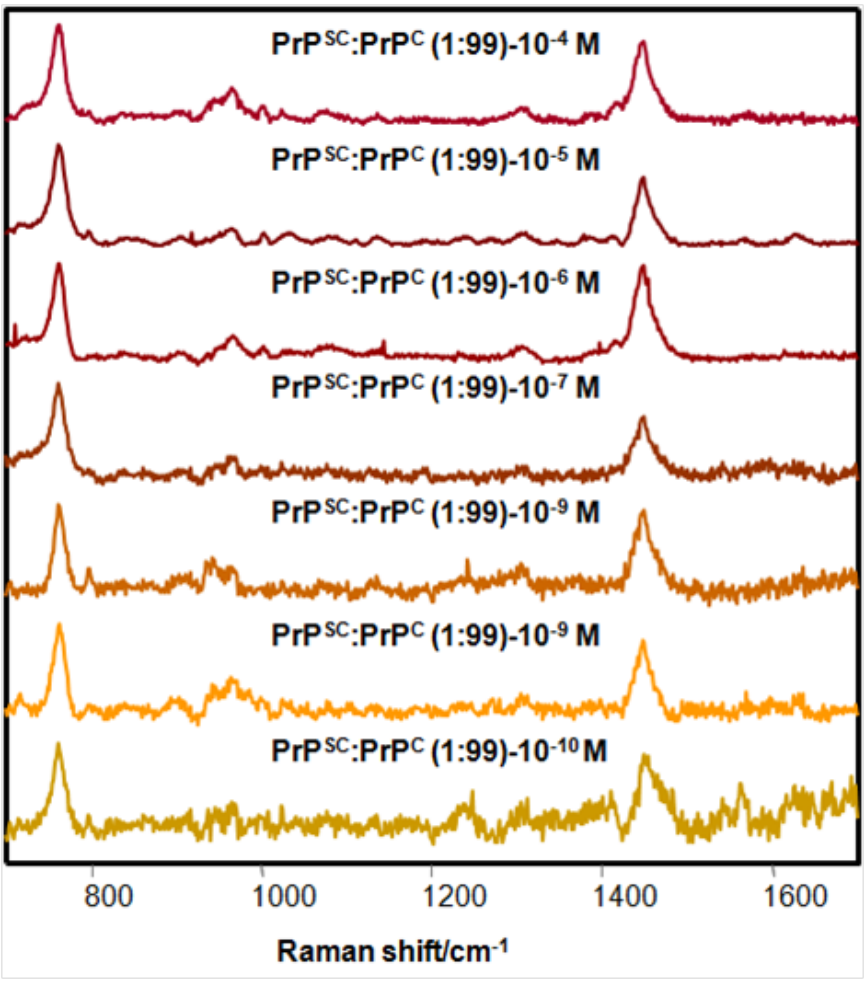

Figure 9.10: SERS spectra of PrP^{SC}:PrP^{C} mixtures (1:99) in decreasing concentration. Signal of the scrambled prion can be detected until concentration of total prion of 10^{-12} M (10^{-12} M if considering the initial concentration of scrambled prion). (λ_{ex}: 785 nm; StremLine maps carried out in confocal mode in backscattering geometry using a 100×/0.90 NA objective; acquisition time: 10 s; power at the sample 1 mW).

The unique potential of these SERS substrates was thus exploited for the ultrasensitive detection of scrambled prions within complex mixtures (natural serum). Due to the high intrinsic toxicity of these materials and the requirement of a biosecurity lab level 3 for their manipulation, we selected a model peptide (106-126, Fig. 9.11(A)), widely used to investigate prion diseases[239] as it forms fibrils in vitro and causes apoptotic cell death in neuron culture. First, we investigated the SERS spectra of

the biologically active and the scrambled prion in PBS. Then we studied the lower proportion of PrP^{SC} in PrP^{C} that can be unambiguously determined. Because the structures of both prions are very similar, so are their respective vibrational patterns (Fig 9.10). SERS is dominated by a band at 762 cm^{-1} assigned to the interaction of Au-S-C, and a triplet in PrP^{C} (1390, 1416 and 1446 cm^{-1}) which becomes a singlet (1448 cm^{-1}) in the scrambled version. These bands are related to the side chain bands together with the amide II and III modes, especially in the -Met-Lys-His-Met- fragment, responsible for the binding of the peptide to the gold surface. It is important to bear in mind that, when prions are mixed, spectral patterns from the misfolded prion are fully identifiable even when its relative concentration is as low as 1% that of the normal prion. This is probably due to induction of the misfolding of PrP^{C} by PrP^{SC}. On the other hand, by systematically diluting the mixture containing 1% PrP^{SC} and 99% PrP^{C} we were able to detect scrambled prion signal down to a total prion concentration of as low as 10^{-10} M. This is equivalent to 10 molecules per area sampled, i.e. zeptomol regime (Fig. 9.10).

9.4 Conclusions

Such high sensitivity may make possible fast real-time detection of prions in a real complex matrix, such as blood serum, which was never possible before.[240] The SERS spectrum of PrP^{SC}:PrP^{C} in serum (Fig. 9.11(E)) is dominated by bands corresponding to the C-N stretching (1118 cm^{-1}), Phe (1003, 1033 cm^{-1}), Trp (1011 and 1560 cm^{-1}), Tyr (845 cm^{-1}) and Cys (720 cm^{-1}). Upon sequential dilution of the prion mixture (1% of PrP^{SC} in 99% of PrP^{C}) in serum, the characteristic prion bands can still be clearly recognized down to concentrations as low as 10^{-10} M. The fact that the prion proteins can be observed clearly identified in serum, a complex solution containing high concentrations of proteins, mainly albumins but also globins, electrolytes, antibodies, antigens, hormones, and any exogenous substances (e.g., drugs

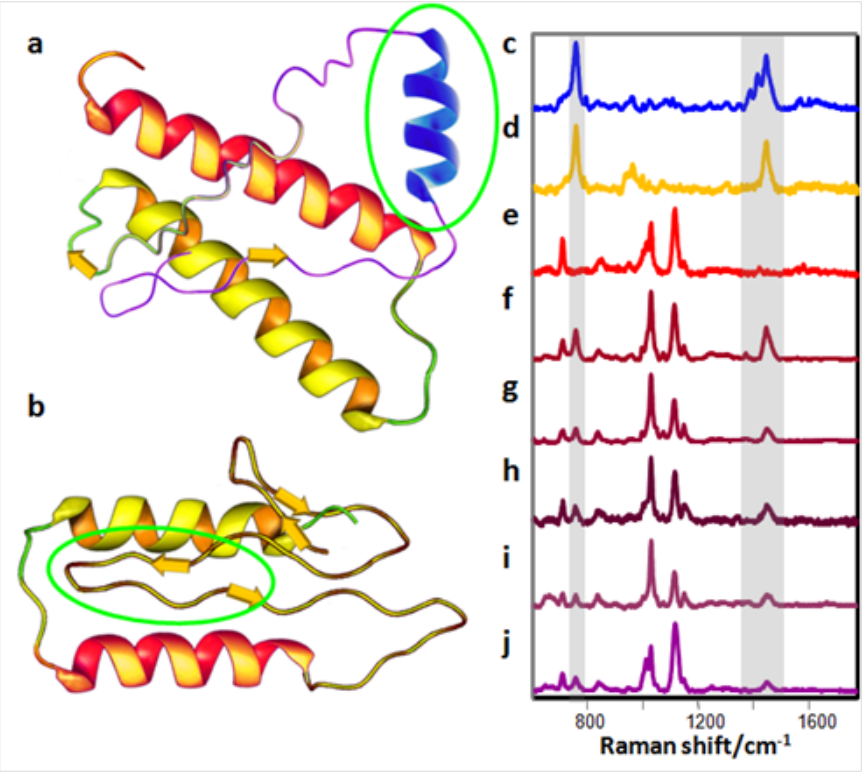

Figure 9.11: Scheme showing the prion mutation and detection limits for the scrambled version in bovine serum. (A) Biologically active (PrP^C α-helix) and (B) scrambled (PrP^{SC} β-sheet) prions; the fragment corresponding to 106-126 peptide is highlighted in green. SERS spectra of (C), PrP^C α-helix) (D), PrP^{SC} (scrambled) and (E), bovine serum. (F-J), Detection limits of PrP^{SC}:PrP^C (1:99) in bovine serum, at 10^{-6}, 10^{-7}, 10^{-8}, 10^{-9}, and 10^{-10} M in total prion, respectively

and microorganisms) is likely to indicate the high affinity of prions for gold, which is in agreement with the capacity of -Met-Lys-His-Met- groups present in prions to efficiently chelate Au atoms.[241]

In summary, highly organized supercrystals of GNRs with plasmonic antennae enhancement of electrical field have made possible the first real-time detection of prions in complex biological media such as serum. The particular nanoparticle morphology and three-dimensional organization render these systems excellent SERS substrates with uniform electric field enhancement, leading to both sensitive and reproducible EFs in the desirable spectral range.

CHAPTER X

Conclusions and Future Work

10.1 Summary of results

With intrinsic advantages including small sizes, ease of preparation and bioconjugation, unique optical properties, as well as good biocompatibility, GNRs have been explored for potentially wide application in drug delivery, cellular imaging, and biomedical diagnostics. This dissertation reports novel developments in the field of targeted contrast agents for PAI as well as organization and self-assembly of GNRs for application as SERS substrates and metamaterials. The following is a brief summary of results.

Chapter II demonstrates the feasibility of photoacoustic imaging of inflammatory responses using bioconjugated GNRs. To target the stimulated cells, GNRs were conjugated to anti-intercellular adhesion molecule-1 (ICAM-1) which binds to cell surfaces over expressing ICAM-1. A monolayer of stimulated endothelial cells labeled with bioconjugated GNRs was scanned using a high frequency transducer. Photoacoustic images differentiated inflamed cells from control cells and matched well with fluorescence images. This technology may permit identification of critical inflammation sites such as blood vessels responsible for cardiovascular diseases. Chapter III investigated the potential of photoacoustic imaging in noninvasive monitoring of anti-TNF drug delivery. After the contrast agent composed of GNRs conjugated with

Etanercept molecules was produced, ELISA experiments were performed to prove the conjugation and to show that the conjugated anti-TNF-α drug was biologically active. PAI of *ex vivo* rat tail joints with the joint connective tissue enhanced by intra-articularly injected contrast agent was conducted to examine the performance of PAT in visualizing the distribution of the gold-nanorod-conjugated drug in articular tissues. By using the described system, GNRs with a concentration down to 1 pM in phantoms or 10 pM in biological tissues can be imaged with good signal-to-noise ratio and high spatial resolution. This study demonstrated the feasibility of conjugating TNF antagonist pharmaceutical preparations with GNRs, preservation of the mechanism of action of TNF antagonist along with preliminary evaluation of novel PAI technology in imaging optical contrast agents conjugated with anti-rheumatic drugs. In future studies, PAI of drug delivery monitoring will be conducted on arthritic animal models in vivo with systemic administration of drug-conjugated GNRs. We expect that PAI enhanced by a novel gold nanoparticle contrast agent may contribute considerably to the more efficient evaluation of drug effects in living laboratory animals and to optimize therapeutic decisions in human clinical practice in the future.

Many nanoparticle contrast agents have difficulties with deep tissue imaging. In Chapter IV, we have investigated the potential of emerging photoacoustic imaging and nuclear imaging in monitoring of anti-rheumatic drug delivery by using a newly developed dual modality contrast agent. After the contrast agent composed of GNRs conjugated to the anti-tumor necrosis factor (anti-TNF-α) drug Etanercept was produced, it was radiolabeled by ^{125}I. ELISA experiments designed to test tumor necrosis factor binding were performed to prove the specificity and biological activity of the radiolabeled conjugated contrast agent. Photoacoustic and nuclear imaging were performed to visualize the distribution of GNRs in articular tissues of the rat tail joints in situ. Findings from the two imaging modalities corresponded well with each other in all experiments. Our system can image GNRs down to a concentration of 10 pM

in biological tissues and with a radioactive label of 5 μCi. This study demonstrates the potential of combining photoacoustic and nuclear imaging modalities through one targeted contrast agent for non-invasive monitoring of drug delivery. Chapter V describes a novel technique to monitor *in vivo* behavior of GNRs using γ-imaging. GNRs were radiolabeled using [^{125}I] sodium iodide in a simple and fast manner with high yield and without disturbing optical properties. Radiolabeled GNRs were successfully visualized by the radioisotope tag, allowing longitudinal in vivo studies to be performed repeatedly on the same animal. The preliminary biodistribution study showed that Polyethylene glycol (PEG) GNRs have much longer blood circulation times and clear out faster, while bare GNRs accumulate quickly in the liver after systematic administration. The highly efficient method reported here provides an extensively useful tool for guidance of design and development of new gold nanoparticles as target-specific agents for both diagnostics and photothermal therapy.

X-ray based computed tomography (CT) is among the most convenient imaging/diagnostic tools in hospitals today in terms of availability, efficiency, and cost. However, in contrast to magnetic resonance imaging (MRI) and various nuclear medicine imaging modalities, CT is not considered a molecular imaging modality since targeted and molecularly specific contrast agents have not yet been developed. Chapter VI describes a targeted molecular imaging platform that enables, for the first time, cancer detection at the cellular and molecular level with standard clinical CT. The method is based on gold nanoprobes that selectively and sensitively target tumor selective antigens while inducing distinct contrast in CT imaging (increased X-ray attenuation). We present an in vitro proof of principle demonstration for head and neck cancer, showing that the attenuation coefficient for the molecularly targeted cells is over 5 times higher than for identical but untargeted cancer cells or for normal cells. We expect this novel imaging tool to lead to significant improvements in cancer therapy due to earlier detection, accurate staging, and microtumor identification.

Apart from application as a contrast agent, gold nanorods due to their anisotropic shape also form interesting building blocks for 3D superstructures with wide range of optical properties for applications in plasmonics, metamaterials and sensors. GNRs in different arrangements represent the most plausible system for the creation of negative refractive index materials (NIMs) in the optical frequency range. Among other challenges, one of the major limitations of present day NIMs is their large amount of energy dissipation which frustrates the restoration of near field modes. To take advantage of exciton-plasmon interactions, an optical system consisting of semiconductor nanoparticles (NPs) and GNRs that can continuously pump energy into the NIM resonator is described in Chapter VII. Superstructures with promising properties were achieved by assembly of CdTe nanoparticles on the surface of nanorods by using streptavidin-biotin bioconjugation where NP→GNR energy transfer occurs with great efficiency. On the initial layer of bioconjugated NPs, the second layer is formed due to nonspecific interactions, which is manifesting in unusual spectral behavior and dependence of lifetime on NP concentration. By varying the ratio of NPs per GNR, the amount of energy transfer can be controlled, while the diameter of NPs and wide overlap offers the possibility to tune the wavelength of the pumping light. Although the individual response of anisometric nanoparticles may be strongly direction dependent, assemblies of randomly oriented GNRs are isotropic. To access the full range of possible materials responses in dispersions, control over orientation is required. GNRs can be oriented by electric fields, but if the dispersing medium is aqueous, the alignment is poor unless the rods are very long. Chapter VIII describes a simple novel technique for the phase transfer of aqueous GNRs to non-aqueous solvents. It is demonstrated that in such solvents, a high degree of alignment ($S \approx 0.9$) can be achieved by an external electric field even for short aspect ratio GNRs.

Fast in-situ detection of prion infections in biological samples of complex composition has numerous levels of difficulties stemming from their structural analogy

to functional form of chemically identical peptides. This task has equally numerous levels of significance both for public health and expansion of the boundaries of analytical techniques. Surface enhanced Raman scattering (SERS) has the ability to detect single aromatic molecules, but it has not proven successful so far in the case of peptides, which would require purposeful design of SERS plasmonic substrates. Chapter IX demonstrates that supercrystals of GNRs with nanoantenna effect enhancing electromagnetic field on the top of the supercrystal and highly reproducible structure make possible real-time monitoring of prion presence in serum. Simulations by CST MICROWAVE STUDIO confirm the nanoantenna effect and large electric field enhancements.

10.2 Future research directions

10.2.1 Simultaneous PAI of multiple inflammatory biomarkers

Understanding and monitoring the bioactivity of the inflammatory responses will provide prognostic information of the major systemic diseases such as atherosclerosis. Some inflammatory biomarkers have predictive value for future vascular events. Multiple targeting of different biomarkers using GNRs of different aspect ratios for optical absorption centered at different wavelength will enable simultaneous detection of different inflammatory responses. Preliminary in vitro cell experiments demonstrate the feasibility to detect the over expressions of ICAM-1 and E-selectin simultaneously by photoacoustics.

10.2.1.1 Preliminary results

HUVECs were cultured on gelatin-coated glass slides, and inflammation was induced by IFN-γ and TNF-α. At 0, 2, 6, 24 hrs after the stimulation, slides exposed to GNRs 800 nm -conjugated FITC labeled anti-ICAM-1 or GNRs 800 nm-

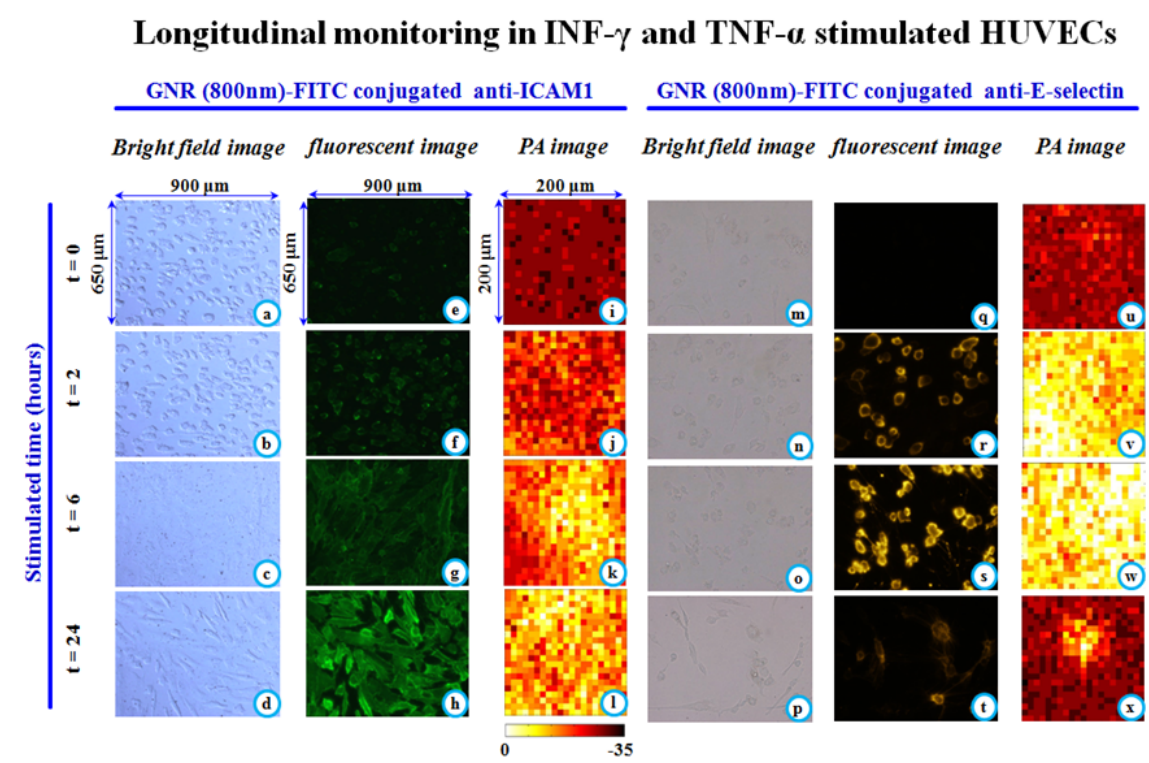

Figure 10.1: Bright field (A-D & M-P), Fluorescent (E-H & Q-T), and Photoacoustic (I-L & U-X) images for both ICAM targeted imaging (left panels) and E-Selectin (right panels) at various time points

conjugated biotinylated anti-E-Selectin. The expression of each biomarker was visualized by direct fluorescence imaging of the FITC label or fluorescent imaging using PE-streptavidin. Expression was also quantified by rt-PCR. For Photoacoustic (PA) scanning, the top surface of the cell culturing slide was illuminated by a pulsed laser beam at 800 nm (Nd:YAG, 5 ns, 10 Hz, 4 mJ/cm^2). A high frequency ultrasonic transducer (60 MHz) connected to a motorized X-Y stage was used to scan the PA signal over the area of 200 µm by 200 µm with 10 µm step size. Fig. 10.1 illustrates the corresponding bright field (A-D & M-P), fluorescent (E-H & Q-T), and PA (I-L & U-X) images for both ICAM targeted imaging (left panels) and E-Selectin (right panels) at various time points. Overall PA signal intensity level is comparable to fluorescence image intensity at these time points. rt-PCR confirms the up-regulation of mRNA similar levels along this time course. It is demonstrated that PAI using bio-

conjugated GNR as targeted contrast agent can detect and monitor the up-regulation of ICAM-1 or E-selectin simultaneously in HUVECs. Future work would involve simultaneous targeting of several biomarkers and studying the in vivo behavior of the targeted contrast agents. Simultaneous targeting could also prove useful in scanning patients for various kinds of cancer cells in body through a single dose of contrast agent.

10.2.2 Chiral nanocomposites

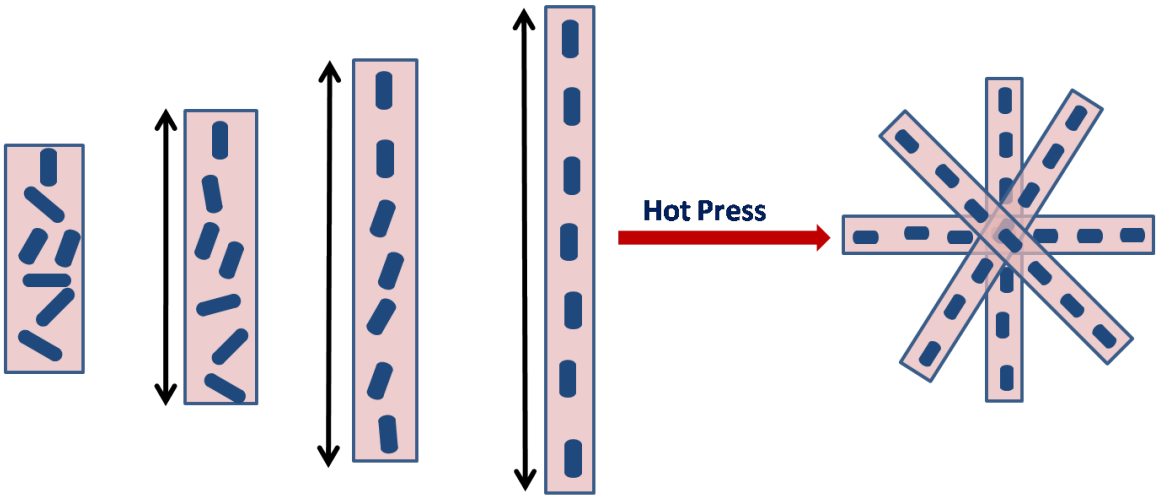

Figure 10.2: Schematic of chiral nanocomposite from LBL films

Negative Index Materials (NIMs) because of their ability to refract light on the opposite side of the normal have the most intriguing optical properties which may find application in construction of perfect lens and cloaking devices. The two most actively pursued approaches to NIMs are via using resonating metallic nanostructures and photonic crystals. Recent theoretical investigations have showed that NIMs can also be realized through chiral materials if the chirality is sufficiently strong. The current work is an effort to realize chiral negative index materials by using resonating metallic nanorods in polymers to create highly chiral nanocomposites. Anisotropic gold nanorods are aligned inside stretched thin polymer films to create strong po-

larizers owing to the LPR. The stretched films are then piled on at a rotating angle and hot pressed into one composite film (Fig. 10.2). The dependence of chirality on the concentration of gold nanorods, piling angle and thickness of the composite need to be invstigated. One of the biggest advantages of this system is that a chiraly active material can be achieved over a large range of wavelength simply by tuning the absorption of the rods.

10.2.2.1 Preliminary results

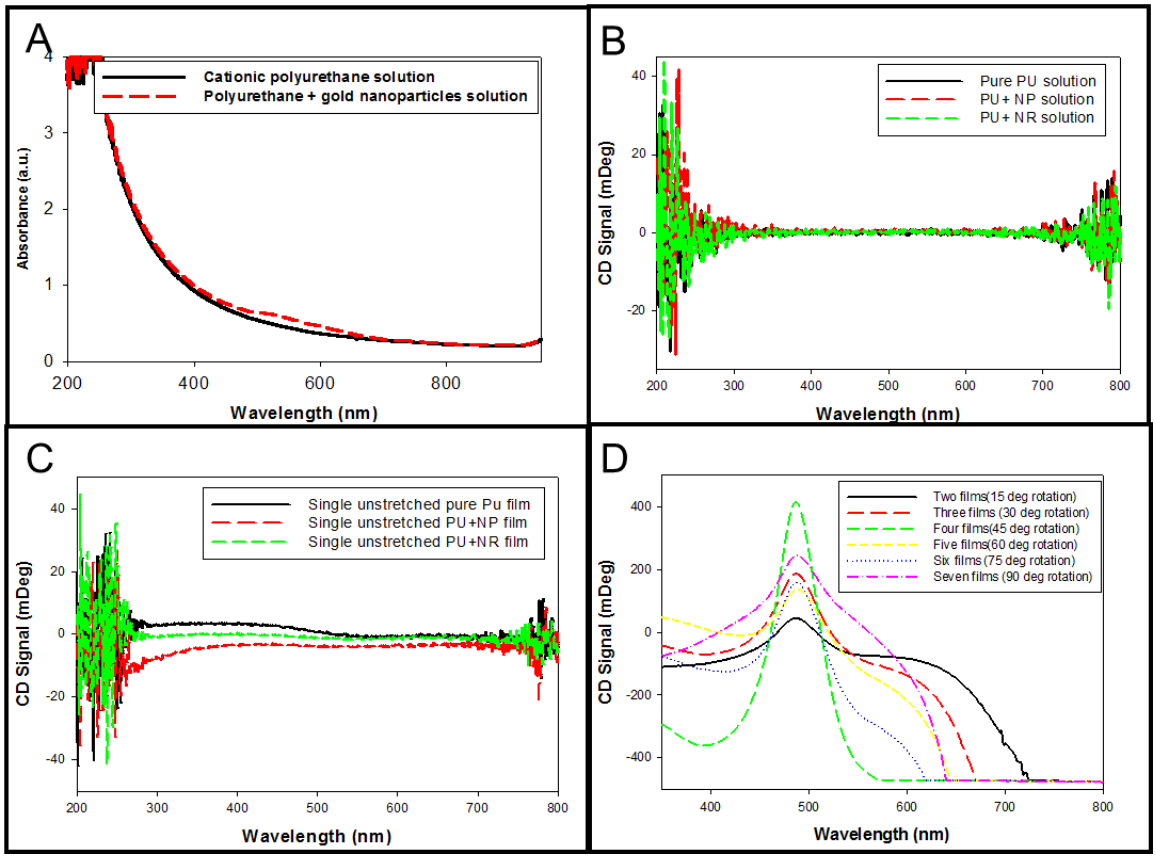

Figure 10.3: (A) UV-Vis absorption of PU and PU+GNRs dipersion. (B) CD spectrum of polymer dispersions. (C) CD spectrum of single stretched films (D) CD spectrum of chiral nanocomposites

Cationic Polyurethane (PU) films are nearly transparent and have excellent mechanical properties. Previous reports from our group have showed that PU films are capable of withstanding high strain values[242,243] which is a highly desirable prop-

erty to align GNRs via stretching.[209,244] Initial experiments with bulk polyurethane (PU) doped with GNRs provided encouraging results. Stretched PU films doped with GNRs were affixed on polycarbonate substrate and stacked on top of each other at various angles. The substrate is placed under a hot press at 100 ℃ and 7 MPa pressure for 5 hours to produce the chiral nanocomposite. It was observed that single stretched films of PU, PU+NP and PU+GNRs have nearly zero circular dichorism (CD). However the nanocomposite from stretched films have strong chiral signal at 500 nm corresponding to the transverse plasmon peak and the second peak corresponding to the stronger longitudinal plasmon does not appear due to saturation of the photodetector in CD machine. The signal is also dependent on the angle at which the films are stacked (Fig. 10.3(D)). It is to be noted that CD signal from stretched films is a sum of linear dichorism (LD), linear birefringence (LB), circular dichorism and circular birefringence (CB).[245,246]

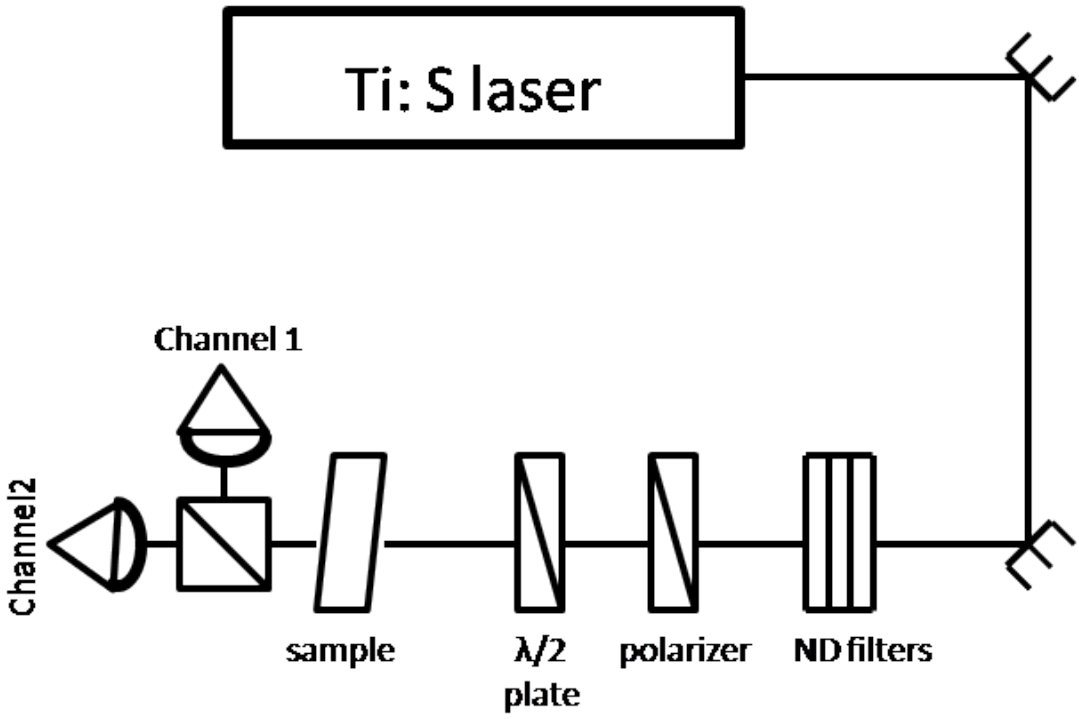

Figure 10.4: Schematic of the setup for measuring rotation in polarization

Due to the presence of single photodetector in a standard CD machine it is difficult

to find the individual contributions of LD, LB and CB which may be contributing a lot to the overall signal. In order to overcome this problem a setup shown in Fig. 10.4 was designed to evaluate the rotation in polarization of light from the chiral nanocomposites. The beam from Ti:S laser is passed through a set of neutral density filters to reduce the peak power and either a half-wave plate or quarter wave plate is used to generate linear or circularly polarized light. After the incoming beam passes through the sample, a beam splitter is placed in the path to separate light into linear components which are measured at respective detectors connected to an oscilloscope.

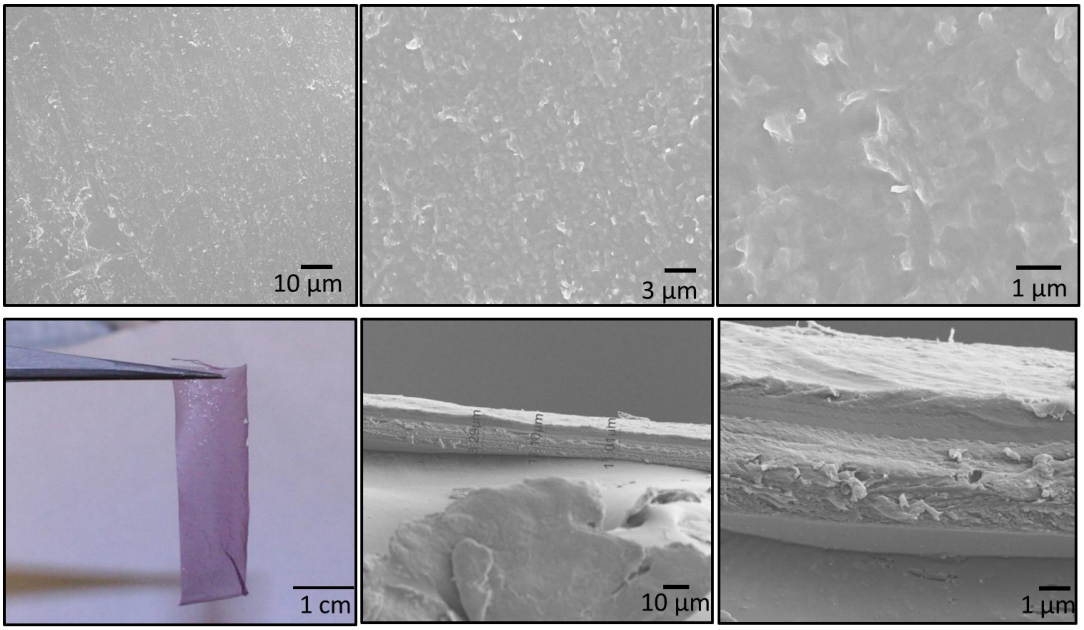

Figure 10.5: (A-C) SEM image of polyurethane GNR exponential LBL film. (D) Optical photograph of free standing LBL film. (E-F) SEM image of the cross-section of LBL film

Also due to the requirement of thin films for stronger effective chirality of a medium it was imperative to build films by Layer-by-Layer (LBL) technique instead of curing bulk PU+GNRs dispersion. Exponential LBL films were made using $(PU/PAA/GNR/PAA)_n$ where the concentration of PU and dipping time in GNRs solution was optimized to obtain films with high loading of GNRs and high strain bearing capacity (Fig. 10.5). The ellipsometric measurements showed that the growth

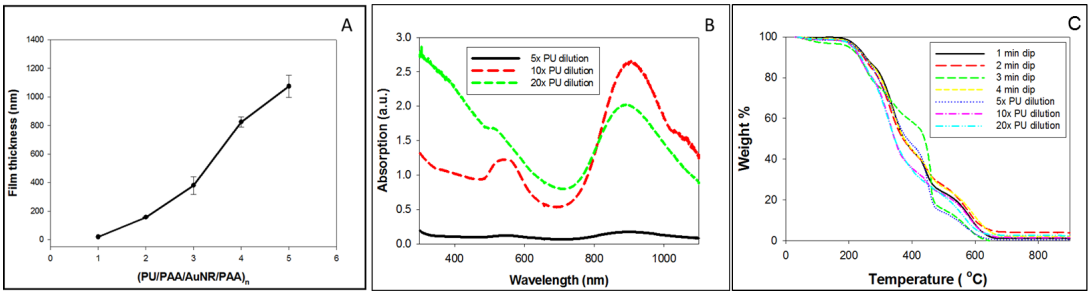

Figure 10.6: (A) Ellipsometric measurements on LBL film (B) UV-Vis absorption of LBL films made under different experimental conditions (C) Thermogravimetric Analysis of LBL films made under different experimental conditions.

of film is exponential (Fig. 10.6(A)) and it was measured by SEM to be 11 µm after 40 quadlayers. The UV-Vis data suggested that at lower PU dilutions the loading of GNRs is poor and at higher dilutions the plasmons of GNRs get broadened possibly due to higher loading of GNRs (Fig. 10.6(B)). Thermo gravimetric analysis (Fig. 10.6(C)) showed that the metal content in the film is about 2 wt% and the most optimum dipping time in GNR solution is 2mins.

Future work involves in depth optical characterization of the chiral nanocomposites made from LBL thin films using the setup described in Fig. 10.4. The setup under certain limitations will help uncouple the contribution of LD, LB and CB to the overall CD signal. It will be interesting to explore and investigate different polymer systems. In order to achieve strong chirality necessary for NIMs it might be required to further decrease the thickness of films while retaining the mechanical properties. Metallic losses due to operation near resonance will be among the many challenges to realize optical NIMs through chirality, which will require potential gain materials similar to those described in Chapter VII.

BIBLIOGRAPHY

[1] J. B. Pendry, "Negative refraction makes a perfect lens," *Physical Review Letters*, vol. 85, no. 18, pp. 3966–3969, 2000.

[2] R. Y. Tsien, "Imagining imaging's future," *Proc. Natl Acad. Sci. USA*, vol. 87, pp. 3112–3116, 1990.

[3] G. Shvets, "Photonic approach to making a material with a negative index of refraction," *Physical Review B*, vol. 67, no. 3, p. 035109, 2003.

[4] A. Ito, M. Shinkai, H. Honda, and T. Kobayashi, "Medical application of functionalized magnetic nanoparticles," *Journal of Bioscience and Bioengineering*, vol. 100, no. 1, pp. 1–11, 2005.

[5] S. A. Wickline and G. M. Lanza, "Nanotechnology for molecular imaging and targeted therapy," *Circulation*, vol. 107, no. 8, pp. 1092–1095, 2003.

[6] H. F. Zhang, K. Maslov, G. Stoica, and L. V. Wang, "Functional photoacoustic microscopy for high-resolution and noninvasive in vivo imaging," *Nature Biotechnology*, vol. 24, no. 7, pp. 848–851, 2006.

[7] M. Xu and L. V. Wang, "Time-domain reconstruction for thermoacoustic tomography in a spherical geometry," *IEEE transactions on medical imaging*, vol. 21, no. 7, pp. 814–822, 2002.

[8] X. Wang, Y. Pang, G. Ku, X. Xie, G. Stoica, and L. V. Wang, "Noninvasive laser-induced photoacoustic tomography for structural and functional in vivo imaging of the brain," *Nature Biotechnology*, vol. 21, no. 7, pp. 803–806, 2003.

[9] X. Wang, Y. Pang, G. Ku, G. Stoica, and L. V. Wang, "Three-dimensional laser-induced photoacoustic tomography of mouse brain with the skin and skull intact," *Optics Letters*, vol. 28, pp. 1739–1741, 2003.

[10] A. A. Oraevsky, A. A. Karabutov, and E. V. Savateeva, "Enhancement of optoacoustic tissue contrast with absorbing nanoparticles," in *Proceedings of SPIE*, vol. 4434, p. 60, 2001.

[11] A. A. Oraevsky, S. L. Jacques, R. O. Esenaliev, and F. K. Tittel, "Time-resolved optoacoustic imaging in layered biological tissues," *Advances in Optical Imaging and Photon Migration*, vol. 21, pp. 161–165, 1994.

[12] R. A. Kruger, D. R. Reinecke, and G. A. Kruger, "Thermoacoustic computed tomographytechnical considerations," *Medical Physics*, vol. 26, p. 1832, 1999.

[13] R. A. Kruger and P. Liu, "Photoacoustic ultrasound: Pulse production and detection in 0.5% liposyn," *Medical physics*, vol. 21, p. 1179, 1994.

[14] R. A. Kruger, W. L. K. Jr, A. P. Romilly, and P. Scmidt, "Thermoacoustic CT of the breast: Pilot study observations," in *Proceedings of SPIE*, vol. 4256, p. 1, 2001.

[15] R. G. M. Kolkman, E. Hondebrink, W. Steenbergen, and F. F. M. D. Mul, "In vivo photoacoustic imaging of blood vessels using an extreme-narrow aperture sensor," *IEEE Journal of selected topics in quantum electronics*, vol. 9, no. 2, pp. 343–346, 2003.

[16] C. G. A. Hoelen, F. F. M. D. Mul, R. Pongers, and A. Dekker, "Three-dimensional photoacoustic imaging of blood vessels in tissue," *Optics letters*, vol. 23, no. 8, pp. 648–650, 1998.

[17] R. Fainchtein, B. J. Stoyanov, J. C. Murphy, D. A. Wilson, and D. F. Hanley, "Local determination of hemoglobin concentration and degree of oxygenation in tissue by pulsed photoacoustic spectroscopy," in *Proceedings of SPIE*, vol. 3916, p. 19, 2000.

[18] R. O. Esenaliev, I. V. Larina, K. V. Larin, D. J. Deyo, M. Motamedi, and D. S. Prough, "Optoacoustic technique for noninvasive monitoring of blood oxygenation: a feasibility study," *Applied optics*, vol. 41, no. 22, pp. 4722–4731, 2002.

[19] M. Xu and L. V. Wang, "Time-domain reconstruction for thermoacoustic tomography in a spherical geometry," *IEEE transactions on medical imaging*, vol. 21, no. 7, pp. 814–822, 2002.

[20] X. Wang, G. Ku, M. A. Wegiel, D. J. Bornhop, G. Stoica, and L. V. Wang, "Noninvasive photoacoustic angiography of animal brains in vivo with near-infrared light and an optical contrast agent," *Optics letters*, vol. 29, no. 7, pp. 730–732, 2004.

[21] J. A. Copland, M. Eghtedari, V. L. Popov, N. Kotov, N. Mamedova, M. Motamedi, and A. A. Oraevsky, "Bioconjugated gold nanoparticles as a molecular based contrast agent: implications for imaging of deep tumors using optoacoustic tomography," *Molecular Imaging & Biology*, vol. 6, no. 5, pp. 341–349, 2004.

[22] K. H. Song, E. W. Stein, J. A. Margenthaler, and L. V. Wang, "Noninvasive photoacoustic identification of sentinel lymph nodes containing methylene blue in vivo in a rat model," *Journal of Biomedical Optics*, vol. 13, no. 5, pp. 054033–6, 2008.

[23] C. H. Li and L. H. V. Wang, "Photoacoustic tomography and sensing in biomedicine," *Physics in Medicine and Biology*, vol. 54, no. 19, pp. R59–R97, 2009.

[24] H. Wang, T. B. Huff, D. A. Zweifel, W. He, P. S. Low, A. Wei, and J. X. Cheng, "In vitro and in vivo two-photon luminescence imaging of single gold nanorods," *Proceedings of the National Academy of Sciences of the United States of America*, vol. 102, no. 44, p. 15752, 2005.

[25] K. Sokolov, M. Follen, J. Aaron, I. Pavlova, A. Malpica, R. Lotan, and R. Richards-Kortum, "Real-time vital optical imaging of precancer using anti-epidermal growth factor receptor antibodies conjugated to gold nanoparticles," *Cancer Research*, vol. 63, no. 9, p. 1999, 2003.

[26] L. R. Hirsch, J. B. Jackson, A. Lee, N. J. Halas, and J. L. West, "A whole blood immunoassay using gold nanoshells," *Analytical Chemistry*, vol. 75, no. 10, pp. 2377–2381, 2003.

[27] N. J. Durr, T. Larson, D. K. Smith, B. A. Korgel, K. Sokolov, and A. Ben-Yakar, "Two-photon luminescence imaging of cancer cells using molecularly targeted gold nanorods," *Nano Letters*, vol. 7, no. 4, pp. 941–945, 2007.

[28] L. Cognet, C. Tardin, D. Boyer, D. Choquet, P. Tamarat, and B. Lounis, "Single metallic nanoparticle imaging for protein detection in cells," *Proceedings of the National Academy of Sciences*, vol. 100, no. 20, p. 11350, 2003.

[29] M. L. Brongersma, "Nanoscale photonics: Nanoshells: gifts in a gold wrapper," *Nature materials*, vol. 2, no. 5, pp. 296–297, 2003.

[30] P. K. Jain, K. S. Lee, I. H. El-Sayed, and M. A. El-Sayed, "Calculated absorption and scattering properties of gold nanoparticles of different size, shape, and composition: applications in biological imaging and biomedicine," *Journal of Physical Chemistry B*, vol. 110, no. 14, pp. 7238–7248, 2006.

[31] Y. Wang, X. Xie, X. Wang, G. Ku, K. L. Gill, D. P. O'Neal, G. Stoica, and L. V. Wang, "Photoacoustic tomography of a nanoshell contrast agent in the in vivo rat brain," *Nano Letters*, vol. 4, no. 9, pp. 1689–1692, 2004.

[32] X. Yang, S. E. Skrabalak, Z.-Y. Li, Y. Xia, and L. V. Wang, "Photoacoustic tomography of a rat cerebral cortex in vivo with au nanocages as an optical contrast agent," *Nano Letters*, vol. 7, no. 12, pp. 3798–3802, 2007.

[33] G. Han, P. Ghosh, M. De, and V. Rotello, "Drug and gene delivery using gold nanoparticles," *NanoBioTechnology*, vol. 3, no. 1, pp. 40–45, 2007.

[34] X. Huang, P. Jain, I. El-Sayed, and M. El-Sayed, "Plasmonic photothermal therapy (pptt) using gold nanoparticles," *Lasers in Medical Science*, vol. 23, no. 3, pp. 217–228, 2008.

[35] G. von Maltzahn, J.-H. Park, A. Agrawal, N. K. Bandaru, S. K. Das, M. J. Sailor, and S. N. Bhatia, "Computationally guided photothermal tumor therapy using long-circulating gold nanorod antennas," *Cancer Res*, vol. 69, no. 9, pp. 3892–3900, 2009.

[36] A. Agarwal, S. W. Huang, M. O'Donnell, K. C. Day, M. Day, N. Kotov, and S. Ashkenazi, "Targeted gold nanorod contrast agent for prostate cancer detection by photoacoustic imaging," *Journal of Applied Physics*, vol. 102, no. 6, p. 064701, 2007.

[37] D. L. Chamberland, A. Agarwal, N. A. Kotov, J. B. Fowlkes, P. L. Carson, and X. Wang, "Photoacoustic tomography of joints aided by an Etanercept-conjugated gold nanoparticle contrast agent - an ex vivo preliminary rat study," *Nanotechnology*, vol. 19, no. 9, p. 095101, 2008.

[38] K. Kim, S.-W. Huang, S. Ashkenazi, M. O'Donnell, A. Agarwal, N. A. Kotov, M. F. Denny, and M. J. Kaplan, "Photoacoustic imaging of early inflammatory response using gold nanorods," *Applied Physics Letters*, vol. 90, no. 22, p. 223901, 2007.

[39] Z. Y. Tang and N. A. Kotov, "One-dimensional assemblies of nanoparticles: Preparation, properties, and promise," *Advanced Materials*, vol. 17, no. 8, pp. 951–962, 2005.

[40] S. Srivastava, A. Santos, K. Critchley, K. S. Kim, P. Podsiadlo, K. Sun, J. Lee, C. L. Xu, G. D. Lilly, S. C. Glotzer, and N. A. Kotov, "Light-controlled self-assembly of semiconductor nanoparticles into twisted ribbons," *Science*, vol. 327, no. 5971, pp. 1355–1359, 2010.

[41] Z. Y. Tang, N. A. Kotov, and M. Giersig, "Spontaneous organization of single cdte nanoparticles into luminescent nanowires," *Science*, vol. 297, no. 5579, pp. 237–240, 2002.

[42] Z. Y. Tang, Z. L. Zhang, Y. Wang, S. C. Glotzer, and N. A. Kotov, "Self-assembly of cdte nanocrystals into free-floating sheets," *Science*, vol. 314, no. 5797, pp. 274–278, 2006.

[43] H. Cory and A. Shtrom, "Wave propagation along a rectangular metallic waveguide longitudinally loaded with a metamaterial slab," *Microwave and Optical Technology Letters*, vol. 41, no. 2, pp. 123–127, 2004.

[44] N. Fang and X. Zhang, "Imaging properties of a metamaterial superlens," *Applied Physics Letters*, vol. 82, no. 2, pp. 161–163, 2003.

[45] J. B. Pendry and D. R. Smith, "The quest for the superlens," *Scientific American*, vol. 295, no. 1, pp. 60–67, 2006.

[46] M. J. Kaplan, "Cardiovascular disease in rheumatoid arthritis," *Current Opinion in Rheumatology*, vol. 18, no. 3, pp. 289–297, 2006.

[47] J. M. Esdaile, M. Abrahamowicz, T. Grodzicky, Y. Li, C. Panaritis, R. du Berger, R. Cote, S. A. Grover, P. R. Fortin, A. E. Clarke, and J. L. Senecal, "Traditional framingham risk factors fail to fully account for accelerated atherosclerosis in systemic lupus erythematosus," *Arthritis and Rheumatism*, vol. 44, no. 10, pp. 2331–2337, 2001.

[48] P. Libby, P. M. Ridker, and A. Maseri, "Inflammation and atherosclerosis," *Circulation*, vol. 105, no. 9, pp. 1135–1143, 2002.

[49] P. Libby, "Inflammation in atherosclerosis," *Nature*, vol. 420, no. 6917, pp. 868–874, 2002.

[50] P. A. Klimiuk, S. Sierakowski, R. Latosiewicz, J. P. Cylwik, B. Cylwik, J. Skowronski, and J. Chwiecko, "Soluble adhesion molecules (icam-1, vcam-1, and e-selectin) and vascular endothelial growth factor (vegf) in patients with distinct variants of rheumatoid synovitis," *Annals of the Rheumatic Diseases*, vol. 61, no. 9, pp. 804–809, 2002.

[51] V. E. Gusev and A. A. Karabutov, *Laser optoacoustics*. New York: American Institute of Physics, 1993.

[52] P. C. Li, C. W. Wei, C. K. Liao, C. D. Chen, K. C. Pao, C. R. C. Wang, Y. N. Wu, and D. B. Shieh, "Multiple targeting in photoacoustic imaging using bioconjugated gold nanorods - art. no. 60860m," *Photons Plus Ultrasound: Imaging and Sensing 2006*, vol. 6086, pp. M860–M860 530, 2006.

[53] A. Conjusteau, S. A. Ermilov, D. Lapotko, H. Liao, J. Hafner, M. Eghtedari, M. Motamedi, N. Kotov, and A. A. Oraevsky, "Metallic nanoparticles as optoacoustic contrast agents for medical imaging - art. no. 60860k," *Photons Plus Ultrasound: Imaging and Sensing 2006*, vol. 6086, pp. K860–K860 530, 2006.

[54] L. M. LizMarzan, M. Giersig, and P. Mulvaney, "Synthesis of nanosized gold-silica core-shell particles," *Langmuir*, vol. 12, no. 18, pp. 4329–4335, 1996.

[55] E. M. Shevach, S. O. Sharrow, K. L. Holmes, B. J. Fowlkes, I. Schmid, J. V. Giorgi, G. Otten, W. M. Yokoyama, C. H. June, and R. Abe, "Immunofluorescence and cell sorting," *Current Protocols in Immunology*, 1992.

[56] J. Doukas and J. S. Pober, "Ifn-gamma enhances endothelial activation induced by tumor-necrosis-factor but not il-1," *Journal of Immunology*, vol. 145, no. 6, pp. 1727–1733, 1990.

[57] B. Nikoobakht and M. A. El-Sayed, "Preparation and growth mechanism of gold nanorods (NRs) using seed-mediated growth method," *Chemistry of Materials*, vol. 15, no. 10, pp. 1957–1962, 2003.

[58] C. J. Murphy and N. R. Jana, "Controlling the aspect ratio of inorganic nanorods and nanowires," *Advanced Materials*, vol. 14, no. 1, p. 80, 2002.

[59] A. Gole and C. J. Murphy, "Biotin-streptavidin-induced aggregation of gold nanorods: Tuning rod-rod orientation," *Langmuir*, vol. 21, no. 23, pp. 10756–10762, 2005.

[60] J. Lee, A. O. Govorov, J. Dulka, and N. A. Kotov, "Bioconjugates of CdTe nanowires and au nanoparticles: Plasmon- exciton interactions, luminescence enhancement, and collective effects," *Nano Letters*, vol. 4, no. 12, pp. 2323–2330, 2004.

[61] N. N. Mamedova, N. A. Kotov, A. L. Rogach, and J. Studer, "Albumin-CdTe nanoparticle bioconjugates: preparation, structure, and interunit energy transfer with antenna effect," *Nano Letters*, vol. 1, no. 6, pp. 281–286, 2001.

[62] S. Wang, N. Mamedova, N. A. Kotov, W. Chen, and J. Studer, "Antigen/antibody immunocomplex from CdTe nanoparticle bioconjugates," *Nano Letters*, vol. 2, no. 8, pp. 817–822, 2002.

[63] S. Wray, M. Cope, D. T. Delpy, J. S. Wyatt, and E. O. Reynolds, "Characterization of the near infrared absorption spectra of cytochrome aa3 and haemoglobin for the non-invasive monitoring of cerebral oxygenation," *Biochim Biophys Acta*, vol. 933, no. 1, pp. 184–92, 1988.

[64] B. B. Aggarwal, S. Shishodia, K. Ashikawa, and A. C. Bharti, "The role of TNF and its family members in inflammation and cancer: lessons from gene deletion," *Current Drug Targets-Inflammation & Allergy*, vol. 1, no. 4, pp. 327–341, 2002.

[65] G. Steiner, M. Tohidast-Akrad, G. Witzmann, M. Vesely, A. Studnicka-Benke, A. Gal, M. Kunaver, P. Zenz, and J. S. Smolen, "Cytokine production by synovial t cells in rheumatoid arthritis," *Rheumatology*, vol. 38, no. 3, p. 202, 1999.

[66] P. Efthimiou and J. A. Markenson, "Role of biological agents in immune-mediated inflammatory diseases," *Southern Medical Journal*, vol. 98, no. 2, p. 192, 2005.

[67] J. C. Fernandes, J. Martel-Pelletier, and J. P. Pelletier, "The role of cytokines in osteoarthritis pathophysiology," *Biorheology*, vol. 39, no. 1, pp. 237–246, 2002.

[68] A. P. Cope, D. Gibbons, F. M. Brennan, M. Feldmann, D. Aderka, M. Doherty, A. C. Jones, H. Engelmann, D. Wallach, and R. N. Maini, "Increased levels of soluble tumor necrosis factor receptors in the sera and synovial fluid of patients with rheumatic diseases," *Arthritis & Rheumatism*, vol. 35, no. 10, pp. 1160–1169, 2008.

[69] P. Barrera, W. J. G. Oyen, O. C. Boerman, and P. van Riel, "Scintigraphic detection of tumour necrosis factor in patients with rheumatoid arthritis," *Annals of the Rheumatic Diseases*, vol. 62, no. 9, p. 825, 2003.

[70] P. Barrera, "Effects of treatment with a fully human anti-tumour necrosis factor monoclonal antibody on the local and systemic homeostasis of interleukin 1 and TNF in patients with rheumatoid arthritis," *Annals of the Rheumatic Diseases*, vol. 60, no. 7, p. 660, 2001.

[71] X. Wang, D. L. Chamberland, P. L. Carson, J. B. Fowlkes, R. O. Bude, D. A. Jamadar, and B. J. Roessler, "Imaging of joints with laser-based photoacoustic tomography: an animal study," *Medical Physics*, vol. 33, p. 2691, 2006.

[72] M. Xu and L. V. Wang, "Universal back-projection algorithm for photoacoustic computed tomography," *Physical Review E*, vol. 71, no. 1, p. 16706, 2005.

[73] X. Wang, Y. Xu, M. Xu, S. Yokoo, E. S. Fry, and L. V. Wang, "Photoacoustic tomography of biological tissues with high cross-section resolution: Reconstruction and experiment," *Medical Physics*, vol. 29, p. 2799, 2002.

[74] R. Weissleder, "A clearer vision for in vivo imaging," *Nature Biotechnology*, vol. 19, no. 4, pp. 316–316, 2001.

[75] A. Gole and C. J. Murphy, "Biotin-streptavidin-induced aggregation of gold nanorods: Tuning rod-rod orientation," *Langmuir*, vol. 21, no. 23, pp. 10756–10762, 2005.

[76] I. H. El-Sayed, X. Huang, and M. A. El-Sayed, "Surface plasmon resonance scattering and absorption of anti-egfr antibody conjugated gold nanoparticles in cancer diagnostics: applications in oral cancer," *Nano Lett*, vol. 5, no. 5, pp. 829–834, 2005.

[77] P. H. Wooley, "The usefulness and the limitations of animal models in identifying targets for therapy in arthritis," *Best Practice & Research Clinical Rheumatology*, vol. 18, pp. 47–58, 2004.

[78] R. E. Hammer, S. D. Maika, J. A. Richardson, J. P. Tang, and J. D. Taurog, "Spontaneous inflammatory disease in transgenic rats expressing HLA-B27 and human [beta] 2m: An animal model of HLA-B27-associated human disorders," *Cell*, vol. 63, no. 5, pp. 1099–1112, 1990.

[79] M. Breban, R. E. Hammer, J. A. Richardson, and J. D. Taurog, "Transfer of the inflammatory disease of HLA-B27 transgenic rats by bone marrow engraftment," *Journal of Experimental Medicine*, vol. 178, no. 5, p. 1607, 1993.

[80] A. L. Oldenburg, M. N. Hansen, D. A. Zweifel, A. Wei, and S. A. Boppart, "Plasmon-resonant gold nanorods as low backscattering albedo contrast agents for optical coherence tomography," *Optics Express*, vol. 14, no. 15, pp. 6724–6738, 2006.

[81] C. Loo, A. Lowery, N. Halas, J. West, and R. Drezek, "Immunotargeted nanoshells for integrated cancer imaging and therapy," *Nano Letters*, vol. 5, no. 4, pp. 709–711, 2005.

[82] A. Cski, P. Kaplanek, R. Mller, and W. Fritzsche, "The optical detection of individual DNA-conjugated gold nanoparticle labels after metal enhancement," *Nanotechnology*, vol. 14, pp. 1262–1268, 2003.

[83] E. Boisselier and D. Astruc, "Gold nanoparticles in nanomedicine: preparations, imaging, diagnostics, therapies and toxicity," *Chemical Society Reviews*, vol. 38, no. 6, pp. 1759–1782, 2009.

[84] I. Brigger, C. Dubernet, and P. Couvreur, "Nanoparticles in cancer therapy and diagnosis," *Advanced Drug Delivery Reviews*, vol. 54, no. 5, pp. 631–651, 2002.

[85] A. M. Morawski, P. M. Winter, K. C. Crowder, S. D. Caruthers, R. W. Fuhrhop, M. J. Scott, J. D. Robertson, D. R. Abendschein, G. M. Lanza, and S. A. Wickline, "Targeted nanoparticles for quantitative imaging of sparse molecular epitopes with mri," *Magnetic Resonance in Medicine*, vol. 51, no. 3, pp. 480–486, 2004.

[86] S. K. Sahoo and V. Labhasetwar, "Nanotech approaches to drug delivery and imaging," *Drug discovery today*, vol. 8, no. 24, pp. 1112–1120, 2003.

[87] M. V. Yezhelyev, X. Gao, Y. Xing, A. Al-Hajj, S. Nie, and R. M. O'Regan, "Emerging use of nanoparticles in diagnosis and treatment of breast cancer," *The lancet oncology*, vol. 7, no. 8, pp. 657–667, 2006.

[88] S. R. Cherry, "In vivo molecular and genomic imaging: new challenges for imaging physics," *Physics in Medicine and Biology*, vol. 49, no. 3, pp. 13–49, 2004.

[89] M. C. Pierce, D. J. Javier, and R. Richards-Kortum, "Optical contrast agents and imaging systems for detection and diagnosis of cancer," *Int. J. Cancer*, vol. 123, no. 9, pp. 1979–1990, 2008.

[90] E. Carbo-Argibay, B. Rodriguez-Gonzalez, J. Pacifico, I. Pastoriza-Santos, J. Perez-Juste, and L. M. Liz-Marzan, "Chemical sharpening of gold nanorods: The rod-to-octahedron transition," *Angewandte Chemie-International Edition*, vol. 46, no. 47, pp. 8983–8987, 2007.

[91] J. Perez-Juste, I. Pastoriza-Santos, L. M. Liz-Marzan, and P. Mulvaney, "Gold nanorods: synthesis, characterization and applications," *Coordination Chemistry Reviews*, vol. 249, no. 17-18, pp. 1870–1901, 2005.

[92] J. X. Gao, C. M. Bender, and C. J. Murphy, "Dependence of the gold nanorod aspect ratio on the nature of the directing surfactant in aqueous solution," *Langmuir*, vol. 19, no. 21, pp. 9065–9070, 2003.

[93] R. Popovtzer, A. Agarwal, N. A. Kotov, A. Popovtzer, J. Balter, T. E. Carey, and R. Kopelman, "Targeted Gold Nanoparticles Enable Molecular CT Imaging of Cancer," *Nano Letters*, vol. 8, no. 12, pp. 4593–4596, 2008.

[94] M. Grzelczak, A. Sanchez-Iglesias, B. Rodriguez-Gonzalez, R. Alvarez-Puebla, J. Perez-Juste, and L. M. Liz-Marzan, "Influence of iodide ions on the growth of gold nanorods: Tuning tip curvature and surface plasmon resonance," *Advanced Functional Materials*, vol. 18, no. 23, pp. 3780–3786, 2008.

[95] K. Maslov, G. Ku, and L. V. Wang, "Photoacoustic microscopy with submicron resolution," vol. 7564, (San Francisco, California, USA), SPIE, 2010.

[96] H. F. Zhang, K. Maslov, G. Stoica, and L. H. V. Wang, "Functional photoacoustic microscopy for high-resolution and noninvasive in vivo imaging," *Nature Biotechnology*, vol. 24, no. 7, pp. 848–851, 2006.

[97] R. Kannan, V. Rahing, C. Cutler, R. Pandrapragada, K. K. Katti, V. Kattumuri, J. D. Robertson, S. J. Casteel, S. Jurisson, and C. Smith, "Nanocompatible chemistry toward fabrication of target-specific gold nanoparticles," *J. Am. Chem. Soc*, vol. 128, no. 35, pp. 11342–11343, 2006.

[98] K. V. Katti, R. Kannan, K. Katti, V. Kattumori, R. Pandrapraganda, V. Rahing, C. Cutler, E. J. Boote, S. W. Casteel, and C. J. Smith, "Hybrid gold nanoparticles in molecular imaging and radiotherapy," *Czechoslovak Journal of Physics*, vol. 56, no. 1, pp. 23–34, 2006.

[99] C. Nripen, K. Para, D. W. Lisa, S. Ravi, Z. Ajit, L. C. Terry, E. Hendrik, R. L. John, K. Kavita, M. F. Genevieve, W. C. Stan, C. J. Smith, H. M. William, J. Silvia, B. Evan, J. D. Robertson, C. Cathy, D. Marina, K. Raghuraman, and V. K. Kattesh, "Radioactive gold nanoparticles in cancer therapy: therapeutic efficacy studies of ga-198aunp nanoconstruct in prostate tumorbearing mice," *Nanomedicine*, vol. 6, no. 2, pp. 201–209, 2010.

[100] K. Roy and S. Lahiri, "A green method for synthesis of radioactive gold nanoparticles," *Green Chemistry*, vol. 8, no. 12, pp. 1063–1066, 2006.

[101] M. D. Chavanpatil, A. Khdair, and J. Panyam, "Nanoparticles for cellular drug delivery: mechanisms and factors influencing delivery," *J Nanosci Nanotechnol*, vol. 6, no. 9-10, pp. 2651–63, 2006.

[102] K. Petrak, "Nanotechnology and site-targeted drug delivery," *J Biomater Sci Polym Ed*, vol. 17, no. 11, pp. 1209–1219, 2006.

[103] M. Rawat, D. Singh, and S. Saraf, "Nanocarriers: promising vehicle for bioactive drugs," *Biol Pharm Bull*, vol. 29, no. 9, pp. 1790–1798, 2006.

[104] J. Bruchez, M., M. Moronne, P. Gin, S. Weiss, and A. P. Alivisatos, "Semiconductor nanocrystals as fluorescent biological labels," *Science*, vol. 281, no. 5385, pp. 2013–6, 1998.

[105] W. C. Chan and S. Nie, "Quantum dot bioconjugates for ultrasensitive nonisotopic detection," *Science*, vol. 281, no. 5385, pp. 2016–2018, 1998.

[106] S. Santra, D. Dutta, G. A. Walter, and B. M. Moudgil, "Fluorescent nanoparticle probes for cancer imaging," *Technol Cancer Res Treat*, vol. 4, no. 6, pp. 593–602, 2005.

[107] I. Brigger, C. Dubernet, and P. Couvreur, "Nanoparticles in cancer therapy and diagnosis," *Adv Drug Deliv Rev*, vol. 54, no. 5, pp. 631–51, 2002.

[108] B. A. Holm, E. J. Bergey, T. De, D. J. Rodman, R. Kapoor, L. Levy, C. S. Friend, and P. N. Prasad, "Nanotechnology in biomedical applications," *Molecular Crystals and Liquid Crystals*, vol. 374, pp. 589 – 598, 2002.

[109] K. K. Jain, "Nanotechnology in clinical laboratory diagnostics," *Clin Chim Acta*, vol. 358, no. 1-2, pp. 37–54, 2005.

[110] S. M. Moghimi, A. C. Hunter, and J. C. Murray, "Nanomedicine: current status and future prospects," *FASEB J*, vol. 19, no. 3, pp. 311–30, 2005.

[111] A. K. Oyelere, P. C. Chen, X. Huang, I. H. El-Sayed, and M. A. El-Sayed, "Peptide-conjugated gold nanorods for nuclear targeting," *Bioconjug Chem*, vol. 18, no. 5, pp. 1490–7, 2007.

[112] J. Z. Zhang, "Biomedical applications of shape-controlled plasmonic nanostructures: A case study of hollow gold nanospheres for photothermal ablation therapy of cancer," *The Journal of Physical Chemistry Letters*, vol. 1, no. 4, pp. 686–695, 2010.

[113] M. A. El-Sayed, "Some interesting properties of metals confined in time and nanometer space of different shapes," *Accounts of Chemical Research*, vol. 34, no. 4, pp. 257–264, 2001.

[114] K. L. Kelly, E. Coronado, L. L. Zhao, and G. C. Schatz, "The optical properties of metal nanoparticles: The influence of size, shape, and dielectric environment," *Journal of Physical Chemistry B*, vol. 107, no. 3, pp. 668–677, 2003.

[115] C. Noguez, "Surface plasmons on metal nanoparticles: The influence of shpae and physical environment," *Journal of Physical Chemistry C*, vol. 111, no. 10, pp. 3806–3819, 2007.

[116] Y. G. Sun and Y. N. Xia, "Increased sensitivity of surface plasmon resonance of gold nanoshells compared to that of gold solid colloids in response to environmental changes," *Analytical Chemistry*, vol. 74, no. 20, pp. 5297–5305, 2002.

[117] L. Tong, Q. S. Wei, A. Wei, and J. X. Cheng, "Gold nanorods as contrast agents for biological imaging: Optical properties, surface conjugation and photothermal effects," *Photochemistry and Photobiology*, vol. 85, no. 1, pp. 21–32, 2009.

[118] C. H. Chou, C. D. Chen, and C. R. C. Wang, "Highly efficient, wavelength-tunable, gold nanoparticle based optothermal nanoconvertors," *Journal of Physical Chemistry B*, vol. 109, no. 22, pp. 11135–11138, 2005.

[119] L. Hirsch, R. Stafford, J. Bankson, S. Sershen, B. Rivera, R. Price, J. Hazle, N. Halas, and J. West, "Nanoshell-mediated near-infrared thermal therapy of tumors under magnetic resonance guidance," *Proceedings of the National Academy of Sciences*, vol. 100, no. 23, p. 13549, 2003.

[120] D. P. O'Neal, L. R. Hirsch, N. J. Halas, J. D. Payne, and J. L. West, "Photothermal tumor ablation in mice using near infrared-absorbing nanoparticles," *Cancer Letters*, vol. 209, no. 2, pp. 171–176, 2004.

[121] H. Petrova, J. P. Juste, I. Pastoriza-Santos, G. V. Hartland, L. M. Liz-Marzan, and P. Mulvaney, "On the temperature stability of gold nanorods: comparison between thermal and ultrafast laser-induced heating," *Physical Chemistry Chemical Physics*, vol. 8, no. 7, pp. 814–821, 2006.

[122] P. Wust, B. Hildebrandt, G. Sreenivasa, B. Rau, J. Gellermann, H. Riess, R. Felix, and P. M. Schlag, "Hyperthermia in combined treatment of cancer," *Lancet Oncology*, vol. 3, no. 8, pp. 487–497, 2002.

[123] J. Y. Chen, D. L. Wang, J. F. Xi, L. Au, A. Siekkinen, A. Warsen, Z. Y. Li, H. Zhang, Y. N. Xia, and X. D. Li, "Immuno gold nanocages with tailored optical properties for targeted photothermal destruction of cancer cells," *Nano Letters*, vol. 7, no. 5, pp. 1318–1322, 2007.

[124] T. B. Huff, L. Tong, Y. Zhao, M. N. Hansen, J. X. Cheng, and A. Wei, "Hyperthermic effects of gold nanorods on tumor cells," *Nanomedicine*, vol. 2, no. 1, pp. 125–132, 2007.

[125] L. Tong, Y. Zhao, T. B. Huff, M. N. Hansen, A. Wei, and J. X. Cheng, "Gold nanorods mediate tumor cell death by compromising membrane integrity," *Advanced Materials*, vol. 19, no. 20, pp. 3136–3141, 2007.

[126] T. Niidome, Y. Akiyama, K. Shimoda, T. Kawano, T. Mori, Y. Katayama, and Y. Niidome, "In vivo monitoring of intravenously injected gold nanorods using near-infrared light," *Small*, vol. 4, no. 7, pp. 1001–1007, 2008.

[127] C. Sonnichsen, T. Franzl, T. Wilk, G. von Plessen, J. Feldmann, O. Wilson, and P. Mulvaney, "Drastic reduction of plasmon damping in gold nanorods," *Physical Review Letters*, vol. 88, no. 7, p. 077402, 2002.

[128] K. Imura, T. Nagahara, and H. Okamoto, "Near-field two-photon-induced photoluminescence from single gold nanorods and imaging of plasmon modes," *Journal of Physical Chemistry B*, vol. 109, no. 27, pp. 13214–13220, 2005.

[129] M. Pelton, M. Z. Liu, H. Y. Kim, G. Smith, P. Guyot-Sionnest, and N. E. Scherer, "Optical trapping and alignment of single gold nanorods by using plasmon resonances," *Optics Letters*, vol. 31, no. 13, pp. 2075–2077, 2006.

[130] H. W. Liao and J. H. Hafner, "Gold nanorod bioconjugates," *Chemistry of Materials*, vol. 17, no. 18, pp. 4636–4641, 2005.

[131] T. Niidome, M. Yamagata, Y. Okamoto, Y. Akiyama, H. Takahashi, T. Kawano, Y. Katayama, and Y. Niidome, "Peg-modified gold nanorods with a stealth character for in vivo applications," *Journal of Controlled Release*, vol. 114, no. 3, pp. 343–347, 2006.

[132] M. Eghtedari, A. V. Liopo, J. A. Copland, A. A. Oraevslty, and M. Motamedi, "Engineering of hetero-functional gold nanorods for the in vivo molecular targeting of breast cancer cells," *Nano Letters*, vol. 9, no. 1, pp. 287–291, 2009.

[133] C. G. Wang, J. Chen, T. Talavage, and J. Irudayaraj, "Gold nanorod/fe3o4 nanoparticle "nano-pearl-necklaces" for simultaneous targeting, dual-mode imaging, and photothermal ablation of cancer cells," *Angewandte Chemie-International Edition*, vol. 48, no. 15, pp. 2759–2763, 2009.

[134] L. L. Rouhana, J. A. Jaber, and J. B. Schlenoff, "Aggregation-resistant water-soluble gold nanoparticles," *Langmuir*, vol. 23, no. 26, pp. 12799–12801, 2007.

[135] C. Fang, B. Shi, Y. Y. Pei, M. H. Hong, J. Wu, and H. Z. Chen, "In vivo tumor targeting of tumor necrosis factor-alpha-loaded stealth nanoparticles: Effect of mepeg molecular weight and particle size," *European Journal of Pharmaceutical Sciences*, vol. 27, no. 1, pp. 27–36, 2006.

[136] D. E. Owens and N. A. Peppas, "Opsonization, biodistribution, and pharmacokinetics of polymeric nanoparticles," *International Journal of Pharmaceutics*, vol. 307, no. 1, pp. 93–102, 2006.

[137] X. K. Sun, R. Rossin, J. L. Turner, M. L. Becker, M. J. Joralemon, M. J. Welch, and K. L. Wooley, "An assessment of the effects of shell cross-linked nanoparticle size, core composition, and surface pegylation on in vivo biodistribution," *Biomacromolecules*, vol. 6, no. 5, pp. 2541–2554, 2005.

[138] J. F. Hainfeld, D. N. Slatkin, T. M. Focella, and H. M. Smilowitz, "Gold nanoparticles: a new x-ray contrast agent," *British Journal of Radiology*, vol. 79, no. 939, pp. 248–253, 2006.

[139] D. K. Smith, N. R. Miller, and B. A. Korgel, "Iodide in ctab prevents gold nanorod formation," *Langmuir*, vol. 25, no. 16, pp. 9518–9524, 2009.

[140] G. Storm, S. O. Belliot, T. Daemen, and D. D. Lasic, "Surface modification of nanoparticles to oppose uptake by the mononuclear phagocyte system," *Advanced Drug Delivery Reviews*, vol. 17, no. 1, pp. 31–48, 1995.

[141] S. E. Dunn, A. Brindley, S. S. Davis, M. C. Davies, and L. Illum, "Polystyrene-poly(ethylene glycol) (ps-peg2000) particles as model systems for site-specific drug-delivery .2. the effect of peg surface-density on the in-vitro cell-interaction and in-vivo biodistribution," *Pharmaceutical Research*, vol. 11, no. 7, pp. 1016–1022, 1994.

[142] H. Rusinek, D. P. Naidich, G. McGuinness, B. S. Leitman, D. I. McCauley, G. A. Krinsky, K. Clayton, and H. Cohen, "Pulmonary nodule detection: Low-dose versus conventional CT," *Radiology*, vol. 209, no. 1, pp. 243–249, 1998.

[143] C. Nanni, D. Rubello, S. Fanti, M. Farsad, V. Ambrosini, L. Rampin, A. Banti, E.and Carpi, P. Muzzio, and R. Franchi, "Role of 18F-FDG-PET and PET/CT imaging in thyroid cancer," *Biomedicine & Pharmacotherapy*, vol. 60, no. 8, pp. 409–413, 2006.

[144] A. Al-Nahhas, Z. Win, T. Szyszko, A. Singh, C. Nanni, S. Fanti, and D. Rubello, "Gallium-68 PET: A new frontier in receptor cancer imaging," *Anticancer Research*, vol. 27, no. 6B, pp. 4087–4094, 2007.

[145] C. Sun, O. Veiseh, J. Gunn, C. Fang, S. Hansen, D. Lee, R. Sze, R. G. Ellenbogen, J. Olson, and M. Zhang, "In vivo MRI detection of gliomas by chlorotoxin-conjugated superparamagnetic nanoprobes," *Small*, vol. 4, no. 3, pp. 372–379, 2008.

[146] R. Lamerichs, "MRI-based molecular imaging using nano-particles," *Cellular Oncology*, vol. 30, no. 2, p. 100, 2008.

[147] R. Kopelman, Y.-E. L. Koo, M. Philbert, B. A. Moffat, G. R. Reddy, P. McConville, D. E. Hall, T. L. Chenevert, M. S. Bhojani, S. M. Buck, A. Rehemtulla, and B. D. Ross, "Multifunctional nanoparticle platforms for in vivo MRI enhancement and photodynamic therapy of a rat brain cancer," *Journal of Magnetism and Magnetic Materials*, vol. 293, no. 1, Sp. Iss. SI, pp. 404–410, 2005.

[148] Y.-E. L. Koo, R. G. Reddy, M. Bhojani, R. Schneider, M. A. Philbert, A. Rehemtulla, B. D. Ross, and R. Kopelman, "Brain cancer diagnosis and therapy with nanoplatforms," *Advanced Drug Delivery Reviews*, vol. 58, no. 14, pp. 1556–1577, 2006.

[149] Y. Guo, D. Shi, J. Lian, Z. Dong, W. Wang, H. Cho, G. Liu, L. Wang, and R. C. Ewing, "Quantum dot conjugated hydroxylapatite nanoparticles for in vivo imaging," *Nanotechnology*, vol. 19, no. 17, 2008.

[150] X. H. Gao and S. M. Nie, "Long-circulating QD probes for in-vivo tumor imaging," in *Nanosensing:Materials and Devices*, vol. 5593, pp. 292–299, 2004.

[151] P. Diagaradjane, J. M. Orenstein-Cardona, N. E. Colon-Casasnovas, A. Deorukhkar, S. Shentu, N. Kuno, D. L. Schwartz, J. G. Gelovani, and S. Krishnan, "Imaging epidermal growth factor receptor expression in vivo: Pharmacokinetic and biodistribution characterization of a bioconjugated quantum dot nanoprobe," *Clinical Cancer Research*, vol. 14, no. 3, pp. 731–741, 2008.

[152] P. K. Jain, I. H. El-Sayed, and M. A. El-Sayed, "Au nanoparticles target cancer," *Nano Today*, vol. 2, no. 1, pp. 18–29, 2007.

[153] X. Huang, P. K. Jain, I. H. El-Sayed, and M. A. El-Sayed, "Gold nanoparticles: interesting optical properties and recent applications in cancer diagnostic and therapy," *Nanomedicine*, vol. 2, no. 5, pp. 681–693, 2007.

[154] X. H. Huang, I. H. El-Sayed, W. Qian, and M. A. El-Sayed, "Cancer cell imaging and photothermal therapy in the near-infrared region by using gold nanorods," *Journal of the American Chemical Society*, vol. 128, no. 6, pp. 2115–2120, 2006.

[155] T. S. Hauck, A. A. Ghazani, and W. C. W. Chan, "Assessing the effect of surface chemistry on gold nanorod uptake, toxicity, and gene expression in mammalian cells," *Small*, vol. 4, no. 1, pp. 153–159, 2008.

[156] E. E. Connor, J. Mwamuka, A. Gole, C. J. Murphy, and M. D. Wyatt, "Gold nanoparticles are taken up by human cells but do not cause acute cytotoxicity," *Small*, vol. 1, no. 3, pp. 325–327, 2005.

[157] J. F. Hainfeld, D. N. Slatkin, T. M. Focella, and H. M. Smilowitz, "Gold nanoparticles: a new X-ray contrast agent," *British Journal of Radiology*, vol. 79, no. 939, pp. 248–253, 2006.

[158] D. Kim, S. Park, J. H. Lee, Y. Y. Jeong, and S. Jon, "Antibiofouling polymer-coated gold nanoparticles as a contrast agent for in vivo x-ray computed tomography imaging," *Journal of the American Chemical Society*, vol. 129, no. 24, pp. 7661–7665, 2007.

[159] V. Kattumuri, K. Katti, S. Bhaskaran, E. J. Boote, S. W. Casteel, G. M. Fent, D. J. Robertson, M. Chandrasekhar, R. Kannan, and K. V. Katti, "Gum arabic as a phytochemical construct for the stabilization of gold nanoparticles: In vivo pharmacokinetics and X-ray-contrast-imaging studies," *Small*, vol. 3, no. 2, pp. 333–341, 2007.

[160] C. Alric, J. Taleb, G. Le Duc, C. Mandon, C. Billotey, A. Le Meur-Herland, T. Brochard, F. Vocanson, M. Janier, P. Perriat, S. Roux, and O. Tillement, "Gadolinium chelate coated gold nanoparticles as contrast agents for both X-ray computed tomography and magnetic resonance imaging," *Journal of the American Chemical Society*, vol. 130, no. 18, pp. 5908–5915, 2008.

[161] Q.-Y. Cai, S. H. Kim, K. S. Choi, S. Y. Kim, S. J. Byun, K. W. Kim, S. H. Park, S. K. Juhng, and K. H. Yoon, "Colloidal gold nanoparticles as a blood-pool contrast agent for x-ray computed tomography in mice," *Investigative Radiology*, vol. 42, no. 12, pp. 797–806, 2007.

[162] O. Rabin, J. M. Perez, J. Grimm, G. Wojtkiewicz, and R. Weissleder, "An X-ray computed tomography imaging agent based on long-circulating bismuth sulphide nanoparticles," *Nature Materials*, vol. 5, no. 2, pp. 118–122, 2006.

[163] D. Chin, G. M. Boyle, S. Porceddu, D. R. Theile, P. G. Parsons, and W. B. Coman, "Head and neck cancer: past, present and future," *Expert Review of Anticancer Therapy*, vol. 6, no. 7, pp. 1111–1118, 2006.

[164] A. L. Carvalho, I. N. Nishimoto, J. A. Califano, and L. P. Kowalski, "Trends in incidence and prognosis for head and neck cancer in the United States: A site-specific analysis of the SEER database," *International Journal of Cancer*, vol. 114, no. 5, pp. 806–816, 2005.

[165] K. A. Kimmel and T. E. Carey, "Altered expression in squamous carcinoma cells of an orientation restricted epithelial antigen detected by monoclonal antibody A9," *Cancer Research*, vol. 46, no. 7, pp. 3614–3623, 1986.

[166] C. Van Waes, K. F. Kozarsky, A. B. Warren, L. Kidd, D. Paugh, M. Liebert, and T. E. Carey, "The a9 antigen associated with aggressive human squamous carcinoma is structurally and functionally similar to the newly defined integrin alpha 6 beta 4," *Cancer Research*, vol. 51, no. 9, pp. 2395–2402, 1991.

[167] G. T. Wolf, T. E. Carey, S. P. Schmaltz, K. D. McClatchey, J. Poore, L. GLaser, D. J. S. Hayashida, and S. Hsu, "Altered antigen expression predicts outcome in squamous cell carcinoma of the head and neck," *Journal of the National Cancer Institute*, vol. 82, no. 19, pp. 1566–1572, 1990.

[168] R. L. Wahl, K. A. Kimmel, W. H. Beierwaltes, and T. E. Carey, "Radioimmunodiagnosis of human-derived squamous cell carcinoma," *Hybridoma*, vol. 6, no. 2, pp. 111–119, 1987.

[169] A. M. Gobin, M. H. Lee, N. J. Halas, W. D. James, R. A. Drezek, and J. L. West, "Near-infrared resonant nanoshells for combined optical imaging and photothermal cancer therapy," *Nano Letters*, vol. 7, no. 7, pp. 1929–1934, 2007.

[170] M. Yoshida, K. H. Roh, and J. Lahann, "Short-term biocompatibility of biphasic nanocolloids with potential use as anisotropic imaging probes," *Biomaterials*, vol. 28, no. 15, pp. 2446–2456, 2007.

[171] V. G. Veselago, "Electrodynamics of substances with simultaneously negative values of sigma and mu," *Soviet Physics Uspekhi-Ussr*, vol. 10, no. 4, pp. 509–514, 1968.

[172] H. J. Lezec, J. A. Dionne, and H. A. Atwater, "Negative refraction at visible frequencies," *Science*, vol. 316, no. 5823, pp. 430–432, 2007.

[173] I. I. Smolyaninov, Y. J. Hung, and C. C. Davis, "Magnifying superlens in the visible frequency range," *Science*, vol. 315, no. 5819, pp. 1699–1701, 2007.

[174] T. Taubner, D. Korobkin, Y. Urzhumov, G. Shvets, and R. Hillenbrand, "Near-field microscopy through a sic superlens," *Science*, vol. 313, no. 5793, pp. 1595–1595, 2006.

[175] V. M. Shalaev, W. S. Cai, U. K. Chettiar, H. K. Yuan, A. K. Sarychev, V. P. Drachev, and A. V. Kildishev, "Negative index of refraction in optical metamaterials," *Optics Letters*, vol. 30, no. 24, pp. 3356–3358, 2005.

[176] R. A. Shelby, D. R. Smith, and S. Schultz, "Experimental verification of a negative index of refraction," *Science*, vol. 292, no. 5514, pp. 77–79, 2001.

[177] J. F. Zhou, L. Zhang, G. Tuttle, T. Koschny, and C. M. Soukoulis, "Negative index materials using simple short wire pairs," *Physical Review B*, vol. 73, no. 4, p. 041101, 2006.

[178] S. Zhang, W. J. Fan, K. J. Malloy, S. R. J. Brueck, N. C. Panoiu, and R. O. Osgood, "Demonstration of metal-dielectric negative-index metamaterials with improved performance at optical frequencies," *Journal of the Optical Society of America B-Optical Physics*, vol. 23, no. 3, pp. 434–438, 2006.

[179] E. V. Ponizovskaya and A. M. Bratkovsky, "Metallic negative index nanostructures at optical frequencies: losses and effect of gain medium," *Applied Physics a-Materials Science & Processing*, vol. 87, no. 2, pp. 161–165, 2007.

[180] V. A. Podolskiy, L. V. Alekseyev, and E. E. Narimanov, "Strongly anisotropic media: the thz perspectives of left-handed materials," *Journal of Modern Optics*, vol. 52, no. 16, pp. 2343–2349, 2005.

[181] S. A. Ramakrishna and J. B. Pendry, "Removal of absorption and increase in resolution in a near-field lens via optical gain," *Physical Review B*, vol. 67, no. 20, p. 201101, 2003.

[182] E. Shamonina, V. A. Kalinin, K. H. Ringhofer, and L. Solymar, "Imaging, compression and poynting vector streamlines for negative permittivity materials," *Electronics Letters*, vol. 37, no. 20, pp. 1243–1244, 2001.

[183] M. A. Noginov, G. Zhu, M. Bahoura, J. Adegoke, C. E. Small, B. A. Ritzo, V. P. Drachev, and V. M. Shalaev, "Enhancement of surface plasmons in an ag aggregate by optical gain in a dielectric medium," *Optics Letters*, vol. 31, no. 20, pp. 3022–3024, 2006.

[184] N. Gaponik, D. V. Talapin, A. L. Rogach, K. Hoppe, E. V. Shevchenko, A. Kornowski, A. Eychmuller, and H. Weller, "Thiol-capping of cdte nanocrystals: An alternative to organometallic synthetic routes," *Journal of Physical Chemistry B*, vol. 106, no. 29, pp. 7177–7185, 2002.

[185] J. Lee, T. Javed, T. Skeini, A. O. Govorov, G. W. Bryant, and N. A. Kotov, "Bioconjugated ag nanoparticles and cdte nanowires: Metamaterials with field-enhanced light absorption," *Angewandte Chemie-International Edition*, vol. 45, no. 29, pp. 4819–4823, 2006.

[186] Y. Wang, Z. Y. Tang, S. S. Tan, and N. A. Kotov, "Biological assembly of nanocircuit prototypes from protein-modified cdte nanowires," *Nano Letters*, vol. 5, no. 2, pp. 243–248, 2005.

[187] A. Gole and C. J. Murphy, "Polyelectrolyte-coated gold nanorods: Synthesis, characterization and immobilization," *Chemistry of Materials*, vol. 17, no. 6, pp. 1325–1330, 2005.

[188] A. O. Govorov, G. W. Bryant, W. Zhang, T. Skeini, J. Lee, N. A. Kotov, J. M. Slocik, and R. R. Naik, "Exciton-plasmon interaction and hybrid excitons in semiconductor-metal nanoparticle assemblies," *Nano Letters*, vol. 6, no. 5, pp. 984–994, 2006.

[189] J. Lee, J. Dulka, A. O. Govorov, and N. A. Kotov, "Bioconjugated cote and au nanoparticles for energy transport.," *Abstracts of Papers of the American Chemical Society*, vol. 228, pp. U897–U897, 2004.

[190] J. Lee, A. O. Govorov, and N. A. Kotov, "Bioconjugated superstructures of cdte nanowires and nanoparticles: Multistep cascade forster resonance energy transfer and energy channeling," *Nano Letters*, vol. 5, no. 10, pp. 2063–2069, 2005.

[191] J. Lee, A. O. Govorov, and N. A. Kotov, "Nanoparticle assemblies with molecular springs: A nanoscale thermometer," *Angewandte Chemie-International Edition*, vol. 44, no. 45, pp. 7439–7442, 2005.

[192] T. Toyama, K. Matsune, H. Oda, M. Ohta, and H. Okamoto, "X-ray diffraction study of cds/cdte heterostructure for thin-film solar cell: influence of cds grain size on subsequent growth of (111)-oriented cdte film," *Journal of Physics D-Applied Physics*, vol. 39, no. 8, pp. 1537–1542, 2006.

[193] J. Lee, P. Hernandez, J. Lee, A. O. Govorov, and N. A. Kotov, "Exciton-plasmon interactions inmolecular spring assemblies of nanowires and wavelength-based protein detection," *Nature Materials*, vol. 6, no. 4, pp. 291–295, 2007.

[194] M. H. Chowdhury, S. N. Malyn, K. Aslan, J. R. Lakowicz, and C. D. Geddes, "Multicolor directional surface plasmon-coupled chemiluminescence," *Journal of Physical Chemistry B*, vol. 110, no. 45, pp. 22644–22651, 2006.

[195] E. F. Schubert, A. M. Vredenberg, N. E. J. Hunt, Y. H. Wong, P. C. Becker, J. M. Poate, D. C. Jacobson, L. C. Feldman, and G. J. Zydzik, "Giant enhancement of luminescence intensity in er-doped si/sio2 resonant cavities," *Applied Physics Letters*, vol. 61, no. 12, pp. 1381–1383, 1992.

[196] V. E. Choong, Y. Park, N. Shivaparan, C. W. Tang, and Y. Gao, "Deposition-induced photoluminescence quenching of tris-(8-hydroxyquinoline) aluminum," *Applied Physics Letters*, vol. 71, no. 8, pp. 1005–1007, 1997.

[197] A. A. Mamedov, A. Belov, M. Giersig, N. N. Mamedova, and N. A. Kotov, "Nanorainbows: Graded semiconductor films from quantum dots," *Journal of the American Chemical Society*, vol. 123, no. 31, pp. 7738–7739, 2001.

[198] A. L. Rogach, D. S. Koktysh, M. Harrison, and N. A. Kotov, "Layer-by-layer assembled films of hgte nanocrystals with strong infrared emission," *Chemistry of Materials*, vol. 12, no. 6, pp. 1526–1528, 2000.

[199] A. O. Govorov, J. Lee, and N. A. Kotov, "Theory of plasmon-enhanced forster energy transfer in optically excited semiconductor and metal nanoparticles," *Physical Review B*, vol. 76, no. 12, p. 125308, 2007.

[200] B. N. J. Persson and N. D. Lang, "Electron-hole-pair quenching of excited-states near a metal," *Physical Review B*, vol. 26, no. 10, pp. 5409–5415, 1982.

[201] E. D. Palik, "Handbook of optical-constants," *Journal of the Optical Society of America a-Optics Image Science and Vision*, vol. 1, no. 12, pp. 1297–1297, 1984.

[202] B. M. I. van der Zande, G. J. M. Koper, and H. N. W. Lekkerkerker, "Alignment of rod-shaped gold particles by electric fields," *Journal of Physical Chemistry B*, vol. 103, no. 28, pp. 5754–5760, 1999.

[203] B. S. Shim and N. A. Kotov, "Single-walled carbon nanotube combing during layer-by-layer assembly: From random adsorption to aligned composites," *Langmuir*, vol. 21, no. 21, pp. 9381–9385, 2005.

[204] B. S. Shim, P. Podsiadlo, D. G. Lilly, A. Agarwal, J. Leet, Z. Tang, S. Ho, P. Ingle, D. Paterson, W. Lu, and N. A. Kotov, "Nanostructured thin films made by diewetting method of layer-by-layer assembly," *Nano Letters*, vol. 7, no. 11, pp. 3266–3273, 2007.

[205] G. T. Wei, Z. S. Yang, C. Y. Lee, H. Y. Yang, and C. R. C. Wang, "Aqueous-organic phase transfer of gold nanoparticles and gold nanorods using an ionic liquid," *Journal of the American Chemical Society*, vol. 126, no. 16, pp. 5036–5037, 2004.

[206] B. P. Khanal and E. R. Zubarev, "Rings of nanorods," *Angewandte Chemie-International Edition*, vol. 46, no. 13, pp. 2195–2198, 2007.

[207] J. Yang, J. C. Wu, Y. C. Wu, J. K. Wang, and C. C. Chen, "Organic solvent dependence of plasma resonance of gold nanorods: A simple relationship," *Chemical Physics Letters*, vol. 416, no. 4-6, pp. 215–219, 2005.

[208] S. K. Eah, H. M. Jaeger, N. F. Scherer, G. P. Wiederrecht, and X. M. Lin, "Plasmon scattering from a single gold nanoparticle collected through an optical fiber," *Applied Physics Letters*, vol. 86, no. 3, p. 031902, 2005.

[209] J. Perez-Juste, B. Rodriguez-Gonzalez, P. Mulvaney, and L. M. Liz-Marzan, "Optical control and patterning of gold-nanorod-poly(vinyl alcohol) nanocomposite films," *Advanced Functional Materials*, vol. 15, no. 7, pp. 1065–1071, 2005.

[210] Z. Kam, "Absorption and scattering of light by small particles - bohren,c, huffman,dr," *Nature*, vol. 306, no. 5943, pp. 625–625, 1983.

[211] P. B. Johnson and R. W. Christy, "Optical-constants of noble-metals," *Physical Review B*, vol. 6, no. 12, pp. 4370–4379, 1972.

[212] J. A. Stratton, I. Antennas, and P. Society., *Electromagnetic theory*. IEEE Press series on electromagnetic wave theory, Hoboken, New Jersey: John Wiley & Sons, Inc., 2007.

[213] S. B. Prusiner, "Prions," *Proceedings of the National Academy of Sciences of the United States of America*, vol. 95, no. 23, pp. 13363–13383, 1998.

[214] M. Cisse and L. Mucke, "Alzheimer's disease a prion protein connection," *Nature*, vol. 457, no. 7233, pp. 1090–1091, 2009.

[215] A. Taraboulos, K. Jendroska, D. Serban, S. L. Yang, S. J. Dearmond, and S. B. Prusiner, "Regional mapping of prion proteins in brain," *Proceedings of the National Academy of Sciences of the United States of America*, vol. 89, no. 16, pp. 7620–7624, 1992.

[216] C. Weissmann, "The state of the prion," *Nature Reviews Microbiology*, vol. 2, no. 11, pp. 861–871, 2004.

[217] J. Castilla, P. Saa, and C. Soto, "Detection of prions in blood," *Nature Medicine*, vol. 11, no. 9, pp. 982–985, 2005.

[218] P. Brown, L. Cervenakova, and H. Diringer, "Blood infectivity and the prospects for a diagnostic screening test in creutzfeldt-jakob disease," *Journal of Laboratory and Clinical Medicine*, vol. 137, no. 1, pp. 5–13, 2001.

[219] A. Aguzzi and M. Glatzel, "Prion infections, blood and transfusions," *Nature Clinical Practice Neurology*, vol. 2, no. 6, pp. 321–329, 2006.

[220] P. Brown, "Blood infectivity, processing and screening tests in transmissible spongiform encephalopathy," *Vox Sanguinis*, vol. 89, no. 2, pp. 63–70, 2005.

[221] P. Saa, J. Castilla, and C. Soto, "Presymptomatic detection of prions in blood," *Science*, vol. 313, no. 5783, pp. 92–94, 2006.

[222] G. P. Saborio, B. Permanne, and C. Soto, "Sensitive detection of pathological prion protein by cyclic amplification of protein misfolding," *Nature*, vol. 411, no. 6839, pp. 810–813, 2001.

[223] J. G. Safar, M. Scott, J. Monaghan, C. Deering, S. Didorenko, J. Vergara, H. Ball, G. Legname, E. Leclerc, L. Solforosi, H. Serban, D. Groth, D. R. Burton, S. B. Prusiner, and R. A. Williamson, "Measuring prions causing bovine spongiform encephalopathy or chronic wasting disease by immunoassays and transgenic mice," *Nature Biotechnology*, vol. 20, no. 11, pp. 1147–1150, 2002.

[224] R. A. Alvarez-Puebla and L. M. Liz-Marzan, "Sers-based diagnosis and biodetection," *Small*, vol. 6, no. 5, pp. 604–610, 2010.

[225] D. V. Talapin, J. S. Lee, M. V. Kovalenko, and E. V. Shevchenko, "Prospects of colloidal nanocrystals for electronic and optoelectronic applications," *Chemical Reviews*, vol. 110, no. 1, pp. 389–458, 2010.

[226] A. Gole and C. J. Murphy, "Seed-mediated synthesis of gold nanorods: Role of the size and nature of the seed," *Chemistry of Materials*, vol. 16, no. 19, pp. 3633–3640, 2004.

[227] J. Kneipp, X. T. Li, M. Sherwood, U. Panne, H. Kneipp, M. I. Stockman, and K. Kneipp, "Gold nanolenses generated by laser ablation-efficient enhancing structure for surface enhanced raman scattering analytics and sensing," *Analytical Chemistry*, vol. 80, no. 11, pp. 4247–4251, 2008.

[228] G. W. Bryant, F. J. G. De Abajo, and J. Aizpurua, "Mapping the plasmon resonances of metallic nanoantennas," *Nano Letters*, vol. 8, no. 2, pp. 631–636, 2008.

[229] M. I. Stockman and P. Hewageegana, "Nanolocalized nonlinear electron photoemission under coherent control," *Nano Letters*, vol. 5, no. 11, pp. 2325–2329, 2005.

[230] Y. R. Fang, H. Wei, F. Hao, P. Nordlander, and H. X. Xu, "Remote-excitation surface-enhanced raman scattering using propagating ag nanowire plasmons," *Nano Letters*, vol. 9, no. 5, pp. 2049–2053, 2009.

[231] Z. P. Li, F. Hao, Y. Z. Huang, Y. R. Fang, P. Nordlander, and H. X. Xu, "Directional light emission from propagating surface plasmons of silver nanowires," *Nano Letters*, vol. 9, no. 12, pp. 4383–4386, 2009.

[232] L. Rodriguez-Lorenzo, R. A. Alvarez-Puebla, I. Pastoriza-Santos, S. Mazzucco, O. Stephan, M. Kociak, L. M. Liz-Marzan, and F. J. G. de Abajo, "Zeptomol detection through controlled ultrasensitive surface-enhanced raman scattering," *Journal of the American Chemical Society*, vol. 131, no. 13, pp. 4616–4618, 2009.

[233] J. Aizpurua, G. W. Bryant, L. J. Richter, F. J. G. de Abajo, B. K. Kelley, and T. Mallouk, "Optical properties of coupled metallic nanorods for field-enhanced spectroscopy," *Physical Review B*, vol. 71, no. 23, p. 235420, 2005.

[234] A. R. Tao, D. P. Ceperley, P. Sinsermsuksakul, A. R. Neureuther, and P. D. Yang, "Self-organized silver nanoparticles for three-dimensional plasmonic crystals," *Nano Letters*, vol. 8, no. 11, pp. 4033–4038, 2008.

[235] X. H. Huang, S. Neretina, and M. A. El-Sayed, "Gold nanorods: From synthesis and properties to biological and biomedical applications," *Advanced Materials*, vol. 21, no. 48, pp. 4880–4910, 2009.

[236] G. Braun, I. Pavel, A. R. Morrill, D. S. Seferos, G. C. Bazan, N. O. Reich, and M. Moskovits, "Chemically patterned microspheres for controlled nanoparticle assembly in the construction of sers hot spots," *Journal of the American Chemical Society*, vol. 129, no. 25, pp. 7760–7761, 2007.

[237] X. D. Chen, S. Yeganeh, L. D. Qin, S. Z. Li, C. Xue, A. B. Braunschweig, G. C. Schatz, M. A. Ratner, and C. A. Mirkin, "Chemical fabrication of heterometallic nanogaps for molecular transport junctions," *Nano Letters*, vol. 9, no. 12, pp. 3974–3979, 2009.

[238] J. Jiang, K. Bosnick, M. Maillard, and L. Brus, "Single molecule raman spectroscopy at the junctions of large ag nanocrystals," *Journal of Physical Chemistry B*, vol. 107, no. 37, pp. 9964–9972, 2003.

[239] D. R. Brown, B. Schmidt, and H. A. Kretzschmar, "Role of microglia and host prion protein in neurotoxicity of a prion protein fragment," *Nature*, vol. 380, no. 6572, pp. 345–347, 1996.

[240] K. E. Shafer-Peltier, C. L. Haynes, M. R. Glucksberg, and R. P. Van Duyne, "Toward a glucose biosensor based on surface-enhanced raman scattering," *Journal of the American Chemical Society*, vol. 125, no. 2, pp. 588–593, 2003.

[241] S. Lehmann, "Metal ions and prion diseases," *Current Opinion in Chemical Biology*, vol. 6, no. 2, pp. 187–192, 2002.

[242] P. Podsiadlo, E. M. Arruda, E. Kheng, A. M. Waas, J. Lee, K. Critchley, M. Qin, E. Chuang, A. K. Kaushik, H. S. Kim, Y. Qi, S. T. Noh, and N. A. Kotov, "Lbl assembled laminates with hierarchical organization from nano- to microscale: High-toughness nanomaterials and deformation imaging," *Acs Nano*, vol. 3, no. 6, pp. 1564–1572, 2009.

[243] P. Podsiadlo, M. Qin, M. Cuddihy, J. Zhu, K. Critchley, E. Kheng, A. K. Kaushik, Y. Qi, H. S. Kim, S. T. Noh, E. M. Arruda, A. M. Waas, and N. A. Kotov, "Highly ductile multilayered films by layer-by-layer assembly of oppositely charged polyurethanes for biomedical applications," *Langmuir*, vol. 25, no. 24, pp. 14093–14099, 2009.

[244] C. L. Murphy and C. J. Orendorff, "Alignment of gold nanorods in polymer composites and on polymer surfaces," *Advanced Materials*, vol. 17, no. 18, pp. 2173–2177, 2005.

[245] Y. Shindo, K. Kani, J. Horinaka, R. Kuroda, and T. Harada, "The application of polarization modulation method to investigate the optical homogeneity of polymer films," *Journal of Plastic Film & Sheeting*, vol. 17, no. 2, pp. 164–183, 2001.

[246] Y. Shindo and M. Nishio, "The effect of linear anisotropies on the cd spectrum - is it true that the oriented polyvinyalcohol film has a magic chiral domain inducing optical-activity in achiral molecules," *Biopolymers*, vol. 30, no. 1-2, pp. 25–31, 1990.